



**Michigan  
Technological  
University**

Michigan Technological University  
**Digital Commons @ Michigan Tech**

---

Dissertations, Master's Theses and Master's Reports

---

2019

# **LITHIUM-ION BATTERY DEGRADATION EVALUATION THROUGH BAYESIAN NETWORK METHOD FOR RESIDENTIAL ENERGY STORAGE SYSTEMS**

Khalid Khan

*Michigan Technological University, [kkhan@mtu.edu](mailto:kkhan@mtu.edu)*

Copyright 2019 Khalid Khan

---

## **Recommended Citation**

Khan, Khalid, "LITHIUM-ION BATTERY DEGRADATION EVALUATION THROUGH BAYESIAN NETWORK METHOD FOR RESIDENTIAL ENERGY STORAGE SYSTEMS", Open Access Dissertation, Michigan Technological University, 2019.

<https://doi.org/10.37099/mtu.dc.etdr/935>

Follow this and additional works at: <https://digitalcommons.mtu.edu/etdr>



Part of the [Power and Energy Commons](#)

LITHIUM-ION BATTERY DEGRADATION EVALUATION THROUGH BAYESIAN  
NETWORK METHOD FOR RESIDENTIAL ENERGY STORAGE SYSTEMS

By

Khalid Khan

A DISSERTATION

Submitted in partial fulfillment of the requirements for the degree of

DOCTOR OF PHILOSOPHY

In Electrical Engineering

MICHIGAN TECHNOLOGICAL UNIVERSITY

2019

© 2019 Khalid Khan

This dissertation has been approved in partial fulfillment of the requirements for the Degree of DOCTOR OF PHILOSOPHY in Electrical Engineering.

Department of Electrical and Computer Engineering

Dissertation Co-Advisor: *Dr. Lucia Gauchia*

Dissertation Co-Advisor: *Dr. Chee-Wooi Ten*

Committee Member: *Dr. Michael C. Roggemann*

Committee Member: *Dr. Wayne W. Weaver*

Committee Member: *Dr. Laura E. Brown*

Department Chair: *Dr. Glen E. Archer*

# Table of Contents

List of figures.....	vi
List of tables.....	ix
Preface.....	x
Acknowledgments.....	xi
Abstract.....	xii
Outline.....	1
References.....	7
Analysis of Battery Degradation Models at Various Scales.....	8
1.1    Introduction .....	9
1.2    Material and Electrode Level Models .....	11
1.2.1        Pseudo-2D Models .....	14
1.2.2        Single Particle Models.....	18
1.2.3        Summarizing Degradation Models at Material & Electrode Level ....	20
1.3    Cell Level Models .....	22
1.3.1        Arrhenius Kinetic Based Models.....	25
1.3.2        Polynomial Based Models.....	29
1.3.3        Summarizing Degradation Models at Cell Level .....	32
1.4    Module and Pack Level Models.....	35
1.5    Probabilistic Degradation Models .....	40
1.6    Conclusion.....	41
References.....	43
Comparison of Li-ion Battery Equivalent Circuit Modeling Using Impedance Analyzer and Bayesian Networks.....	52
2.1    Introduction .....	53
2.2    Overview of Experimental Method.....	56
2.3    Testing Procedure.....	58
2.3.1        Capacity Test.....	58
2.3.2        Hybrid Pulse Power Characterization Test.....	61
2.3.3        Electrochemical Impedance Spectroscopy Test .....	63
2.4    Equivalent Circuit Modeling.....	68
2.4.1        Impedance Analyzer Fitting .....	71

2.4.2	Developing ECM with Bayesian Model.....	74
2.5	Impedance Analyzer vs. Bayesian Network Models.....	79
2.5.1	Estimation Accuracy .....	79
2.5.2	Estimation Error Analysis .....	82
2.5.3	Drive Cycle Validation.....	85
2.6	Conclusion.....	87
	References.....	89
Residential Battery Degradation in Smart Home Using Hierarchical Bayesian Network.....		92
3.1	Introduction .....	93
3.2	Smart Home Energy Management System .....	100
3.2.1	Load Models.....	101
3.2.1.1	Inflexible Loads.....	101
3.2.1.2	Uninterruptible Loads.....	102
3.2.1.3	Interruptible Loads .....	104
	3.2.1.3.1 Battery Energy Storage System Load .....	104
	3.2.1.3.2 Electric Vehicle Load .....	106
3.2.1.4	Thermostatically Controlled Loads .....	107
3.2.2	PV Generation Model.....	108
3.2.3	Problem Formulation.....	109
3.3	Hierarchical Bayesian Network for Battery Degradation Estimation .....	111
3.3.1	Network Development.....	112
3.3.2	Mathematical Expressions.....	115
3.3.3	Training and Evaluation of BN through Testing.....	119
3.4	Case Study: Evaluate Degradation of The Battery.....	121
3.4.1	Effect of Grid Services on Capacity Fade .....	121
3.4.2	Effect of EV Schedule on Capacity Fade .....	123
3.4.3	Impact of Weather and Location on Capacity Fade .....	125
3.5	Conclusion.....	128
	References.....	129
Low-cost Hardware-in-the-Loop Lithium-Ion Battery Degradation System for Residential Energy Storage.....		133
4.1	Introduction .....	134
4.2	Overview of the HIL Simulation.....	135
4.3	Residential Load Problem Formulation .....	136
4.4	Schematic and Operation of MINILAB HIL System.....	139
4.5	Initial Results & the Effectivity of MiniLab as HIL System .....	144

4.6 Conclusion.....	145
References.....	146
Conclusions.....	148
Contributions.....	151
Future Work.....	153
A Copyright Documentations .....	155

## List of figures

Figure 1. Graphical Outline. ....	4
Figure 1.1. The trend of the aging models' analyses in this chapter. ....	11
Figure 1.2. Li-ion cell schematic .....	12
Figure 1.3. Degradation factors in the negative and positive electrodes .....	14
Figure 1.4. The basic idea of material and electrode level degradation models.....	21
Figure 1.5. Degradation factors in the cell level models .....	24
Figure 1.6. The basic idea of cell level degradation models.....	33
Figure 2.1. The disassembled commercial Li-ion battery pack. ....	57
Figure 2.2. Time-domain test experimental setup. ....	59
Figure 2.3. Capacity test results.....	60
Figure 2.4. The HPPC test load profile and response voltage. ....	62
Figure 2.5. The HPPC test Ah response. ....	62
Figure 2.6. The ideal Nyquist plot for <i>LiCoO2</i> Li-ion battery.....	65
Figure 2.7. Time-domain test experimental setup. ....	66
Figure 2.8. The measured impedance by EIS test at 20°C.....	67
Figure 2.9. The measured impedance by EIS test at 0°C.....	67
Figure 2.10. The measured impedance by EIS test at -10°C. ....	67
Figure 2.11. Equivalent circuit components .....	69
Figure 2.12. Generated equivalent circuit models .....	70
Figure 2.13. Bayesian network for the ECM model .....	76
Figure 2.14. The Bayesian model outputs histogram for <i>R0</i> . ....	77
Figure 2.15. The Bayesian model output gamma PDF for <i>R0</i> at various SOCs. ....	77
Figure 2.16. The Bayesian model output normal PDF of parameters for <i>R0</i> . ....	78

Figure 2.17. Accuracy of various Impedance Analyzer model at 20°C and 80% SOC....	80
Figure 2.18. Accuracy of various Impedance Analyzer model at 20°C and 20% SOC....	80
Figure 2.19. Accuracy of various BN models at 20°C and 80% SOC.....	81
Figure 2.20. Accuracy of various BN models at 20°C and 20% SOC.....	81
Figure 2.21. The probability distribution of fitting error for real and imaginary parts of impedance in Impedance Analyzer models. ....	82
Figure 2.22. The probability distribution of estimation error for real and imaginary parts of impedance in BN models.....	83
Figure 2.23. The experimental load current and battery SOC%.....	85
Figure 2.24. The experimental validation of 8RC ECM developed with Impedance Analyzer fitting. ....	86
Figure 2.25. Accuracy of Impedance Analyzer models.....	87
Figure 2.26. Accuracy of BN models .....	87
Figure 3.1. Inflexible load profile [27]. ....	102
Figure 3.2. Hot water usage pattern in a residence [30]. ....	108
Figure 3.3. The utilized day ahead RT price profile. ....	110
Figure 3.4. Developed BN for estimating degradation for residential battery energy storage systems. ....	114
Figure 3.5. Training of modeled Bayesian Network.....	120
Figure 3.6. Testing of modeled Bayesian Network. ....	120
Figure 3.7. Effect of grid services on the capacity fade.....	122
Figure 3.8. An increase in PV power used to charge the battery.....	123
Figure 3.9. Effect of EV schedule on capacity fade. ....	124
Figure 3.10. Capacity fade increases with EV departure time and Ah. ....	124
Figure 3.11. Effect of the ambient temperature of various locations on the capacity fade. ....	125



Figure 3.12. Increase in the Ah throughput for higher ambient temperature. ....	126
Figure 3.13. Increase in contribution to capacity fade for increased solar irradiance. ...	127
Figure 3.14. Effect of capacity fade for increased solar irradiance .....	127
Figure 4.1. Overview of the HIL simulation.....	136
Figure 4.2. Single cell load profile while grid services are prohibited. ....	138
Figure 4.3. Single cell load profile while grid services are performed.....	138
Figure 4.4. Solar irradiance in both case scenarios.....	139
Figure 4.5. Schematic of MiniLab HIL simulation system. ....	140
Figure 4.6. MiniLab HIL simulation system. ....	142
Figure 4.7. Fish1 MiniLab HIL system. ....	142
Figure 4.8. MiniLab HIL simulation system. ....	143
Figure 4.9. Results of HIL while grid services are performed.....	144

## List of tables

Table 1.1. Summary of material and electrode level degradation models.....	22
Table 1.2. Summary of cell level degradation models.....	34
Table 1.3. Summary of cell level degradation models for calendar aging .....	35
Table 1.4. Summary of battery degradation models .....	43
Table 2.1. Battery pack and cell details .....	56
Table 2.2. The measured actual capacity of commercial Li-ion battery.....	60
Table 2.3. OCV-DOD data from HPPC test.....	63
Table 2.4. OCV-DOD-T function parameters .....	72
Table 2.5. ECM component function parameters .....	73
Table 2.6. BN 2RC and 3RC model Data at 20°C .....	78
Table 2.7. Rayleigh distribution parameters of impedance fitting and BN estimation.....	84
Table 3.1. List of nomenclatures.....	96
Table 3.2. NRMSDP Values from Training and Testing.....	121

## Preface

Chapters of this dissertation contain published material. The following list provides the published material presented in conferences and journal articles.

M. Jafari, K. Khan, L. Gauchia, “Deterministic models of Li-ion battery aging: It is a matter of scale,” *Journal of Energy Storage*, 2018.

W. Wang, P. Malysz, K. Khan, L. Gauchia and A. Emadi, "Modeling, parameterization, and benchmarking of a lithium-ion electric bicycle battery," in *2016 IEEE Energy Conversion Congress and Exposition (ECCE)*, 2016.

K. Khan, Z. Bin, and R. Amir, "Real-Time Application of Battery State of Charge and State of Health Estimation," SAE Technical Paper, in *WCX™ 17: SAE World Congress Experience*, 2017.

K. Khan, M. Jafari, L. Gauchia, “Comparison of Li-ion battery equivalent circuit modeling using impedance analyzer and Bayesian networks”, *IET Electrical Systems in Transportation*, 2018.

K. Khan, T. Hossen, A. Savaci, S. Paudyal, L. Gauchia, “Design of A Simplified Hierarchical Bayesian Network for Residential Energy Storage Degradation,” in *2019 IEEE Power & Energy Society General Meeting (PESGM)*, 2019.

K. Khan, L. E. Brown, S. Paudyal, L. Gauchia, “Evaluation of Residential Battery Energy Storage Degradation in Smart Home using Detailed Hierarchical Bayesian Network,” in review.

K. Khan, T. Hossen, L. Gauchia, “Low-cost Hardware-in-the-Loop Lithium-Ion Battery Degradation System for Residential Energy Storage,” in review.

Khalid Khan had the major or significant contribution in modeling simulation, conducting experiments, and writing the material for all of these publications.

## Acknowledgments

There are many people I would like to acknowledge for their relentless support throughout my time in graduate school. To be specific, this thesis would not be possible without the help from my advisor, thesis committee members, colleagues, funding authority, my friends, and lastly my family members.

I joined the graduate school as a Ph.D. student without a supervisor, funding, or any teaching assistantship. With my dedication, diligence and innate abilities as a researcher, I was able to convince Dr. Lucia Gauchia, my recently ex-advisor, to let me join her research group. Academically, Dr. Gauchia taught me the fundamentals, characteristics and associated experimental procedures for different energy storage systems. On a personal level, she taught me how to be a good, responsible human being above anything else. I'm grateful that I was able to learn from and work with Dr. Gauchia, who has enriched me as a person overall. On this note, I would like to express my gratitude to Dr. Chee-Wooi Ten for stepping in as my advisor to supervise over my thesis and defense.

Besides my advisor, I would also like to thank my thesis committee members (Dr. Roggemann, Dr. Weaver, and Dr. Brown). I've taken several courses under Dr. Weaver, which trained me to think critically and realize there may be more than one answer to an engineering problem. The bulk of the research is based on Bayesian Networks, it wouldn't have been possible without guidance from Dr. Brown.

I would like to mention about my colleagues, Dr. Mehdi Jafari, Tareq Hossen and Mark Sloat. Mehdi and I worked side by side, he was instrumental in helping me grasp the concepts of Bayesian Network. I could always rely on Mark for any technical help, without his guidance all my experimental work would be for naught.

I would like to acknowledge the Department of Electrical and Computer Engineering for supporting me with a teaching assistant position throughout graduate school. Moreover, I would express my gratitude to National Science Foundation for supporting our research with Award 1651256. Furthermore, my gratitude goes out to the graduate school for supporting me with finishing fellowship.

I want to thank my friends here at Michigan tech, especially the Bangladeshi community, they were like bright sunny days in frigid cold weather conditions of Houghton. My gratitude goes out to my family, especially my father Ehtesham Ul Haque Khan, the source of my inspiration for starting grad school, and one of the happiest people on the day of my defense.

Lastly, my wife Farhana Haque... without her support, none of this would be possible. Her encouragement during the toughest situations, her grasp on reality helping me make tough decisions, and her trust in my qualities to complete my Ph.D. have gotten me this far.

## Abstract

Batteries continue to infiltrate in innovative applications with the technological advancements led by Li-ion chemistry in the past decade. Residential energy storage is one such example, made possible by increasing efficiency and decreasing the cost of solar PV. Residential energy storage, charged by rooftop solar PV is tied to the grid, provides household loads. This multi-operation role has a significant effect on battery degradation. These contributing factors especially solar irradiation and weather conditions are highly variable and can only be explained with probabilistic analysis. However, the effect of such external factors on battery degradation is approached in recent literature with mostly deterministic and some limited stochastic processes. Thus, a probabilistic degradation analysis of Li-ion batteries in residential energy storage is required to evaluate aging and relate to the external causal factors. The literature review revealed modified Arrhenius degradation model for Li-ion battery cells. Though originating from an empirical deterministic method, the modified Arrhenius equation relates battery degradation with all the major properties, i.e. state of charge, C-rate, temperature, and total amp-hour throughput.

These battery properties are correlated with external factors while evaluation of capacity fade of residential Li-ion battery using a proposed detailed hierarchical Bayesian Network (BN), a hierarchical probabilistic framework suitable to analyze battery degradation stochastically. The BN is developed considering all the uncertainties of the process including, solar irradiance, grid services, weather conditions, and EV schedule. It also includes hidden intermediate variables such as battery power and power generated by

solar PV. Markov Chain Monte-Carlo analysis with Metropolis-Hastings algorithm is used to estimate capacity fade along with several other interesting posterior probability distributions from the BN. Various informative and promising results were obtained from multiple case scenarios that were developed to explore the effect of the aforementioned external factors on the battery. Furthermore, the methodologies involved to perform several characterizations and aging test that is essential to evaluate the estimation proposed by the hierarchical BN is explored. These experiments were conducted with conventional and low-cost hardware-in-the-loop systems that were developed and utilized to quantify the quality of estimation of degradation.

## Outline

Batteries, much like their users, operate by deriving energy from internal chemical reactions. Over the years, with multiple iterations of different tasks, the batteries' performance degrades, just like human beings. The degradation of batteries occurs internally with the deterioration of the involved chemical processes. These degradations culminate as either loss of capacity or loss of power. The loss of capacity limits the total energy that the battery can hold with a single charging procedure whereas, loss of power limits the current that the battery can provide at a certain instance. Thus, it is of paramount importance to determine the degradation of any battery to ensure continued performance and modification of usage pattern to elongate lifespan. These degradation phenomena can not be determined through measurements. Hence, these behaviors need to be estimated.

There are several approaches to define the degradation of the battery. In most cases, these can be categorized into two major groups, off-line laboratory experiment, simulation based and on-line application specific approach. The first group focuses on lab based experiments and develops models to represent battery degradation. This approach, though highly accurate, is limited to the specific chemistry of the battery and a particular application. The other approach is geared towards the particular application where the aging is determined from solely available measurements while the battery is operating. This method is more suitable to define batteries' health to a battery management system (BMS). This dissertation focuses on the first approach while attempting to relate to specific applications through probabilistic methods. The battery degradation is based on the lab

based off-line experiments and simulations whereas, probabilistic methods are utilized to incorporate, and relate the external factors to the degradation characteristics.

A recent survey from the National Renewable Energy Laboratory (NREL) shows that renewable energy resources are significantly less expensive than 10 years ago [1]. These renewable energy resources can reduce the cost of expansion while improving efficiency to meet the higher demand of the population. The research from NREL supports this trend of reducing the cost of solar panels and wind turbines. One issue with such renewable energy sources is storage. The production of renewable energy sources does not coincide with the electrical energy demand of the population. For example, with solar panels, the sun sets just as electricity demand increases with people coming home from work. Better energy storage, i.e. batteries will allow the electricity to be available to match the demand, even if the renewable source is not live. Lithium-ion is the most successful battery being used with renewable energy sources.

With the advancement of renewable energy systems and desire for demand side management, energy storage at residence is becoming an inevitability. Due to li-ions high energy density, longer service life, lower maintenance, it has become the leading technology in residential energy storage systems. The literature review on the degradation of residential energy storage revealed some shortcomings. There are several research groups working toward determining li-ion capacity degradation. These researchers use either stochastic, equivalent circuits, performance-based, electrochemical or empirical models of battery to solve this problem. These methods are based on modeling the battery degradation with data available from the prior lab-based tests. These methods produce a



deterministic result for degradation. Also, the lab experiments providing the degradation data are carried in a controlled environment. However, neither the process of degradation is deterministic, nor the factors affecting degradation remain constant over the lifetime of the battery. This non-deterministic nature of degradation arises from the fact that batteries operate with multiple applications. Most of these applications have stochastic nature, i.e. solar irradiation and weather patterns. It is not possible to define degradation for numerous scenarios generated by such stochastically operating causal factors. Thus, a data-driven method such as Bayesian Network is required to incorporate uncertainty in the measurement of data and process, provide probability distribution instead of deterministic value, and show the causal relationship between degradation to the factors that affect the deterioration process. Therefore, Bayesian models can provide a more insightful and accurate evaluation of li-ion capacity degradation.

My research attempts to establish a probabilistic battery degradation method. The purpose is to develop a methodology that can be utilized by the manufacturers and users alike to ascertain the remaining life of the battery in terms of capacity fade. Thus, it solves the shortcomings of contemporary techniques to determine battery degradation. This research generates a causal relationship between physical degradation of the battery capacity and their effects on the factors affecting the deterioration process leading towards performance deterioration of the entire system surrounding the li-ion battery. Though the research focuses on li-ion battery and limits itself on a residential application, the property of the Bayesian Network itself allows to branch out towards other future technologies and

applications with minor variations. This research was carried out through multiple stages as shown by the graphical outlined in Figure. 1.

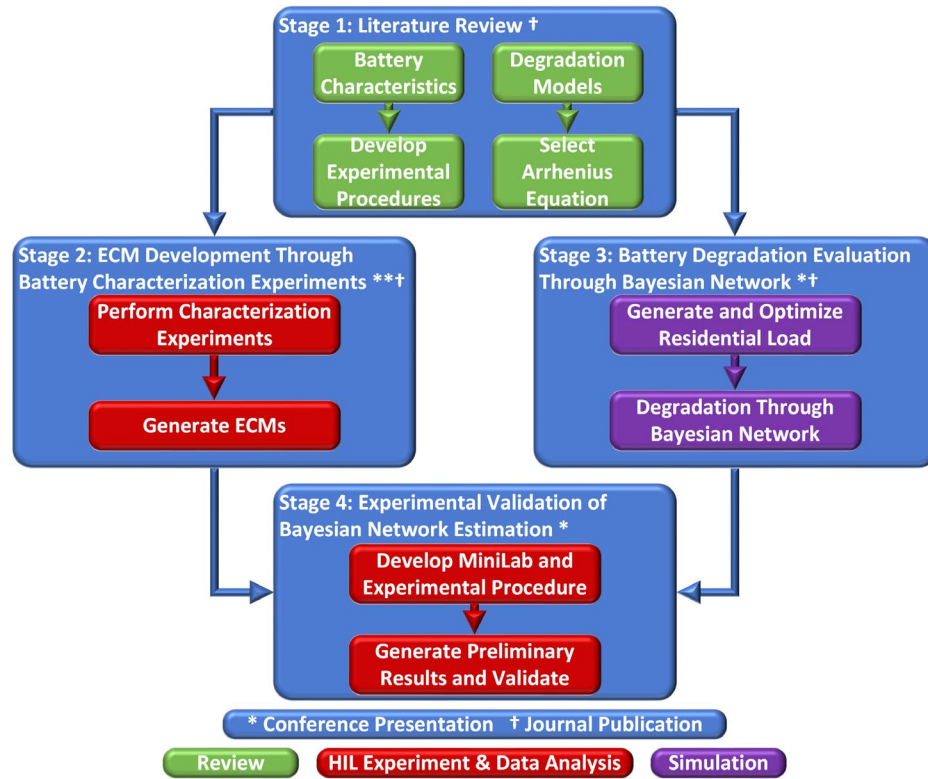


Figure 1. Graphical Outline.

The literature review stage was a two-part process, the study of battery performance and degradation characteristics, with associated experimental procedures involved. The study about battery performance, modeling, associated time-domain, and frequency-domain testing resulted in the foundation of the Energy Storage System and Sustainability (E3S) lab. Starting off E3S consisted of battery tester, thermal chamber, data acquisition system, impedance analyzer. The experimental procedures and equipment were utilized in stage two. Exploration of degradation methods supported the selection of the most appropriate method of defining capacity fade of li-ion batteries, modified Arrhenius

equation. The modified Arrhenius equation serves as the foundation of the mathematical model of capacity fade and utilized throughout stage three extensively.

In stage two, extensive experimental procedure, both time and frequency-domain were performed in order to develop multiple equivalent circuit model (ECM) of the Li-ion battery. Two systematic approaches were followed to develop the ECMs. First, the ECM is developed through fitting the time-domain and frequency-domain test results carried out on a 50V commercial Li-ion battery composed of Samsung ICR18650-22P cells. Later Bayesian Network method was applied to estimate the ECM circuit elements. In both cases, multiple circuit topologies were used to compare the accuracy of the model. The models were developed in MATLAB/Simulink environment. A highly dynamic drive cycle was utilized to validate the ECMs through hardware-in-loop testing. It was observed that the appropriate ECM topology used for the linear least square regression fitting generated an average error of 3.3% whereas for BN estimation it was 3.5%. The purpose of the experimental part in this stage was to obtain the necessary skills required for battery degradation testing. Hardware-in-loop testing is instrumental in order to perform any battery degradation testing. Furthermore, impedance analyzer testing and following data analysis to develop ECM provided the expertise to define battery aging in terms of battery internal impedance or loss of power. These acquired skills were applied in stage four to validate the results of aging obtained from stage three. Finally, Bayesian Network based regression to develop the ECM granted the knowledge to generate the Hierarchical Bayesian Network that was used in stage three. The ECMs produced through this stage is one of the most accurate ECMs available within the considered boundary conditions.

In stage three, the effect of various residential load on the battery was required to estimate the degradation for a household application. A residence equipped with an energy storage system, renewable source, smart home energy management system (SHEMS), and common household loads was simulated as a mixed-integer linear programming problem. This simulation provided the profiles of various loads while optimizing to reduce electricity bill. These load profiles were used to generate a detailed hierarchical BN to probabilistically estimate the capacity fade degradation of a residential battery energy storage in a smart home environment. The BN utilizes a stochastic method to relate the causal factors of residential battery degradation. Experimental results of lithium iron phosphate batteries were used to train the BN. The capacity fade was evaluated for several cases, originated from SHEMS. Since the BN can estimate the hidden variables in battery capacity fade, it is a very strong tool with high accuracy and reliable results. The cases show that the capacity fade of the residential battery system relies heavily on SHEMS architecture, load characteristics, user preferences, and geographical location. The case studies revealed that performing grid services reduces the capacity fade by 3% more. Furthermore, geographical location with higher temperature and solar irradiance can have up to 5% more capacity fade with similar load patterns while reducing electricity consumption by 40%. The BN also provided information on the contribution of individual load on battery degradation. The overall result showed that a probabilistic analysis provides a more holistic picture of the battery health condition. The results of the estimation in this section, albeit supported by a trained BN with experimental results, is further verified in stage four. The battery load profile obtained through this probabilistic method for various scenarios was used in stage four to validate the estimations.

To validate the results, obtained from various scenarios in stage three, an experimental setup that could test multiple cells simultaneously was required. This system would reduce the time required for testing significantly as multiple cases could be tested concurrently. Previously, the battery tester used in stage 2, though highly accurate, could only test one cell at a time. Thus, a Raspberry Pi based “MiniLab” was developed to allow the testing of multiple cells. The Raspberry Pi acts as the processing unit, communicating with the DC/DC converter, electronic load, and battery through ADC and digital potentiometer. The control algorithm developed in Python consists of multiple PI controllers. These PI controllers ensure the battery was charging and discharging according to the load profile obtained from stage three. The preliminary testing of the MiniLab hardware shows promising results as the experimental results are in accordance with the result of the SHEMS optimized battery load profiles. The experimental procedure to degrade the battery in accordance with the load profiles is currently underway. Once the battery is depleted to a certain degree the results can be compared with estimations obtained from stage three.

Therefore, this dissertation addressed battery aging challenges from a probabilistic perspective, combining both simulation and experimental work to better understand the cause of battery degradation in a residential application.

## References

- [1] R. Fu, D. J. Feldman, and R. M. Margolis, “U.S. Solar Photovoltaic System Cost Benchmark: Q1 2018,” Golden, CO (United States), Nov. 2018.

# Chapter 1

## Analysis of Battery Degradation Models at Various Scales

### **Abstract**

Due to the increasing interest in the Li-ion battery aging studies among researchers, there are numerous battery degradation models presented in the literature. However, they are either focused on a single technology, form factor or scale. This can be challenging for researchers that typically have to bridge multiple technologies and are interested in crossing multiple scales, from material-level to cell, module, and pack level. Moreover, most of the research is concentrated on a deterministic analysis of battery degradation in all the form factors. Though, recent investigations have found that modeling probabilistically produces improved degradation estimations. This chapter explores both deterministic and probabilistic models presented for Li-ion battery degradation in different scales from the material level to the application level. In each scale, the main aging variables are summarized, the mathematical presentation of models are analyzed, and the merits and disadvantages of each scale are discussed. This review aims at bringing together methods and results for multiple technologies, form factors for the most common Li-ion

battery technologies. This review leads to the selection of the most appropriate Li-ion battery degradation model to be used in this dissertation.

## **1.1 Introduction**

As batteries are integrated into more applications than ever before, from portable to transportation, residential, and grid; defining battery degradation remains a challenging factor for manufacturers and users. The battery of choice of this growing industry is Li-ion due to available high energy density, but limited lifetime [1]. Up until recently, batteries were focused on performing single tasks. However, the trend is changing as batteries are being designed to perform multiple operations [2]–[4]. An example is residential energy storage systems, capable of participating in the ancillary services for the grid, besides providing backup for the residence. As each task has a different priority, degradation cost and economical cost or benefit, all these factors need to be considered when scheduling the tasks during the life of the battery.

It can become even more relevant when batteries are repurposed for second life in residential applications. For example, in transportation, due to the high power and energy demands, the battery end of life is reached when the capacity degrades to 80% of the original capacity. Therefore, there is still available capacity that can be repurposed as a second life in less demanding applications such as residential energy storage [5]. In this second life, the battery starts from a degraded point due to its first life and will degrade even faster. Therefore, modeling and identifying the causes of degradation is highly relevant. However, approaches are spread out at different scales due to the dichotomy of

aging taking place at the material level, but decision making and control taking place at the system level [6].

Other challenges add to this scenario, namely considering different Li-based technologies, form factors and cycling characteristics that affect the degradation observed. Other available review papers [7]–[9] focus either on a single application, single technology, a single scale while considering a deterministic approach. However, most researchers must bridge scales, technologies and consider a probabilistic approach to address multiple degradation phenomena. The objective of this chapter is to analyze the current approaches to battery degradation or aging modeling in each scale and its application across Li-ion technologies. This review will help the researchers to identify the main degradation factors and variables in each scale. This will also cover mathematical aging models, their strengths and weaknesses to be able to simulate the models for their own purpose. Figure 1.1 provides the graphical illustration of this chapter’s perspective, which starts the discussion at the material level and gradually moves upwards towards the application level. The rest of the chapter is organized as follows. Section 1.2 explains the aging in the material and electrode level and presents the related models in this scale. Afterward, section 1.3 scales up the aging models to the cell level. Section 1.4 explores how to use the aging models in the module, pack, and application level. Finally, section 1.5 discusses the probabilistic approach to model battery degradation modeling followed by the conclusion.



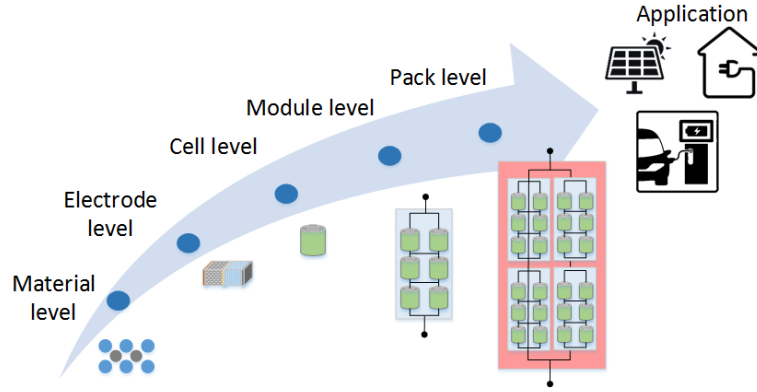


Figure 1.1. The trend of the aging models' analyses in this chapter.

## 1.2 Material and Electrode Level Models

Before discussing the degradation phenomenon inside the battery cell, a brief overview of the Li-ion battery cell's performance will be helpful. A Li-ion battery cell is composed of a negative electrode, positive electrode, separator in between electrodes, and electrolyte permeating throughout the battery as shown in Figure 1.2. During discharge, Li ions de-intercalate from the negative electrode, passing through the electrolyte, and intercalate in the positive electrode. At the same time, electrons travel in the same direction through the external circuit. The opposite reactions take place during the charging process.

Material scale models are based on the phenomenological approach developed by Doyle [10] to mathematically describe the movement of ions in the battery. This model was based on Newman's porous electrode theory [11]. However, it did not include a thermal model, which was added to the porous electrode model [12].

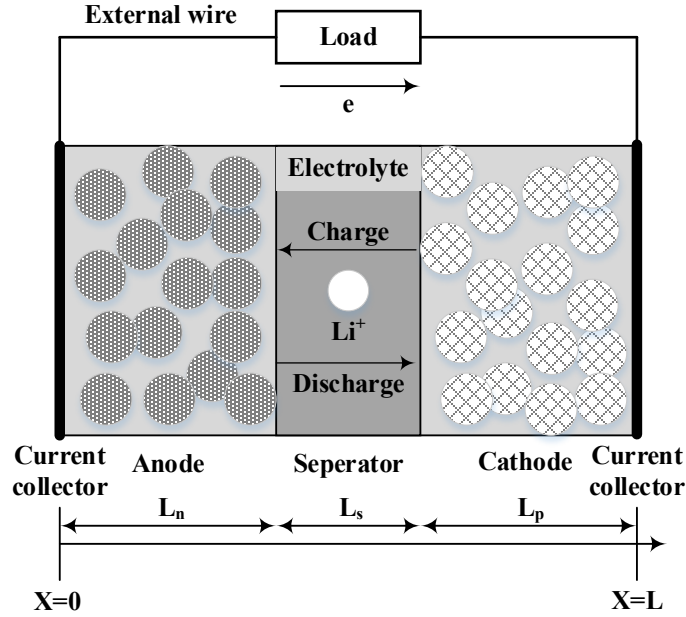


Figure 1.2. Li-ion cell schematic

Inside a Li-ion battery cell, aging starts in the electrodes/ electrolyte interface. The degradation in the positive and negative electrodes follows different mechanisms [13]. The negative electrode is commonly carbon-based and is made of graphite, titanate or silicon [14]. The major source of aging in the negative electrode is the formation of a resistive layer between the electrode and electrolyte surface due to the side reactions named solid electrolyte interface (SEI) [15]. The SEI is normally formed during the initial battery cycling and protects the electrode from corrosion and the electrolyte from reduction [16], [17]. However, in the long term, SEI's thickness and shape continue to grow and penetrate the porous structure of the negative electrode. It leads to (i) loss of the effective surface of the electrode (ii) increased resistance against Li-ions penetration and (iii) loss of cyclable lithium [18]–[20]. Note that the electrolyte materials define the SEI shape and properties [21]. Studies show that the high temperatures enhance the aging associated with SEI formation [22]–[24], and low temperatures lead to Li plating due to the lower rate of lithium

diffusion which reduces the cyclable lithium [25]. Another aging factor in the negative electrode can be the mechanical or electrical contact loss between the anode active materials and connecting parts due to the cycling [26]. Most of the aging models in the material and electrode level focus on the aging in the negative electrode/electrolyte interface as they believe that side reactions, and as a result of SEI formation, are more likely in the negative electrode due to its potential [27], [28].

Aging in the positive electrode happens slightly differently than in the negative electrode. The SEI formation in the positive electrode is dependent on the material used in the electrode but it cannot be detected easily [29]. Experiments show that the rise of impedance in the negative electrode due to cycling is higher than the positive electrode [30]. This indicates that the main SEI formation takes place on the negative electrode surface. Although the first stage of aging in the Li-ion cell is the SEI formation and cyclable Li loss in the negative electrode, the second stage in the battery cell aging is the loss of active materials in the positive electrode. This causes the cathode to be more intercalated at the end of each discharge [24]. The cathode active material loss can be the result of structural disordering, phase transitions and metal dissolution [31]. The positive electrode aging is not limited to the active materials loss; it also can be caused by the inactive components' degradation as binder decomposition, corrosion of the current collector and oxidation of the conductive agents [32]. Literature in the positive electrode aging mainly focuses on the experimentally oriented studies and does not present mathematical modeling of the aging in the cathode. Figure 1.3 summarizes the aging causes in the positive and negative electrodes.

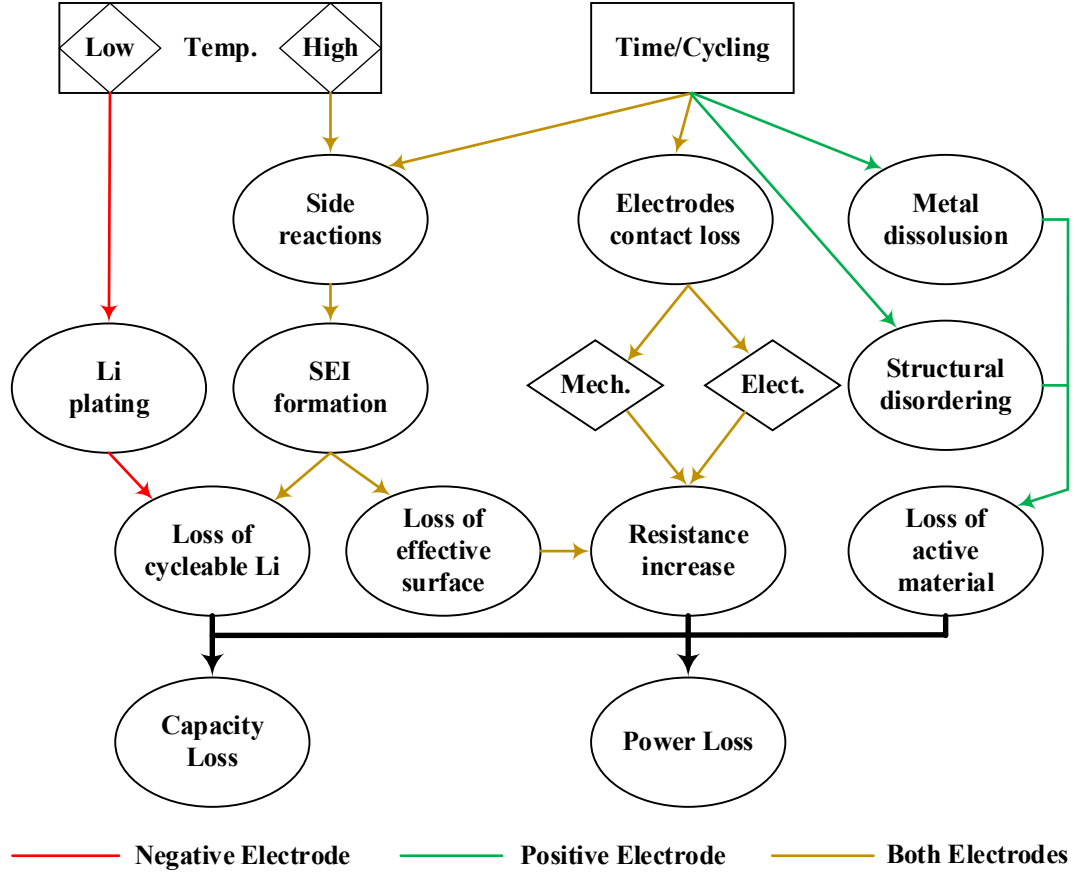


Figure 1.3. Degradation factors in the negative and positive electrodes

There are two popular methods to model electrode level battery degradation, Pseudo-2D Models (P2D), and Single Particle Model (SPM). The P2D is a physics-based electrode level model based on the conservation of species in electrode and electrolyte. Whereas, the SPM is another simplified form of P2D which excludes conservation of species in the electrolyte. These are discussed in detail in the following parts.

### 1.2.1 Pseudo-2D Models

These models are based on the porous electrode models by Doyle and expand them by including diffusion in the electrolytes and electrode as well as Butler-Volmer kinetics. These non-linear set of partial differential equations are one of the most used physics-based

models. Conservation of charge in the electrode or solid phase is given in (1-1) with the boundary conditions in (1-2). Similarly, the conservation of charge in the electrolyte is given by (1-3) with boundary conditions of (1-4) and (1-5). To complete the system, the conservation of lithium species in the electrode is represented by (1-6) along with boundary conditions in (1-7) and (1-8). Conservation of lithium species in the electrolyte is given by (1-9) with boundary condition (1-10). Finally, the dynamic performance is characterized by the Butler-Volmer kinetics (1-11) and surface potential by (1-12).

$$\frac{\partial}{\partial x} \left( \sigma^{eff} \frac{\partial}{\partial x} \phi_s \right) = j^{Li} \quad (1-1)$$

$$-\sigma_-^{eff} \frac{\partial}{\partial x} \phi_s|_{x=0} = \sigma_+^{eff} \frac{\partial}{\partial x} \phi_s|_{x=L} = \frac{I}{A} \quad (1-2)$$

$$\frac{\partial}{\partial x} \left( \kappa^{eff} \frac{\partial}{\partial x} \phi_e \right) + \frac{\partial}{\partial x} \left( \kappa_D^{eff} \frac{\partial}{\partial x} \ln c_e \right) = -j^{Li} \quad (1-3)$$

$$\frac{\partial}{\partial x} \phi_s|_{x=L_-} = \frac{\partial}{\partial x} \phi_s|_{x=L_+ + L_{sep}} = 0 \quad (1-4)$$

$$\frac{\partial}{\partial x} \phi_e|_{x=0} = \frac{\partial}{\partial x} \phi_e|_{x=L} = 0 \quad (1-5)$$

$$\frac{\partial c_s}{\partial t} = \frac{D_s}{r^2} \frac{\partial}{\partial r} \left( r^2 \frac{\partial c_s}{\partial r} \right) \quad (1-6)$$

$$\frac{\partial}{\partial r} c_s|_{r=0} = 0 \quad (1-7)$$

$$D_s \frac{\partial}{\partial r} c_s|_{r=R_s} = \frac{j^{Li}}{a_s F} \quad (1-8)$$

$$\frac{\partial(\varepsilon_e c_e)}{\partial t} = \frac{\partial}{\partial x} \left( D_e^{eff} \frac{\partial}{\partial x} c_e \right) + \frac{1 - t_+^0}{F} j^{Li} \quad (1-9)$$

$$\frac{\partial}{\partial x} c_e|_{x=0} = \frac{\partial}{\partial x} c_e|_{x=L} = 0 \quad (1-10)$$

$$j^{Li} = a_s i_0 \left[ \exp\left(\frac{\alpha_s F}{RT} \eta\right) - \exp\left(\frac{\alpha_c F}{RT} \eta\right) \right] \quad (1-11)$$

$$\eta = \phi_s - \phi_e - U \quad (1-12)$$

Here the solid and electrolyte potentials are  $\phi_s$  and  $\phi_e$ , respectively. The lithium concentrations in the solid and electrolyte phases are represented with  $c_s$  and  $c_e$ , correspondingly. The electronic conductivity  $\sigma^{eff}$ , ionic conductivity  $\kappa^{eff}$ , and the electrolyte diffusion coefficient  $D_e^{eff}$  are corrected by the Bruggeman factor [33]. The solid and electrolyte phase volume fractions are defined by  $\varepsilon_s$  and  $\varepsilon_e$ , respectively. Here,  $j^{Li}$  represents the Li-ion current density,  $i_0$  is the exchange current density. Also,  $F$ ,  $R$  and  $T$  are the Faraday's constant, the universal gas constant, and the temperature, respectively. The negative and positive electrodes transfer coefficients are  $\alpha_s$  and  $\alpha_c$ , respectively.

However, these equations do not capture the degradation phenomena completely as presented in Figure 1.3. As discussed, SEI formation and lithium plating are two dominant aging causes. They both modify the electrode film resistance, increasing it as the layers grow. This layer formation will affect the Butler-Volmer kinetics equation that represents

the rate of Li-ion intercalation in the electrode (1-13). The exponential terms are modified with  $R_{film}$  to characterize SEI formation and lithium plating. The included  $R_{film}$  is composed of both SEI and lithium plating as shown in (1-14).

$$j^{Li} = a_s i_0 \left[ \exp \left( \frac{\alpha_s F}{RT} \eta - \frac{R_{film}}{a_s} j^{Li} \right) - \exp \left( \frac{\alpha_c F}{RT} \eta - \frac{R_{film}}{a_s} j^{Li} \right) \right] \quad (1-13)$$

$$R_{film} = R_{SEI} + R_{Li} \quad (1-14)$$

The loss of active surface due to fracture increases the overall active area whilst the isolation of particles decreases the area. These changes will affect the differential equations representing phenomena in the solid, which are the conservation of charge in the solid (1-1) and the conservation of species in the solid (1-6). Modifications to these equations are linked to changes in the area  $A$  and  $a_s$  is given in (1-15), that will be affected by the number of cycles  $N$ . Material parameter  $k$  [34] dependent on particle size, state-of-charge, and its variations are obtained empirically for both fracture and isolation as given by (1-16) and (1-17), respectively.

$$a_s = a_{initial} + a_{fracture} - a_{isolation} \quad (1-15)$$

$$k_{fracture} = \frac{d \left( \frac{a_{fracture}}{a_{initial}} \right)}{dN} \quad (1-16)$$

$$k_{isolation} = \frac{d \left( \frac{a_{isolation}}{a_{initial}} \right)}{dN} \quad (1-17)$$

Mechanical stress that affects the electrode volume [35] can be considered through the modification of the Butler-Volmer kinetics equation through the inclusion of the mean stress  $\sigma_{mean}$  and the partial molar volume of lithium in the electrode  $\Omega$  as shown in (1-18).

$$j^{Li} = a_s i_0 \left[ \exp \left( \frac{\alpha_s F}{RT} \eta - \frac{\Omega \sigma_{mean}}{RT} \right) - \exp \left( \frac{\alpha_c F}{RT} \eta - \frac{\Omega \sigma_{mean}}{RT} \right) \right] \quad (1-18)$$

Randall et al. [36] suggest that computationally-heavy models such as P2D represent a burden for the battery management systems (BMS) capabilities. Therefore, they have presented an incremental model for SEI resistance and capacity fade calculations with simplifying assumptions as quasi-equilibrium state for cell and neglecting local electrolyte and electrode surface concentration variations, uniform intercalation and side reactions current density in anode surface and equal anode and cathode charge transfer coefficients. These simplifications account for less than 1% error, based on the results.

### 1.2.2 Single Particle Models

The Single Particle Models (SPM) presented in [10], [33], [37], [38] characterizes each electrode as a single particle. It represents a simplification of the P2D model by including the conservation of species in the electrode, but not in the electrolyte. By disregarding the lithium concentration distribution and the potential distribution in the electrolyte, the SPM can be prone to error at high currents [39]. The governing equations include the diffusion of lithium in the electrodes as (1-19) with boundary conditions (1-20) and (1-21), along with the modified Butler-Volmer equation (1-22). The latter can describe SEI growth by including the increased resistance. An increased resistance component is included to account for SEI growth to modify the Butler-Volmer equation.



$$\frac{\partial c_s}{\partial t} = \frac{D_s}{r^2} \frac{\partial}{\partial r} \left( r^2 \frac{\partial c_s}{\partial r} \right) \quad (1-19)$$

$$\frac{\partial}{\partial r} c_s|_{r=0} = 0 \quad (1-20)$$

$$D_s \frac{\partial}{\partial r} c_s|_{r=R_s} = \frac{j^{Li}}{a_s F} \quad (1-21)$$

$$j^{Li} = a_s i_0 \left[ \exp \left( \frac{\alpha_s F}{RT} \eta - \frac{R_{SEI}}{a_s} j^{Li} \right) - \exp \left( \frac{\alpha_c F}{RT} \eta - \frac{R_{SEI}}{a_s} j^{Li} \right) \right] \quad (1-22)$$

Safari et al. [40] have considered the side reactions kinetic equation as the index for SEI formation rate as shown in (1-23).

$$i_s = -F k_{f,s} c_{EC} \exp \left( -\frac{\beta_s F}{RT} (\Phi_1 - R_{SEI} I) \right) \quad (1-23)$$

Where,  $k_{f,s}$  and  $c_{EC}$  refer to rate constant of side reactions and solvent concentration in the SEI film, respectively. Also,  $\beta_s$  is the charge transfer coefficient for the side reactions and  $I$  is electrode total current. It is possible to calculate the side reactions current density by its dependency to total applied current, temperature, and the SEI layer thickness  $\delta$ , through the Arrhenius equation as shown in (1-24) [41].

$$i_s = \beta_0 e^{-\lambda \delta} \exp(-E_a/RT) I \quad (1-24)$$

Here,  $\beta_0$  is temperature independent pre-factor and  $\lambda$  is the limiting coefficient. Due to the weak relationship of  $e^{-\lambda \delta}$  to the temperature,  $\lambda$  can be defined by the inverse

Arrhenius equation as given by (1-25). Also,  $\lambda_0$  is constant. The growth rate of the SEI in (1-24) can be calculated with (1-26) [42]. Where,  $M_{SEI}$  stands for the SEI molecular weight and  $\rho_{SEI}$  is its density.

$$\lambda = \lambda_0 \exp(E_a/RT) \quad (1-25)$$

$$\frac{\partial \delta}{\partial t} = -\frac{i_s}{2F} \frac{M_{SEI}}{\rho_{SEI}} \quad (1-26)$$

Tanim et al. [43] have developed another reduced-order non-linear physic-based SPM and combined it with the degradation calculations as given by (1-27) and (1-28), which simplifies and reduces the model computations. The capacity fade is quantified by the percentage loss of the lithium  $c_s$  in the negative electrode. Here,  $S_n$  is the negative electrode' active surface. To find the power fade, the rate of rise of the SEI resistance is calculated by (1-28).

$$\frac{dc_s}{dt} = S_n i_s \quad (1-27)$$

$$\frac{dR_{SEI}}{dt} = -\frac{1}{\kappa_{SEI} S_n} \frac{i_s M_{SEI}}{2F \rho_{SEI}} \quad (1-28)$$

### 1.2.3 Summarizing Degradation Models at Material & Electrode Level

Graphical illustration of the discussed battery performance and degradation models in this scale is presented in Figure 1.4. The current and temperature are the input variables for the models. Open circuit voltage (OCV) as a function of SOC is obtained from the experiments and the electrochemical properties, that are defined for each battery chemistry

and materials. The outputs of these models are battery voltage, capacity, and power losses. In each iteration of the simulation, lithium current density is used to calculate the side reactions current and as a result the aging variables. Afterward, the SEI resistance and lithium concentration in the negative electrode are updated for the next simulation step.

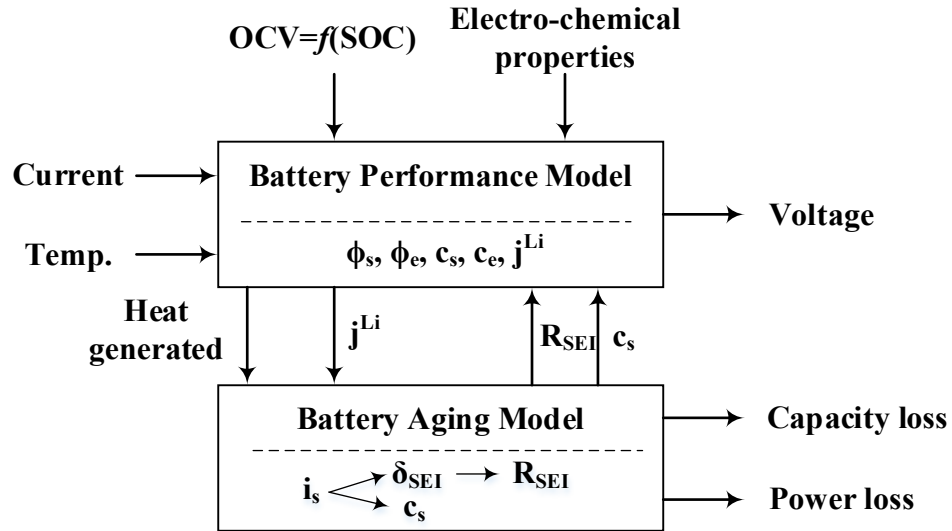


Figure 1.4. The basic idea of material and electrode level degradation models.

In summary, the material and electrode level capacity and power fade models are simulated by first, calculating the side reactions current. Afterward, obtaining the SEI film thickness followed by SEI resistance growth for power fade analysis. Finally, calculating the cyclable lithium loss for the capacity fade analysis. These models have high accuracy due to their detailed inside-the-cell dynamic equations without requiring bulk experimental measurements. However, there are complicated differential equations to be solved in each iteration and therefore, high computational load is involved. Fan [44] quantified the RMS error during model order reduction and observed nearly error increasing 35 times as the model is reduced from a 5th order to a 1st order model. Table 1.1 presents a summary of both P2D and SPM models.

Table 1.1. Summary of material and electrode level degradation models

Type	Major Mathematical Expressions Involved	Variables	Meas.	Ref.	Calculation Process	Pros and Cons
P2D	$\frac{\partial}{\partial x} \left( \sigma^{eff} \frac{\partial}{\partial x} \phi_s \right) = j^{Li}$ $\frac{\partial}{\partial x} \left( \kappa^{eff} \frac{\partial}{\partial x} \phi_e \right) + \frac{\partial}{\partial x} \left( \kappa_D^{eff} \frac{\partial}{\partial x} \ln c_e \right) = -j^{Li}$ $\frac{\partial c_s}{\partial t} = \frac{D_s}{r^2} \frac{\partial}{\partial r} \left( r^2 \frac{\partial c_s}{\partial r} \right)$ $j^{Li} = a_s i_0 \left[ \exp \left( \frac{\alpha_s F}{RT} \eta \right) - \exp \left( \frac{\alpha_c F}{RT} \eta \right) \right]$ <p>Modifications to the exponential term:</p> <ul style="list-style-type: none"> <li>SEI formation and Li plating  <math display="block">- \frac{R_{film}}{a_s} j^{Li}</math> </li> <li>Mechanical stress  <math display="block">- \frac{\Omega \sigma_{mean}}{RT}</math> </li> </ul>	$c_e$ $c_s$ $i_s$	$I$ $T$	[45] [11] [32]	<ul style="list-style-type: none"> <li>Calculate solid and electrolyte potentials</li> <li>Calculate solid and electrolyte species concentration</li> <li>Calculate current with modification of Butler-Volmer equation</li> <li>Update electrode total current</li> </ul>	<ul style="list-style-type: none"> <li>✓ Model results are valid over a large range of operation</li> <li>✓ Model is widely accepted</li> <li>– The intense computation required to solve multiple PDE</li> </ul>
SPM	$\frac{\partial c_s}{\partial t} = \frac{D_s}{r^2} \frac{\partial}{\partial r} \left( r^2 \frac{\partial c_s}{\partial r} \right)$ $j^{Li} = a_s i_0 \left[ \exp \left( \frac{\alpha_s F}{RT} \eta - \frac{R_{SEI}}{a_s} j^{Li} \right) - \exp \left( \frac{\alpha_c F}{RT} \eta - \frac{R_{SEI}}{a_s} j^{Li} \right) \right]$ $i_s = \beta_0 e^{-\lambda \delta} \exp(-E_a/RT) I$ $\frac{\partial \delta}{\partial t} = - \frac{i_s}{2F} \frac{M_{SEI}}{\rho_{SEI}}$	$R_{SEI}$ $i_s$ $\delta$	$I$ $T$	[32] [34] [40] [41] [42]	<ul style="list-style-type: none"> <li>Calculate side reactions current with Butler-Volmer equation</li> <li>Find SEI resistance growth rate with side reactions current</li> <li>Update electrode total current</li> </ul>	<ul style="list-style-type: none"> <li>✓ Requires less intense computation</li> <li>– Results are less accurate for higher C rates</li> </ul>

### 1.3 Cell Level Models

Degradation models in the material and electrode level include the governing electrochemical differential equations to simulate both the real-time performance and aging of the battery, as observed in the previous section. These equations are solved simultaneously and after each iteration, the parameters related to the aging such as cyclable lithium loss and

SEI resistance are updated. The material and electrode level models are mostly physics-based model to understand the internal functions of the cell and used in performance analysis of newer battery chemistry. However, in the cell level aging models, the battery cell is considered as an electrical equivalent circuit with time-variant elements. This approach is taken to use these models with in-conjunction with other engineering studies, i.e. control architecture development for the BMS. Scaling up from the material level to the cell level is changing the view from the electrochemical reactions inside the cell to the electrically measurable variable as voltage, impedance, ampere-hour (Ah) on the cell terminals. Thus, allowing the battery models to be analyzed and utilized with physically measurable quantities.

The battery degradation phenomena occur in both the storage and utilization modes. The aging associated with the storage period, “calendar aging” is dependent on the storage temperature, state of charge (SOC), and time as shown in (1-29) [46]–[48]. As the SOC of the battery and its terminal voltage are directly related, some literature has translated the battery SOC to its storage voltage [49], [50]. For the aging caused by the battery utilization, “cycle aging”, the effectual factors are ambient temperature, SOC, depth of discharge (DOD), charge/discharge current and number of cycles as given (1-30) [51]–[53].

$$Q_{cal.} = f(T, SOC, t) \quad (1-29)$$

$$Q_{cyc.} = g(T, SOC, DOD, I_{ch/dch}, N) \quad (1-30)$$

Here,  $Q_{cal.}$  and  $Q_{cyc.}$  refer to the percentage calendar and cycle capacity fade respectively. The calculation trend from the mentioned aging factor to the capacity and power losses is shown in Figure 1.5.

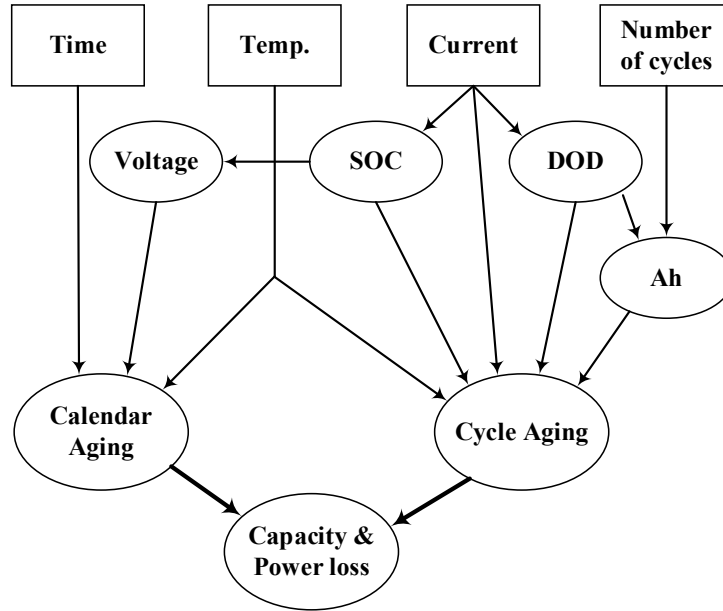


Figure 1.5. Degradation factors in the cell level models

Studies on the cell level aging modeling are empirically oriented and present fitted mathematical models to the data derived from extensive experimental data. These data are generated through both accelerated and non-accelerated testing methods for various battery technologies. Non-accelerated testing methods provide better results than accelerated testing. Regardless of the testing procedure, empirical models obtained through testing produces a considerable accurate result for a specific technology of battery. These results are deterministic in nature, providing a fixed value of capacity and power fade, as opposed to probabilistic answers, defined by a probability density function. Usually, these experimental data are fitted either with Arrhenius-like [49] or polynomial equation [53]. These two most popular cell level models are discussed here in detail. The choice of

mathematical model depended on the chemistry of the battery technology and the accuracy of the fitting.

### 1.3.1 Arrhenius Kinetic Based Models

Generally, most of the battery aging models obtained through empirical methods use the Arrhenius equation. Arrhenius equation dictates the relationship between the rate constant of a chemical reaction to major factors i.e. temperature, activation energy. Different researchers use this equation to relate the capacity and power fade of the battery with ambient temperature and time. Some variations and modifications are also performed in the base equation to accommodate the effect of SOC and Ah throughput. The rate constant  $k$  is defined by the Arrhenius equations as (1-31). Here,  $A$  is a pre-exponential factor,  $E_a$  is activation energy.

$$k = A \exp\left(-\frac{E_a}{RT}\right) \quad (1-31)$$

Empirically obtained models require extensive testing, which demands substantial time and resources. These tests are performed under accelerated aging conditions with elevated temperatures. Note that the higher temperature has a significant effect on the battery aging acceleration [53], as batteries are significantly affected by exothermic conditions. So, Bloom et al. [54] tested 18650 cells in temperatures above 40°C to investigate the calendar and cycle life of the battery. They used the general Arrhenius equation to fit the experimental data (1-32).

$$Q = B \exp\left(\frac{-E_a}{RT}\right) t^z \quad (1-32)$$

Here,  $B$  is a pre-exponential factor,  $t$  is time, and  $z$  is the power factor. The numerical values of these parameters for different test conditions are presented in [54]. Authors in [54] explain the battery capacity fade and power fade in both the calendar and cycle aging with a power law of time. Although the time is a reasonable variable in the calendar aging evaluation, the capacity fade due to the cycling is more dependent on the total Ampere-hour (Ah) throughput of the battery. In addition, in constant current charge and discharge cycles, the Ah throughput is directly related to the time. Therefore, authors in [55] altered the time to Ah in the Arrhenius equation to be able to study the effect of different C-rates on battery degradation. Based on their model, the pre-exponential factor and activation energy are a function of C-rate and the power factor is a constant value as given in (1-33). Ah in (1-33) can be calculated according to (1-34). In (1-33),  $C$  is the rated capacity of the battery cell and  $N$  is the number of cycles. Numerical data for  $B$  provided in [55] are adopted from fitting an exponential function of C-rate as given in (1-35) [56].

$$Q_{cyc.} = B \exp\left(\frac{-31700 + 370.3Crate}{RT}\right) Ah^{0.55} \quad (1-33)$$

$$Ah = N \cdot DOD \cdot C \quad (1-34)$$

$$\ln B = 1.226 \exp(-0.2797 Crate) + 9.263 \quad (1-35)$$

This model in (1-33) includes the effect of temperature, DOD, C-rate and number of cycles. However, it is not considering the impact of SOC. Authors in [57] present a similar



model relating the pre-exponential factor  $B$  to the SOC of the battery during cycling as shown in (1-36).

$$Q_{cyc.} = (\alpha SOC + \beta) \exp\left(\frac{-E_a + \eta \times C_{rate}}{RT}\right) Ah^z \quad (1-36)$$

Where, values for  $\alpha, \beta, \eta$ , and  $z$  can be found from [57]. These models are helpful to evaluate the battery health condition. However, they are valid only in identical repetitive conditions. Han et al. [8] have employed accumulated damage theory and modeled the battery degradation in each cycle which can be different from the previous cycling conditions. They have presented a discrete capacity fade model as shown in (1-37), (1-38), and (1-39). These equations calculate the capacity loss associated with each cycle. A cumulative of capacity fade for every cycle provides the aggregate capacity fade. The parameters used are generated from tests and it is a practical model that should be calibrated to avoid accumulated error due to the difference in the test and real-world conditions.

$$Q_{cyc.(1)} = B \exp\left(\frac{-E_a}{RT}\right) N, \quad N = 1 \quad (1-37)$$

$$Q_{cyc.(N+1)} = Q_{cyc.(N)} + k_1 \exp\left(\frac{k_2}{T}\right) Q_{cyc.(N)}^{k_3} \quad (1-38)$$

$$k_1 = zB^{\frac{1}{z}}, k_2 = -\frac{E_a}{zR}, k_3 = \frac{z-1}{z} \quad (1-39)$$

Another practical model that can be used for real-world battery degradation simulations is presented by Lam et al. [58] considering the effect of SOC, DOD, temperature and Ah throughput. Authors referred to [59] to calculate the average SOC,

$SOC_{avg}$  and its standard deviation,  $SOC_{dev}$  from the SOC profile of the battery after a cycling as given in (1-40) and (1-41).

$$SOC_{ave} = \frac{1}{Ah} \int_0^{Ah_T} SOC(Ah) dAh \quad (1-40)$$

$$SOC_{dev} = \sqrt{\frac{3}{Ah} \int_0^{Ah_T} (SOC(Ah) - SOC_{avg})^2 dAh} \quad (1-41)$$

Following Millner's work from [59], the capacity fade is calculated by the multiplication of exponentials of  $SOC_{avg}$  and  $SOC_{dev}$ . However, Lam's experimental results fitting shows an empirical function. By including the temperature effect, the capacity fade model is concluded as shown in (1-42). Where,  $k_1, k_2, k_3,$  and  $k_4$  are calculated from fitting the experimental results.

$$Q_{cyc.} = \sum_i^N \left( (k_1 SOC_{dev,i} \exp(k_2 SOC_{avg,i}) + k_3 \exp(k_4 SOC_{dev,i})) \exp\left(-\frac{E_a}{R} \left(\frac{1}{T_i} - \frac{1}{T_{ref}}\right)\right) \right) \cdot Ah_i \quad (1-42)$$

Arrhenius equation is used widely by different authors because of its considerable accuracy in defining capacity fade. This equation states that C-rate and temperature affect the capacity fade exponentially, while SOC is a pre-exponential factor. But this assumption is limited by battery technology and experimental conditions.

### 1.3.2 Polynomial Based Models

Although the temperature dependency in most of the aging models is indicated by the Arrhenius law, Omar et al. [60] claim that the Li-ion cells' characteristic is not completely exponential. Therefore, a polynomial function is used for calculating the number of cycles before the battery reached the end of life (EOL). These polynomial functions are developed from fitting results from extensive testing. Function for determining the number of cycles  $CL$  for the effect of temperature on the battery is given by (1-43).

$$CL(T) = k_1 T^3 + k_2 T^2 + k_3 T + k_4 \quad (1-43)$$

Similarly, they use the experimental data to fit exponential functions to include the effects of discharge current  $I_d$ , DOD, and charge current  $I_{ch}$  as given by (1-44), (1-45), and (1-46), respectively.

$$CL(I_d) = k_5 \exp(k_6 I_d) + k_7 \exp(k_8 I_d) \quad (1-44)$$

$$CL(DOD) = k_9 \exp(k_{10} DOD) + k_{11} \exp(k_{12} DOD) \quad (1-45)$$

$$CL(I_{ch}) = k_{13} \exp(k_{14} I_{ch}) + k_{15} \exp(k_{16} I_{ch}) \quad (1-46)$$

Here, parameters  $k_1$  to  $k_{16}$  are concluded from the fittings and can be found in [60]. Considering these equations as the core of the model, the authors evaluate the effect of each factor in each cycling and calculate the maximum number of cycling in different conditions.

Not all the aging models focus on the cycle aging, some studies explore the calendar aging specifically. Ecker et al. [49] suggest that the calendar aging is the square root of time while it is affected by the temperature and voltage which can be calculated by the experimental data fitting method used by [61], [62] for supercapacitor aging calculations. However, the calendar aging does not always change by the square root of the time. Different tests show that it may have a linear dependency to time or even a combination of both [52]. Considering both perspectives, battery calendar aging can be fitted to (1-47).

$$Q_{cal.} = k_1 t + k_2 \sqrt{t} \quad (1-47)$$

Where,  $k_1$  and  $k_2$  can represent the effect of the temperature and the SOC or voltage by an exponential function, polynomial function, or combination of both. Marongui et al. [50] considers capacity fade is dependent on the square root of time at  $k_1 = 0$ , and defined an exponential fitting function for  $k_2$  as given by (1-48). Here,  $V$  stands for battery storage voltage,  $T$  is the temperature. The parameters  $\alpha, \beta$ , and  $\lambda$  can be obtained from experimental data fitting.

$$k_2 = \alpha \exp\left(-\frac{\beta}{T}\right) \cdot \exp(\lambda V) \quad (1-48)$$

To present a more comprehensive study, authors in [48] considers both the calendar and cycle degradation to model total capacity fade  $Q$ . The calendar life part is based on the battery storage voltage  $V$ , temperature  $T$ , and storage time  $t$ . The cycle life consists of the effect of the average voltage  $V_{avg}$ , DOD and total Ah throughput. The parameters  $k_1$  to  $k_7$

are obtained through fitting to experimental tests in both storage and cycling modes. The equations for this model are given by (1-49), (1-50) and (1-51).

$$Q = Q_{cal.} + Q_{cyc.} = \alpha t^{0.75} + \beta Ah^{0.5} \quad (1-49)$$

$$\alpha = (k_1 V + k_2) \exp\left(\frac{k_3}{T}\right) \quad (1-50)$$

$$\beta = k_4 (V_{avg} + k_5)^2 + k_6 DOD + k_7 \quad (1-51)$$

Similarly, in [63], [64], Zabala et al. have modeled the calendar capacity fade of the battery cell by the storage SOC, temperature, and time. The cycling capacity fade was modeled by DOD, and Ah while keeping the C-rate, and SOC level constant. This model is given by (1-52), (1-53), and (1-54); it is derived for different DOD limits from the experimental results.

$$Q_{cal.} = k_1 \exp\left(\frac{k_2}{T}\right) \cdot k_3 \exp(k_4 SOC) \sqrt{t} \quad (1-52)$$

$$10\% \leq DOD \leq 50\%; \quad Q_{cyc.} = (k_5 DOD^2 + k_6 DOD + k_7) Ah^{0.87} \quad (1-53)$$

$$\begin{aligned} 10\% > DOD \text{ and } DOD > 50\%; \quad Q_{cyc.} &= (k_8 \exp(k_9 DOD) \\ &+ k_{10} \exp(k_{11} DOD)) Ah^{0.65} \end{aligned} \quad (1-54)$$

Here,  $k_1$  to  $k_{11}$  are fitted to best match the experimental data. In [65], an energy based aging model is presented that considers calendar and cycle aging. A new term as “state of energy (SOE)” is defined which is very similar to SOC. Total capacity fade in this

model is the sum of the calendar and cycle aging. Here the calendar life is a function of  $SOE$  and temperature as given by (1-55).

$$Q_{cal.} = Q_{cal.0} \exp\left(\frac{SOE - SOE_0}{k_1}\right) \cdot \exp\left(\frac{T - T_0}{k_2}\right) \sqrt{t} \quad (1-55)$$

Here,  $Q_{cal.0}$  is the nominal calendar capacity fade in the condition with  $SOE_0$  and  $T_0$ . The parameters  $k_1$  and  $k_2$  are fitting parameters. For the cycle aging, different cycles' accumulated capacity fade is considered. For each cycle, a polynomial function of change of  $SOE$  as expressed by (1-56) calculates the capacity fade. Also, parameter  $k_3$  to  $k_5$  are obtained through fitting experimental results.

$$Q_{cyc.} = \sum_i^N (k_3 \Delta SOE_i^3 + k_4 \Delta SOE_i^2 + k_5 \Delta SOE_i) \quad (1-56)$$

### 1.3.3 Summarizing Degradation Models at Cell Level

Figure 1.6 summarizes the cell level degradation models like previous material and electrode level. It describes the essence of most of the models available in the current literature. The current and temperature are the input variables in the cell level models. OCV and circuit elements (R, L, and C) are obtained from the experiments as functions of SOC and temperature. SOC from the performance model is used besides the current and temperature to calculate the degradation and update the capacity. Degradation models will modify the battery performance model by varying the battery internal impedance parameters and capacity, which will result in a variation of the battery terminal voltage.

As observed, cell level degradation models rely on the experimental results and therefore, they are valid only for the specific battery technology and defined test conditions. Although these models are easy to simulate and reduce the computational load, they are less accurate compared to the material level models. One way to improve the accuracy of these models is to recalibrate the model parameters for any specific condition. To compare the mathematical models in cell level studies considering only cycle aging, they are presented in Table 1.2 with their references. The research work solely based on calendar aging and calendar aging combined with cycle aging are discussed in Table 1.3. These tables contain the key variables, required measurements, technologies, form factor, calculation process, and pro-cons of using each model are illustrated for a better understanding of these models.

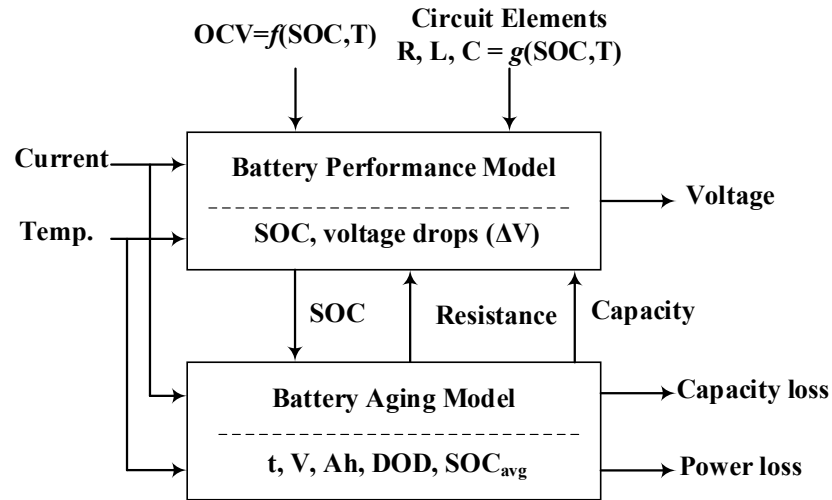


Figure 1.6. The basic idea of cell level degradation models

Table 1.2. Summary of cell level degradation models

Major Mathematical Expressions Involved	Variables	Meas.	Ref.	Tech & Form	Calculation Process	Pros and Cons
$Q_{cyc.}$ $= B \exp\left(\frac{-31700 + 370.3 \times C-rate}{RT}\right) Ah^{0.55}$ $\ln B = 1.226 \exp(-0.2797 C-rate) + 9.263$	C-rate	Ah T	[46]– [48]	LFP 18650 26650	<ul style="list-style-type: none"> <li>• Calculate C-rate for each cycle</li> <li>• Find the capacity fade percentage</li> <li>• Update capacity after each cycle</li> </ul>	<ul style="list-style-type: none"> <li>✓ Using Ah instead of time</li> <li>– Accelerated test reduce the accuracy</li> </ul>
$Q_{cyc.}$ $= (\alpha SOC + \beta) \exp\left(\frac{-E_a + \eta \times C-rate}{RT}\right) Ah^z$	SOC C-rate	Ah T	[49]	LFP 26650	<ul style="list-style-type: none"> <li>• Calculate SOC and C-rate</li> <li>• Find the capacity fade percentage</li> </ul>	<ul style="list-style-type: none"> <li>✓ The exponent of Ah is variable</li> <li>✓ Pre-exponent considers the effect of SOC</li> <li>– Incorrect determination of Ah throughput</li> </ul>
$Q_{cyc.(N+1)}$ $= Q_{cyc.(N)} + k_1 \exp\left(\frac{k_2}{T}\right) \cdot Q_{cyc.(N)}^{k_3}$ $k_1 = zB^{\frac{1}{z}}, k_2 = -\frac{E_a}{zR}, k_3 = \frac{z-1}{z}$	N	T	[50]	NMC LFP LMO	<ul style="list-style-type: none"> <li>• Count number of cycles</li> <li>• Calculate capacity fade for each cycle with subsequent results</li> </ul>	<ul style="list-style-type: none"> <li>✓ Discrete aging meas.</li> <li>– Needs recalibration for real-world data</li> </ul>
$Q_{cyc.}$ $= \sum_i^N \left( \left( k_1 SOC_{dev,i} \exp(k_2 SOC_{avg,i}) \right) + k_3 \exp(k_4 SOC_{dev,i}) \right) \times \exp\left(-\frac{E_a}{R} \left( \frac{1}{T_i} - \frac{1}{T_{ref}} \right) \right)$ $\times Ah_i$	$SOC_{dev}$ $SOC_{avg}$	Ah T	[51], [52]	LFP 18650 26650	<ul style="list-style-type: none"> <li>• In cycle, find average SOC and DOD</li> <li>• Calculate capacity fade for cycle</li> <li>• Accumulate for number of cycles</li> </ul>	<ul style="list-style-type: none"> <li>✓ SOC and polynomial based aging</li> <li>– Limited to a specific technology</li> </ul>
$CL(T) = k_1 T^3 + k_2 T^2 + k_3 T + k_4$ $CL(I_d) = k_5 \exp(k_6 I_d) + k_7 \exp(k_8 I_d)$ $CL(DOD) = k_9 \exp(k_{10} DOD) + k_{11} \exp(k_{12} DOD)$ $CL(I_{ch}) = k_{13} \exp(k_{14} I_{ch}) + k_{15} \exp(k_{16} I_{ch})$	$I_d, I_{ch}$ $DOD, T$	$I_d$ $I_{ch}$ $DOD$ T	[53]	LFP	<ul style="list-style-type: none"> <li>• Calculate the effect of each factor</li> <li>• Accumulate results</li> <li>• Find maximum cycle number to EOL</li> </ul>	<ul style="list-style-type: none"> <li>✓ Effect of multiple parameters on aging</li> <li>– Constant C rates used in aging</li> </ul>



Table 1.3. Summary of cell level degradation models for calendar aging

Type	Major Mathematical Expressions Involved	Variables	Meas.	Ref.	Tech Form	Calculation Process	Pros and Cons
Calendar Degradation	$Q_{cal.} = \alpha \exp\left(-\frac{\beta}{T}\right) \cdot \exp(\lambda V) \sqrt{t}$	$V$	$T$ $t$	[42] [43] [44]	NMC LFP	<ul style="list-style-type: none"> <li>Measure storage voltage and temperature</li> <li>Calculate capacity fade in time</li> </ul>	<ul style="list-style-type: none"> <li>✓ Considers both time and effect of temp</li> <li>– Aging determined in terms of voltage only</li> </ul>
	$Q = Q_{cal.} + Q_{cyc.} = \alpha t^{0.75} + \beta Ah^{0.5}$ $\alpha = (k_1 V + k_2) \exp\left(\frac{k_3}{T}\right)$ $\beta = k_4 (V_{avg} + k_5)^2 + k_6 DOD + k_7$	$V$ $V_{avg}$ $DOD$	$Ah$ $T$ $t$	[41]	NMC 18650	<ul style="list-style-type: none"> <li>Measure storage voltage and temperature</li> <li>Find cycling average voltage</li> <li>Calculate calendar and cycle aging</li> </ul>	<ul style="list-style-type: none"> <li>✓ Determined both calendar and cycle aging</li> <li>– Limited to a specific tech</li> </ul>
Cycle and Calendar Degradation	$Q_{cal.} = k_1 \exp\left(\frac{k_2}{T}\right) \cdot k_3 \exp(k_4 SOC) \sqrt{t}$ <p>if <math>10 \leq DOD \leq 50</math>:</p> $Q_{cyc.} = (k_5 DOD^2 + k_6 DOD + k_7) Ah^{0.87}$ <p>if <math>10 &gt; DOD</math> and <math>DOD &gt; 50</math>:</p> $Q_{cyc.} = (k_8 \exp(k_9 DOD) + k_{10} \exp(k_{11} DOD)) Ah^{0.65}$	$SOC$ $DOD$	$Ah$ $T$ $t$	[56], [57]	LFP 26650	<ul style="list-style-type: none"> <li>Calculate SOC and DOD</li> <li>Use SOC to calculate calendar aging</li> <li>Determine DOD range</li> <li>Use DOD to calculate cycle aging</li> </ul>	<ul style="list-style-type: none"> <li>✓ Considering the effect of Ah, temperature and time</li> <li>– SOC and C-rates are kept constant during testing</li> </ul>
	$Q_{cal.} = Q_{cal.0} \exp\left(\frac{SOE - SOE_0}{k_1}\right)$ $\times \exp\left(\frac{T - T_0}{k_2}\right) \sqrt{t}$ $Q_{cyc.} = \sum_i^N (k_3 \Delta SOE_i^3 + k_4 \Delta SOE_i^2 + k_5 \Delta SOE_i)$	$SOE$ $N$	$T$ $t$	[58]	LFP	<ul style="list-style-type: none"> <li>Calculate the State of Energy</li> <li>Count number of cycles</li> <li>Calculate calendar aging with SOE</li> <li>Calculate cycle aging with <math>\Delta SOE</math> and <math>N</math></li> </ul>	<ul style="list-style-type: none"> <li>✓ SOE based aging</li> <li>– Limited to a specific tech</li> </ul>

## 1.4 Module and Pack Level Models

A single Li-ion battery cell has limited power and capacity. Thus, for the high power and energy applications, the cells are connected in series or parallel configurations to form battery modules and pack with increased voltage, current, and stored energy capability. However, internal differences among the cells of a module or a pack are unavoidable. The source of this difference can be either the difference in the cells' production process or

different working conditions such as temperature and loading [66]. Among 20,000 fresh cells, measured initial capacity has a normal distribution with a 1.3% deviation. Direct current internal resistance result for these cells has the same distribution with 5.8% deviation [67].

This phenomenon leads to inhomogeneous aging in the connected cells of a module or pack. For instance, two parallel-connected cells with a 20% difference in the internal resistance experience 40% higher peak currents [68] compared to the case that two cells work dependently. These increased current peaks cause extra heat production in the cell. Also, the location of the cell inside the module and pack affects its heat dissipation and changes the cell temperature [69]. Therefore, boosted current and temperature causes expedited aging in these cells, referring to the aging models of the previous section. Based on Gogoana et al., a 20% difference in the internal resistance of a pair of parallel cells can reduce the cycle life of both cells by 40 % [70]. In the series connected cells, the expediting aging factor is temperature, as the currents in series-connected cells are equal.

Considering this discussion, aging models developed for the cell level are not adequate to predict the aging behavior of a module or a pack due to variations inside the pack. Pack simulation from the cell model is valid only if the cell-to-cell variations are considered [71]. The first step in solving the problem is to calculate/estimate the amount of imbalance between the cells to have a quantitative understanding of the different working conditions for the cells. “State of Balance” is a concept presented by Wang et al. [66] to estimate the cells' imbalance for dynamic equalization adjustment. One major imbalance factor is temperature which causes a mismatch on the cell resistance leading to

unbalanced currents and different aging behavior. During the discharge of a module with parallel cells, cells with higher temperature have higher current extraction until 75% DOD. After that, the current falls until 90% DOD and then rises again to the end of discharge. This result shows a significant impact of temperature in cells' performance, reported in [72]. The authors indicate a linear relationship between the capacity fade difference and the temperature difference between cells.

To better understand the aging difference in a single cell and the pack Lebel et al. [73] explored the parallel-connected cells aging by an electro-thermal model. Incremental capacity analysis (ICA) is reported to be a suitable tool for the study of the difference in cell and pack capacity fade due to variation in the internal resistance, temperature [74], [75]. Kalogiannis et al. [76] report results at different discharge rates and reference authors performing ICA for lithium iron phosphate, lithium nickel manganese, and lithium titanate oxide technologies. However, reports on these technologies are experimental and not formally described with a mathematical equation that can be reproduced for other battery packs.

The next step is to bridge the gap between cell aging models and module/pack degradation calculations. In a battery pack with parallel and series cells, the basic approach is to neglect the current imbalance in the parallel cells and consider them as a bigger cell due to the passive balance control. Then, it is possible to calculate the aging for the series cells considering their working condition by updating the cell aging model using the SOC and state of health (SOH) information from the pack. At this point, deciding about the pack capacity fade from cells' aging information can follow different methods [77]–[79].

The simplest method is to select the most aged cell as the representative of the whole pack and calculate the pack capacity fade as follows [80], [81]. This considers exclusively serially-connected cells as given by (1-57).

$$Q_p = \max Q_{c,i} \quad i = 1:M \quad (1-57)$$

Here each cell's capacity fade is  $Q_{c,i}$ , and the number of cells is  $M$ . The disadvantage of this method is that it overestimates the pack capacity fade. Taking the average of cells capacity fade for the pack degradation estimation is another approach that underestimates the total capacity fade. Therefore, authors in [67], [79] suggest using probabilistic aging estimation, which finds the probability distribution of cells capacity and presents the whole pack capacity by a probability distribution function. However, the results show that although the estimation error is improved, this method still underestimates the pack degradation, slightly.

Other module and pack level aging determination methods consider that the battery is already deployed in an application. In most cases, these applications are related to electric, hybrid electric vehicles, grid, and residential application. In such cases, it is not possible to remove the battery from that application and test to determine degradation frequently. The aging must be determined while the battery is being utilized, or online. Therefore, these methods are used to simplify the aging estimation with minimum measurement and test requirements. Note that such studies do not present mathematical aging models for simulation purposes and they focus on the estimation methods to be implemented in real-life battery applications.

The main objective of these methods is to estimate the aging while the battery is online. This can be categorized into two groups: experimentally oriented and adaptive methods [82]. The experimental methods measure and store the aging related variables and calculate the aging in each state of life of the battery using simplified aging models and historical logged data. Resistance measurement in different current signals [83], joule effect which is the generated heat by the internal resistance [84] and Ah throughput counting [85], [86] are some of these approaches.

Remmlinger et al. [87] proposed a resistance estimation method using a specific current signal detection while the battery is working and measuring the voltage for resistance calculation. Ah throughput counting method using the aging model presented in [51] is another study presented in [88]. As the working condition of a battery, such as loading and temperature change during its life, the total Ah count rises the aging estimation error. Therefore, Marano et al. [89] suggested using effective Ah counting which defines weighting coefficients for each Ah considering the different working conditions. Although these methods have low computational burdens and are easy to implement in the battery management system, they require large data storing capacity and, they have less accuracy due to the accumulated error over time.

To prevent the bulk measurement of the aging related parameter and data storage problem, it is possible to reduce the measurements and computations by sampling a small group of the cells [90]. In this method, a new circuit topology of the battery pack is needed which separates it into two tests and main groups. The circuit configuration is designed in such a way that while the main group is working, the test group cells can be separated by

relays and measurements can be performed without disturbing the function of the battery. This method simplifies and reduces the computational burden with the cost of slightly lowering the accuracy.

## **1.5 Probabilistic Degradation Models**

Even with large data sets detailing the battery behavior, online pack and module level aging determination generate results with large error margins. It is because such estimation methods are deterministic in nature while relying on results obtained through a controlled experiment in a lab. It is nearly impossible to replicate the exact application scenario during the associated testing procedure. So, the deterministic results obtained will be inherently erroneous, because of the inability to predict the load applied on the battery by a specific application. Therefore, researchers are moving towards a more probabilistic approach to determine degradation.

These probabilistic-based studies mainly use adaptive methods that calculate the parameters sensitive to the aging such as resistance and estimate the life of the battery from those calculations. These methods eliminate the need for bulk measurements and simulations of the battery performance. For this purpose, they use different algorithms such as Kalman filter [91] and its improved versions, observers [92], fuzzy logic [93], artificial neural networks [94], and linear least squares [95]. All these methods can target specific aging related parameters in the battery. For example, Gholizadeh et al. [96] have used a sliding mode type observer (SMO) and Remmlinger et al. [97] employed linear parameter-varying (LPV) model on series resistance measurements. They have used general

measurements that are available in the BMS. In [98], Kalman filter is applied for aging estimation by cell capacitance from Randles' equivalent circuit model and it is shown that the aging of the battery has a non-linear relationship with that capacitive property. However, these models typically quantify aging but disregard the causes of aging beyond the battery parameters.

## 1.6 Conclusion

This chapter classified the models into different scales and analyzed each model by presenting its mathematical expression, key variables, required measurements, and calculation process. At the material level, the literature is well established through the physics-based governing equations based on porous theory. Model order reduction and simplifications such as single particle models are widely used to improve the usability of these models. However, these models could benefit from probabilistic approaches that consider variations in active surfaces, and ratios of electrode-electrolyte volumes.

At the cell level, findings show that researchers report their aging models with varying degrees of disclosure. For example, only a sub-set of researchers presented the cell technology and form factor. Also, aging studies are mostly reported based on laboratory experiments, but the field is clearly moving towards real application-based data. Increased data availability through cloud-based databases will radically increase the resources available to generate aging models.

At the module and pack level, most of the work is focused on identifying variations in cell capacities and voltages. However, some methods are developed for the

series/parallel combination of the pack studied, which makes it difficult to adopt for other packs. Also, at the module and pack level, our findings show a heightened interest in probabilistic approaches that can be driven by real application data. However, there are not enough studies that reach beyond a single scale and particularly none that tie them probabilistically.

This literature review served the basis for obtaining a solid understanding of battery characteristics and aging models used to predict battery degradation. This dissertation focuses on developing a probabilistic approach through a hierarchical Bayesian Network to evaluate battery degradation. The hierarchical Bayesian Network requires a deterministic function that relates battery degradation to intermediate variables, i.e. SOC, Ah throughput, C-rate, etc. Later these intermediate variables can be related to external causal factors. For the cell level, a suitable function is a modified Arrhenius equation given in (1-36). This equation will be utilized in later sections to define the battery capacity during Bayesian Network development.

The summary and qualitative comparison of degradation models and methods in different scales are given in Table 1.4.



Table 1.4. Summary of battery degradation models

Scale	Factor	Application	Target and Purpose	Pros and Cons
Material and Electrode Level	<ul style="list-style-type: none"> <li>• Cyclable Li loss</li> <li>• Resistance rise</li> <li>• Effective surface loss</li> <li>• Loss of active materials</li> </ul>	<ul style="list-style-type: none"> <li>• Electrochemical modeling</li> <li>• Material improvement</li> <li>• Cell design</li> <li>• New battery technology</li> </ul>	<ul style="list-style-type: none"> <li>• To evaluate and test the capabilities of a new technology of battery before mass production</li> </ul>	<ul style="list-style-type: none"> <li>✓ Detailed modeling</li> <li>✓ No time-consuming experiments</li> <li>– Complicated</li> <li>– High computational burden</li> </ul>
Cell Level	<ul style="list-style-type: none"> <li>• Storage temperature</li> <li>• Storage SOC</li> <li>• Cycling temperature</li> <li>• Cycling SOC and DOD</li> <li>• Cycling current</li> <li>• Total Ah and time</li> </ul>	<ul style="list-style-type: none"> <li>• Battery performance</li> <li>• Lab experiments</li> <li>• Simulation for different conditions</li> </ul>	<ul style="list-style-type: none"> <li>• Understand the system level performance of a technology</li> <li>• Characterize different form factors</li> <li>• Find proper applications</li> </ul>	<ul style="list-style-type: none"> <li>✓ Simple modeling</li> <li>✓ Easy to implement</li> <li>✓ Low computational burden</li> <li>– Limited to its specific test condition</li> <li>– Requires extensive test data</li> </ul>
Module and Pack Level	<ul style="list-style-type: none"> <li>• Cells' manufacturing differences</li> <li>• Cells' configurations (series, parallel)</li> <li>• Temperature variations inside module and pack</li> <li>• Usage pattern difference</li> <li>• External factors variations</li> </ul>	<ul style="list-style-type: none"> <li>• Cell balancing</li> <li>• Temperature distribution</li> <li>• BMS design</li> <li>• On-board estimations</li> <li>• Real-time application</li> <li>• Control purposes</li> </ul>	<ul style="list-style-type: none"> <li>• Design a module or pack for an application</li> <li>• Manage battery in real-time</li> <li>• Control system designing based on battery characteristics</li> </ul>	<ul style="list-style-type: none"> <li>✓ Simple modeling</li> <li>✓ Applicable to real cases</li> <li>✓ Simple implementation</li> <li>✓ Applicable to any technology</li> <li>✓ No time-consuming experiments</li> <li>– Hard to track the cell difference</li> <li>– Complicated temperature distribution</li> <li>– Accumulated error issue</li> <li>– Data storage problem</li> </ul>
Probabilistic Models	<ul style="list-style-type: none"> <li>• Considers all factors from all scales</li> </ul>	<ul style="list-style-type: none"> <li>• Electrochemical modeling</li> <li>• Battery performance</li> <li>• Temperature distribution</li> </ul>	<ul style="list-style-type: none"> <li>• Develop a non-deterministic degradation model</li> </ul>	<ul style="list-style-type: none"> <li>✓ Requires less testing data</li> <li>✓ Faster implementation</li> <li>– Computationally requirement</li> <li>– Choice of prior</li> </ul>

## References

- [1] A. Yoshino, "The birth of the lithium-ion battery," *Angewandte Chemie - International Edition*, vol. 51, no. 24. pp. 5798–5800, 2012.
- [2] D. T. Gladwin and C. R. Gould, "Viability of ' second-life ' use of electric and hybrid- electric vehicle battery packs," *IECON 2013 - 39th Annu. Conf. IEEE Ind. Electron. Soc.*, vol. Vienna, Au, pp. 1922–1927, 2013.

- [3] P. J. Hart, P. J. Kollmeyer, L. W. Juang, R. H. Lasseter, and T. M. Jahns, "Modeling of second-life batteries for use in a CERTS microgrid," in *2014 Power and Energy Conference at Illinois (PECI)*, 2014, pp. 1–8.
- [4] D. Strickland, L. Chittock, D. A. Stone, M. P. Foster, and B. Price, "Estimation of Transportation Battery Second Life for Use in Electricity Grid Systems," *IEEE Trans. Sustain. Energy*, vol. 5, no. 3, pp. 795–803, 2014.
- [5] L. C. Casals, B. A. García, F. Aguesse, and A. Iturrondobeitia, "Second life of electric vehicle batteries: relation between materials degradation and environmental impact," *International Journal of Life Cycle Assessment*, 2015.
- [6] B. Pilvelait, C. Rentel, G. L. Plett, M. Marcel, and D. Carmen, "An Advanced Battery Management System for Lithium Ion Batteries," *Ndia Gr. Veh. Syst. Eng. Technol. Symp.*, pp. 1–7, 2011.
- [7] K. B. Hatzell, A. Sharma, and H. K. Fathy, "A survey of long-term health modeling, estimation, and control of Lithium-ion batteries: Challenges and opportunities," *Am. Control Conf.*, pp. 584–591, 2012.
- [8] X. Han, M. Ouyang, L. Lu, and J. Li, "A comparative study of commercial lithium ion battery cycle life in electric vehicle: Capacity loss estimation," *J. Power Sources*, vol. 268, no. 0, pp. 658–669, 2014.
- [9] S. Pelletier, O. Jabali, G. Laporte, and M. Veneroni, "Battery degradation and behaviour for electric vehicles: Review and numerical analyses of several models," *Transp. Res. Part B Methodol.*, vol. 103, pp. 158–187, 2017.
- [10] M. Doyle, T. F. Fuller, and J. Newman, "Modeling Of Galvanostatic Charge And Discharge Of The Lithium Polymer Insertion Cell," *J. Electrochem. Soc.*, vol. 140, no. 6, pp. 1526–1533, 1993.
- [11] J. Newman and W. Tiedemann, "Porous-electrode Theory with Battery Applications," *Am. Inst. Chem. Eng.*, vol. 21, no. 1, pp. 25–41, 1975.
- [12] P. Northrop, M. Pathak, D. Rife, S. De, S. Santhanagopalan, and V. Subramanian, "Efficient Simulation and Model Reformulation of Two-Dimensional Electrochemical Thermal Behavior of Lithium-Ion Batteries," *J. Electrochem. Soc.*, vol. 162, pp. 940–951, 2015.
- [13] F. Joho, P. Novák, and M. E. Spahr, "Safety Aspects of Graphite Negative Electrode Materials for Lithium-Ion Batteries," *J. Electrochem. Soc.*, vol. 149, no. 8, pp. A1020–A1024, 2002.
- [14] Y. P. Wu, E. Rahm, and R. Holze, "Carbon anode materials for lithium ion batteries," *J. Power Sources*, vol. 114, no. 2, pp. 228–236, 2003.

- [15] P. Arora, "Capacity Fade Mechanisms and Side Reactions in Lithium-Ion Batteries," *J. Electrochem. Soc.*, vol. 145, no. 10, p. 3647, 1998.
- [16] R. Imhof, "In Situ Investigation of the Electrochemical Reduction of Carbonate Electrolyte Solutions at Graphite Electrodes," *J. Electrochem. Soc.*, vol. 145, no. 4, p. 1081, 1998.
- [17] H. Buqa, A. Würsig, J. Vetter, M. E. Spahr, F. Krumeich, and P. Novák, "SEI film formation on highly crystalline graphitic materials in lithium-ion batteries," in *Journal of Power Sources*, 2006, vol. 153, no. 2, pp. 385–390.
- [18] K. Amine *et al.*, "Factors responsible for impedance rise in high power lithium ion batteries," in *Journal of Power Sources*, 2001, vol. 97–98, pp. 684–687.
- [19] J. Y. Song, H. H. Lee, Y. Y. Wang, and C. C. Wan, "Two- and three-electrode impedance spectroscopy of lithium-ion batteries," *J. Power Sources*, vol. 111, no. 2, pp. 255–267, 2002.
- [20] M. Broussely, S. Herreyre, P. Biensan, P. Kasztejna, K. Nechev, and R. J. Staniewicz, "Aging mechanism in Li ion cells and calendar life predictions," in *Journal of Power Sources*, 2001, vol. 97–98, pp. 13–21.
- [21] G. E. Blomgren, "Electrolytes for advanced batteries," *J. Power Sources*, vol. 81–82, pp. 112–118, 1999.
- [22] M. Koltypin, D. Aurbach, L. Nazar, and B. Ellis, "More on the performance of LiFePO<sub>4</sub> electrodes - The effect of synthesis route, solution composition, aging, and temperature," *J. Power Sources*, vol. 174, no. 2, pp. 1241–1250, 2007.
- [23] O. Erdinc, B. Vural, and M. Uzunoglu, "A dynamic lithium-ion battery model considering the effects of temperature and capacity fading," in *2009 International Conference on Clean Electrical Power, ICCEP 2009*, 2009, pp. 383–386.
- [24] Q. Zhang and R. E. White, "Capacity fade analysis of a lithium ion cell," *J. Power Sources*, vol. 179, no. 2, pp. 793–798, 2008.
- [25] S. S. Zhang, K. Xu, and T. R. Jow, "The low temperature performance of Li-ion batteries," *J. Power Sources*, vol. 115, no. 1, pp. 137–140, 2003.
- [26] Y. Wang, X. Guo, S. Greenbaum, J. Liu, and K. Amine, "Solid Electrolyte Interphase Formation on Lithium-Ion Electrodes: A [<sup>sup</sup> 7]Li Nuclear Magnetic Resonance Study," *Electrochem. Solid-State Lett.*, vol. 4, no. 6, p. A68, 2001.
- [27] D. Aurbach, B. Markovsky, A. Rodkin, M. Cojocaru, E. Levi, and H. J. Kim, "An analysis of rechargeable lithium-ion batteries after prolonged cycling," *Electrochim. Acta*, vol. 47, no. 12, pp. 1899–1911, 2002.

- [28] M. Broussely *et al.*, “Main aging mechanisms in Li ion batteries,” in *Journal of Power Sources*, 2005, vol. 146, no. 1–2, pp. 90–96.
- [29] M. Kerlau, M. Marcinek, V. Srinivasan, and R. M. Kostecki, “Studies of local degradation phenomena in composite cathodes for lithium-ion batteries,” *Electrochim. Acta*, vol. 52, no. 17, pp. 5422–5429, May 2007.
- [30] K. Amine, J. Liu, and I. Belharouak, “High-temperature storage and cycling of C-LiFePO<sub>4</sub>/graphite Li-ion cells,” *Electrochem. commun.*, vol. 7, no. 7, pp. 669–673, 2005.
- [31] M. Wohlfahrt-Mehrens, C. Vogler, and J. Garche, “Aging mechanisms of lithium cathode materials,” in *Journal of Power Sources*, 2004, vol. 127, no. 1–2, pp. 58–64.
- [32] J. Vetter *et al.*, “Ageing mechanisms in lithium-ion batteries,” *J. Power Sources*, vol. 147, no. 1–2, pp. 269–281, 2005.
- [33] W. B. Gu and C. Y. Wang, “Thermal-Electrochemical Modeling of Battery Systems,” *J. Electrochem. Soc.*, vol. 147, no. 8, p. 2910, 2000.
- [34] C. Delacourt and M. Safari, “Mathematical Modeling of Aging of Li-Ion Batteries,” in *Physical Multiscale Modeling and Numerical Simulation of Electrochemical Devices for Energy Conversion and Storage*, 2016.
- [35] R. Xu and K. Zhao, “Electrochemomechanics of Electrodes in Li-Ion Batteries: A Review,” *J. Electrochem. Energy Convers. Storage*, vol. 13, no. 3, pp. 1–9, 2016.
- [36] A. V. Randall, R. D. Perkins, X. Zhang, and G. L. Plett, “Controls oriented reduced order modeling of solid-electrolyte interphase layer growth,” *J. Power Sources*, vol. 209, pp. 282–288, 2012.
- [37] J. Fuller, Thomas F. Doyle, Marc. Newman, “Simulation and Optimization of the Dual Lithium Ion Insertion Cell,” *J. Electrochem. Soc.*, vol. 141, no. 1, p. 1, 1994.
- [38] M. Doyle, J. Newman, and J. Reimers, “A quick method of measuring the capacity versus discharge rate for a dual lithium-ion insertion cell undergoing cycling,” *J. Power Sources*, vol. 52, no. 2, pp. 211–216, 1994.
- [39] S. K. Rahimian, S. Rayman, and R. E. White, “Extension of physics-based single particle model for higher chargedischarge rates,” *J. Power Sources*, vol. 224, pp. 180–194, 2013.
- [40] M. Safari, M. Morcrette, a. Teyssot, and C. Delacourt, “Multimodal Physics-Based Aging Model for Life Prediction of Li-Ion Batteries,” *J. Electrochem. Soc.*, vol. 156, no. 3, p. A145, 2009.

- [41] J.-F. Li, Y.-S. Lin, C.-H. Lin, and K.-C. Chen, "Three-Parameter Modeling of Nonlinear Capacity Fade for Lithium-Ion Batteries at Various Cycling Conditions," *J. Electrochem. Soc.*, vol. 164, no. 12, pp. A2767–A2776, 2017.
- [42] G. Ning, R. E. White, and B. N. Popov, "A generalized cycle life model of rechargeable Li-ion batteries," *Electrochim. Acta*, vol. 51, no. 10, pp. 2012–2022, 2006.
- [43] T. R. Tanim and C. D. Rahn, "Aging formula for lithium ion batteries with solid electrolyte interphase layer growth," *J. Power Sources*, vol. 294, pp. 239–247, 2015.
- [44] G. Fan, K. Pan, and M. Canova, "A comparison of model order reduction techniques for electrochemical characterization of Lithium-ion batteries," *2015 54th IEEE Conf. Decis. Control*, vol. 2016-Febru, no. Cdc, pp. 3922–3931, 2015.
- [45] K.-C. Chiu, C.-H. Lin, S.-F. Yeh, Y.-H. Lin, C.-S. Huang, and K.-C. Chen, "Cycle life analysis of series connected lithium-ion batteries with temperature difference," *J. Power Sources*, vol. 263, pp. 75–84, 2014.
- [46] E. Prada, D. Di Domenico, Y. Creff, J. Bernard, V. Sauvant-Moynot, and F. Huet, "Simplified Electrochemical and Thermal Model of LiFePO<sub>4</sub>-Graphite Li-Ion Batteries for Fast Charge Applications," *J. Electrochem. Soc.*, vol. 159, no. 9, pp. A1508–A1519, 2012.
- [47] M. Petit, E. Prada, and V. Sauvant-Moynot, "Development of an empirical aging model for Li-ion batteries and application to assess the impact of Vehicle-to-Grid strategies on battery lifetime," *Appl. Energy*, vol. 172, pp. 398–407, 2016.
- [48] J. Schmalstieg, S. Käbitz, M. Ecker, and D. U. Sauer, "A holistic aging model for Li(NiMnCo)O<sub>2</sub> based 18650 lithium-ion batteries," *J. Power Sources*, vol. 257, no. 0, pp. 325–334, 2014.
- [49] M. Ecker *et al.*, "Development of a lifetime prediction model for lithium-ion batteries based on extended accelerated aging test data," *J. Power Sources*, vol. 215, pp. 248–257, 2012.
- [50] A. Marongiu, M. Roscher, and D. U. Sauer, "Influence of the vehicle-to-grid strategy on the aging behavior of lithium battery electric vehicles," *Appl. Energy*, vol. 137, pp. 899–912, 2015.
- [51] Y. Zhang, C. Y. Wang, and X. Tang, "Cycling degradation of an automotive LiFePO<sub>4</sub> lithium-ion battery," *J. Power Sources*, vol. 196, no. 3, pp. 1513–1520, 2011.
- [52] W. Waag, S. Käbitz, and D. U. Sauer, "Experimental investigation of the lithium-

ion battery impedance characteristic at various conditions and aging states and its influence on the application,” *Appl. Energy*, vol. 102, pp. 885–897, 2013.

- [53] H. Song *et al.*, “Capacity fade of LiFePO<sub>4</sub>/graphite cell at elevated temperature,” *J. Solid State Electrochem.*, vol. 17, no. 3, pp. 599–605, 2013.
- [54] I. Bloom *et al.*, “An accelerated calendar and cycle life study of Li-ion cells,” *J. Power Sources*, vol. 101, no. 2, pp. 238–247, 2001.
- [55] J. Wang *et al.*, “Cycle-life model for graphite-LiFePO<sub>4</sub> cells,” *J. Power Sources*, vol. 196, no. 8, pp. 3942–3948, 2011.
- [56] J. Shen, S. Dusmez, and a Khaligh, “Optimization of Sizing and Battery Cycle Life in Battery/UC Hybrid Energy Storage System for Electric Vehicle Applications,” *Ind. Informatics, IEEE Trans.*, vol. PP, no. 99, p. 1, 2014.
- [57] G. Suri and S. Onori, “A control-oriented cycle-life model for hybrid electric vehicle lithium-ion batteries,” *Energy*, vol. 96, pp. 644–653, 2016.
- [58] L. Lam and P. Bauer, “Practical capacity fading model for Li-ion battery cells in electric vehicles,” *IEEE Trans. Power Electron.*, vol. 28, no. 12, pp. 5910–5918, 2013.
- [59] A. Millner, “Modeling lithium ion battery degradation in electric vehicles,” *2010 IEEE Conf. Innov. Technol. an Effic. Reliab. Electr. Supply, CITRES 2010*, pp. 349–356, 2010.
- [60] N. Omar *et al.*, “Lithium iron phosphate based battery – Assessment of the aging parameters and development of cycle life model,” *Appl. Energy*, vol. 113, no. 0, pp. 1575–1585, 2014.
- [61] O. Bohlen, J. Kowal, and Dirk Uwe Sauer, “Ageing behaviour of electrochemical double layer capacitors. Part II. Lifetime simulation model for dynamic applications,” *J. Power Sources*, vol. 173, no. 1, pp. 626–632, 2007.
- [62] O. Bohlen, J. Kowal, and D. U. Sauer, “Ageing behaviour of electrochemical double layer capacitors. Part I. Experimental study and ageing model,” *J. Power Sources*, vol. 172, no. 1, pp. 468–475, 2007.
- [63] E. Sarasketa-Zabala, E. Martinez-Laserna, M. Berecibar, I. Gandiaga, L. M. Rodriguez-Martinez, and I. Villarreal, “Realistic lifetime prediction approach for Li-ion batteries,” *Appl. Energy*, vol. 162, pp. 839–852, 2016.
- [64] E. Sarasketa-Zabala, I. Gandiaga, E. Martinez-Laserna, L. M. Rodriguez-Martinez, and I. Villarreal, “Cycle ageing analysis of a LiFePO<sub>4</sub>/graphite cell with dynamic model validations: Towards realistic lifetime predictions,” *J. Power Sources*, vol.

275, pp. 573–587, 2015.

- [65] C. Guenther, B. Schott, W. Hennings, P. Waldowski, and M. A. Danzer, “Model-based investigation of electric vehicle battery aging by means of vehicle-to-grid scenario simulations,” *J. Power Sources*, vol. 239, pp. 604–610, 2013.
- [66] S. Wang, L. Shang, Z. Li, H. Deng, and J. Li, “Online dynamic equalization adjustment of high-power lithium-ion battery packs based on the state of balance estimation,” *Appl. Energy*, vol. 166, pp. 44–58, 2016.
- [67] S. Paul, C. Diegelmann, H. Kabza, and W. Tillmetz, “Analysis of ageing inhomogeneities in lithium-ion battery systems,” *J. Power Sources*, vol. 239, pp. 642–650, 2013.
- [68] X. Gong, R. Xiong, and C. C. Mi, “Study of the Characteristics of Battery Packs in Electric Vehicles with Parallel-Connected Lithium-Ion Battery Cells,” *IEEE Trans. Ind. Appl.*, vol. 51, no. 2, pp. 1872–1879, 2015.
- [69] T. Bruen and J. Marco, “Modelling and experimental evaluation of parallel connected lithium ion cells for an electric vehicle battery system,” *J. Power Sources*, vol. 310, pp. 91–101, 2016.
- [70] R. Gogoana, M. B. Pinson, M. Z. Bazant, and S. E. Sarma, “Internal resistance matching for parallel-connected lithium-ion cells and impacts on battery pack cycle life,” *J. Power Sources*, vol. 252, pp. 8–13, 2014.
- [71] M. Dubarry, N. Vuillaume, and B. Y. Liaw, “From single cell model to battery pack simulation for Li-ion batteries,” *J. Power Sources*, vol. 186, no. 2, pp. 500–507, 2009.
- [72] N. Yang, X. Zhang, B. Shang, and G. Li, “Unbalanced discharging and aging due to temperature differences among the cells in a lithium-ion battery pack with parallel combination,” *J. Power Sources*, vol. 306, pp. 733–741, 2016.
- [73] F. Lebel, S. Wilke, B. Schweitzer, M. Roux, and J. P. F. Trov, “A Lithium-Ion Battery Electro-Thermal Model of Parallellized Cells,” pp. 3–8, 2016.
- [74] C. Weng, Y. Cui, J. Sun, and H. Peng, “On-board state of health monitoring of lithium-ion batteries using incremental capacity analysis with support vector regression,” *J. Power Sources*, vol. 235, pp. 36–44, 2013.
- [75] C. Weng, X. Feng, J. Sun, and H. Peng, “State-of-health monitoring of lithium-ion battery modules and packs via incremental capacity peak tracking,” *Appl. Energy*, vol. 180, pp. 360–368, 2016.
- [76] T. Kalogiannis, D. I. Stroe, J. Nyborg, K. Nørregaard, A. E. Christensen, and E.

- Schaltz, "Incremental Capacity Analysis of a Lithium-Ion Battery Pack for Different Charging Rates," *ECS Trans.*, vol. 77, no. 11, pp. 403–412, 2017.
- [77] Y. Zheng, M. Ouyang, L. Lu, and J. Li, "Understanding aging mechanisms in lithium-ion battery packs: From cell capacity loss to pack capacity evolution," *J. Power Sources*, vol. 278, pp. 287–295, 2015.
  - [78] M. Ouyang, X. Feng, X. Han, L. Lu, Z. Li, and X. He, "A dynamic capacity degradation model and its applications considering varying load for a large format Li-ion battery," *Appl. Energy*, vol. 165, pp. 48–59, 2016.
  - [79] C.-Y. Chang, P. Tulpule, G. Rizzoni, W. Zhang, and X. Du, "A probabilistic approach for prognosis of battery pack degradation," *J. Power Sources*, vol. 347, pp. 57–68, 2017.
  - [80] B. Scrosati, J. Garche, and W. Tillmetz, *Advances in Battery Technologies for Electric Vehicles*. 2015.
  - [81] A. Cordoba-Arenas, S. Onori, G. Rizzoni, and G. Fan, "Aging propagation in advanced battery systems: Preliminary results," in *IFAC Proceedings Volumes (IFAC-PapersOnline)*, 2013, vol. 7, no. PART 1, pp. 313–318.
  - [82] M. Berecibar, I. Gandiaga, I. Villarreal, N. Omar, J. Van Mierlo, and P. Van Den Bossche, "Critical review of state of health estimation methods of Li-ion batteries for real applications," *Renew. Sustain. Energy Rev.*, vol. 56, pp. 572–587, 2016.
  - [83] C. Zhang, J. Liu, S. M. Sharkh, and C. Zhang, "Identification of dynamic model parameters for lithium-ion batteries used in hybrid electric vehicles," *Int. Symp. Electr. Veh.*, vol. 1, pp. 1–11, 2009.
  - [84] J. D. Kozlowski, "Electrochemical cell prognostics using online impedance measurements and model-based data fusion techniques," *IEEE Aerosp. Conf. Proc.*, vol. 7, pp. 3257–3270, 2003.
  - [85] K. S. Ng, C. S. Moo, Y. P. Chen, and Y. C. Hsieh, "Enhanced coulomb counting method for estimating state-of-charge and state-of-health of lithium-ion batteries," *Appl. Energy*, vol. 86, no. 9, pp. 1506–1511, 2009.
  - [86] I. J. Fernández, C. F. Calvillo, A. Sánchez-Miralles, and J. Boal, "Capacity fade and aging models for electric batteries and optimal charging strategy for electric vehicles," *Energy*, vol. 60, pp. 35–43, 2013.
  - [87] J. Remmlinger, M. Buchholz, M. Meiler, P. Bernreuter, and K. Dietmayer, "State-of-health monitoring of lithium-ion batteries in electric vehicles by on-board internal resistance estimation," *J. Power Sources*, vol. 196, no. 12, pp. 5357–5363, 2011.



- [88] S. Ebbesen, P. Elbert, and L. Guzzella, "Battery State-of-Health Perceptive Energy Management for Hybrid Electric Vehicles," *IEEE Trans. Veh. Technol.*, vol. 61, no. 7, pp. 2893–2900, 2012.
- [89] V. Marano, S. Onori, Y. Guezennec, G. Rizzoni, and N. Madella, "Lithium-ion batteries life estimation for plug-in hybrid electric vehicles," *Veh. Power Propuls. Conf. 2009. VPPC '09. IEEE*, pp. 536–543, 2009.
- [90] F. Camci, C. Ozkurt, O. Toker, and V. Atamuradov, "Sampling based State of Health estimation methodology for Li-ion batteries," *J. Power Sources*, vol. 278, pp. 668–674, 2015.
- [91] G. L. Plett, "Extended Kalman filtering for battery management systems of LiPB-based HEV battery packs: Part 1. Background," *J. Power Sources*, vol. 134, no. 2, pp. 252–261, 2004.
- [92] I. S. Kim, "A technique for estimating the state of health of lithium batteries through a dual-sliding-mode observer," *IEEE Trans. Power Electron.*, vol. 25, no. 4, pp. 1013–1022, 2010.
- [93] H. G. Schweiger *et al.*, "Comparison of several methods for determining the internal resistance of lithium ion cells," *Sensors*, vol. 10, no. 6, pp. 5604–5625, 2010.
- [94] J. Zhang and J. Lee, "A review on prognostics and health monitoring of Li-ion battery," *J. Power Sources*, vol. 196, no. 15, pp. 6007–6014, 2011.
- [95] G. K. Prasad and C. D. Rahn, "Model based identification of aging parameters in lithium ion batteries," *J. Power Sources*, vol. 232, pp. 79–85, 2013.
- [96] M. Gholizadeh and F. R. Salmasi, "Estimation of state of charge, unknown nonlinearities, and state of health of a lithium-ion battery based on a comprehensive unobservable model," *IEEE Trans. Ind. Electron.*, vol. 61, no. 3, pp. 1335–1344, 2014.
- [97] J. Remmlinger, M. Buchholz, T. Soczka-Guth, and K. Dietmayer, "On-board state-of-health monitoring of lithium-ion batteries using linear parameter-varying models," *J. Power Sources*, vol. 239, pp. 689–695, 2013.
- [98] C. R. Gould, C. M. Bingham, D. A. Stone, and P. Bentley, "New battery model and state-of-health determination through subspace parameter estimation and state-observer techniques," *IEEE Trans. Veh. Technol.*, vol. 58, no. 8, pp. 3905–3916, 2009.

## Chapter 2

# Comparison of Li-ion Battery Equivalent Circuit Modeling Using Impedance Analyzer and Bayesian Networks

### **Abstract**

Energy storage system simulations require a battery model capable of precisely predicting the dynamic behavior and characteristics of the battery. There are multiple methods available in the contemporary literature on accurate battery modeling. The most common method utilized is the semi-empirical equivalent circuit model (ECM) developed through time-domain testing. A better alternative can be obtained using a combination of time-domain and frequency-domain tests to parameterize ECM components. The underlying fitting mechanism for this proposed method is linear least square regression. The fitting accuracy can be further improved by applying Bayesian Network (BN) to estimate the ECM circuit elements. In this chapter, two systematic approaches to determine ECM are discussed. First, the ECM is developed through fitting the time-domain and frequency-domain test results carried out on a commercial electric bicycle Li-ion battery composed of Samsung ICR18650-22P cells. Later BN method was applied to estimate the

ECM circuit elements. In both cases, multiple circuit topologies were used to compare the accuracy of the model. The models were developed in MATLAB/ Simulink environment. A highly dynamic drive cycle was utilized to validate the ECMs through hardware-in-loop testing. It was observed that the appropriate ECM topology used for the linear least square regression fitting generated an average error of 3.3% whereas for BN estimation it was 3.5%.

## 2.1 Introduction

Lithium-ion technologies require advanced battery management systems (BMS) to operate safely at maximum performance. These BMS heavily rely on an accurate model of the battery [1]. The battery model is also required in the battery simulation of performance and aging studies [2]. Battery modeling techniques can be grouped into three broad categories: electrochemical, physics-based and ECM. ECM provides a circuit composed of a voltage source, signifying open-circuit voltage (OCV) and the battery internal impedance. This internal impedance can be determined to utilize time and frequency domain testing [3], [4]. The accuracy of ECM typically depends on the number of RC parallel combinations [5].

Authors in [6], [7] generated an ECM through frequency domain electrochemical impedance spectroscopy (EIS) tests. They limited their experimentation to a single cell and results were fitted with 2 or 3 RC networks. However, the accuracy of such an ECM model is reduced due to a reduction in the number of RC components. Moreover, single cell-based ECM is incapable of considering the variability of multiple cells/modules in a battery pack.

Time-domain hybrid pulse power characterization (HPPC) is used by authors in [8]–[14] to generate an ECM. Impedance parameters are determined from the voltage response during the relaxation period after a constant discharge period. However, the impedance determined through HPPC is only valid for constant current loads at a specific state of charge (SOC) and temperature. Moreover, the ECM from HPPC is also limited to 1-3 RC components.

Authors in [15]–[17] applied multiple versions of Kalman filters to estimate components of ECM. The complexity and processing time to determine the impedances of ECM increases with the higher number of RC components. Thus, the authors reduce the fitting to the 1RC component. But this reduces the accuracy of ECM severely.

Authors in [18], [19] used various filters to estimate 3RC based ECM. Developed ECM showed improved results compared to single RC based models. An ECM requires even higher RC components to model a battery accurately. In [20] both time-domain and frequency-domain analyses are performed on multiple Li-ion battery technologies to develop an ECM with higher accuracy containing 8RC components. But there was no logical explanation of why an 8RC ECM is appropriate for ECM. Also, the advantage gained through using a higher order ECM was not tangible, as a comparison with lower order models was not presented. Moreover, the determined impedance parameters are non-uniform and complicated to replicate.

Another statistical approach that is widely used to estimate the unseen variables conditional to the measurements is Bayesian Networks (BN) [21], [22]. In the battery

studies, BNs are mostly used for state estimation purposes such as SOC and state of health (SOH) of the battery which are unseen variables and difficult to measure [23], [24]. However, BN can be used for probabilistic estimation of any problem with limited measurements and observations. Therefore, it can be used to estimate the battery impedance elements conditional to the measurements of the time and frequency domain tests.

This chapter develops the ECM of a Li-ion battery pack by fitting experimental results and estimation through BN. The developed models are compared based on their accuracy by quantifying the error variation when considering higher and lower order ECM models. A commercial Li-ion battery is used as a test case in this regard. Time-domain capacity and hybrid pulse power characterization test, and frequency domain electrochemical impedance spectroscopy test results are used to develop the models. The first set of ECM was developed with fitting the experimental result with a linear least square regression by Impedance Analyzer to generate 2RC, 3RC and 8RC models. Whereas, the second set of models were developed for 2RC and 3RC with BN estimation.

The rest of the chapter is organized as follows. Section 2.2 provides an overview of the experimental procedure describing the boundary conditions and various scenarios utilized to generate a detailed ECM model. Section 2.3 delves into the details and technicalities of the experimental procedures. Section 2.4 shows how the ECM model was developed using the impedance analyzer through the linear least square regression method. Sections 2.5 explains the process of developing the BN for the regression procedure and showcases the results obtained. Finally, Section 2.6 illustrates the comparison between the

impedance analyzer's linear least square method and BN estimation followed by the conclusion.

## 2.2 Overview of Experimental Method

The commercial Li-ion battery pack can either be charged from an outlet or through regenerative braking. The battery pack is composed of Samsung ICR18650-22P. The details of the battery pack and associated cells are provided in Table 2.1 [25].

Table 2.1. Battery pack and cell details

Battery or Cell Properties	Value
Nominal Voltage	48 Volts
Nominal Capacity	8.6 Amp-hours
Pack Arrangement	13S4P (13 modules of 4 cells connected parallelly in a single module)
Maximum Charging Voltage	54.6 Volts
Minimum Cutoff Voltage	35.75 Volts
Cell Chemistry	Lithium cobalt oxide ( $LiCoO_2$ )
Cell Nominal Voltage	3.62 Volts
Cell Nominal Capacity	2.15 Amp-hours
Cell Minimum Cutoff Voltage	2.75 Volts
Standard Discharge Current	430 mA (0.2C)
Maximum Discharge Current	10,000 mA (10C)
Cell Maximum Charge Voltage	4.20 Volts
Standard Charge Current	1075 mA (C/2)
Maximum Charge Current	2150 mA (1C)

The battery pack used for the testing procedure was at the beginning of life (BOL). The time-domain testing consists of capacity and hybrid pulse power characterization (HPPC) tests. A National Instrument data acquisition (DAQ) device was used to record pack voltage and current. The temperature was measured from 8 different locations within the pack. Multiple analog temperature sensors were used to observe the variations within the pack. The temperature measurements were also performed with the DAQ device. The

locations of the eight sensors are marked in Figure 2.1. Also, three module voltages from module 1, 6, and 13 were recorded during time-domain tests. These tests were repeated for  $-10^{\circ}\text{C}$ ,  $0^{\circ}\text{C}$ , and  $20^{\circ}\text{C}$  to have a proper representation of commercial Li-ion usage conditions.

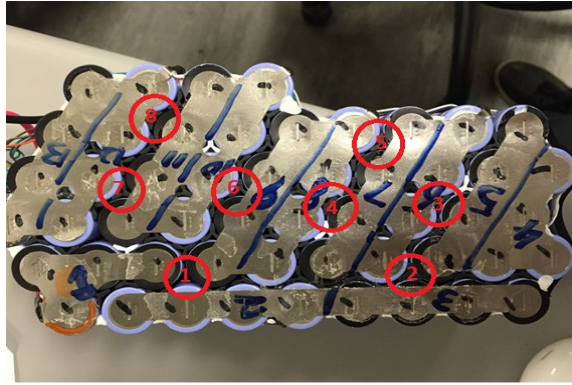


Figure 2.1. The disassembled commercial Li-ion battery pack.

The frequency-domain testing method, EIS was performed through a galvanostatic control using a battery impedance analyzer. The EIS test was performed with a frequency sweep from 2mHz to 1kHz at 100%, 80%, 60%, 40% and 20% SOC. Each of these tests was repeated for  $-10^{\circ}\text{C}$ ,  $0^{\circ}\text{C}$ , and  $20^{\circ}\text{C}$ , in accordance with the time-domain experiments. The EIS was performed at multiple SOC to generate more data for developing a proper battery impedance model. Note that, although the experiments are performed on the commercial Li-ion battery and the model results and validations are based on the dynamic load profile data, the developed models are not dependent on any specific application of commercial Li-ion battery.

## 2.3 Testing Procedure

The type of tests performed on the commercial Li-ion battery can be classified in three main groups: Capacity test to measure the actual capacity of the battery in Ah, HPPC test to measure the OCV vs. SOC characteristics of the battery, and EIS with an impedance analyzer to determine the internal impedance of the battery. The capacity and HPPC tests are time-domain whereas the EIS is frequency-domain. Thus, the capacity and HPPC test share a similar set of equipment as opposed to the EIS. The following subsections delve into detail about the testing procedures.

### 2.3.1 Capacity Test

The test determines the actual capacity of the battery in Ah while being discharged with a constant current. The nominal capacity of the battery ( $Q_n$ ), provided by the manufacturer is an average measurement. The average is determined by testing multiple batteries from the production line. Due to minor changes in the manufacturing process, each battery cell has a slightly different capacity than the other. The difference in individual cells is often negligible. However, when a battery pack is formed with cells with various actual capacity, the overall battery capacity can have a major deviation from the manufacturer rated nominal capacity. Moreover, the capacity measurement estimates the SOC of the battery. A wrong SOC estimation can lead to cycling the battery incorrectly, causing performance issues and pre-mature aging. Furthermore, the battery capacity changes significantly with the ambient temperature even if determined with manufacturer suggested C-rates are used. Thus, it is essential to know the actual capacity of the battery at multiple temperatures to develop accurate ECM.



The capacity of the battery is dependent upon the discharge current C-rate and temperature. A standardized C/3 rate is used in accordance with the manufacturer specifications [25]. For the battery in the discussion, a constant current load of 2.87A was used to determine actual battery capacity ( $Q_a$ ).

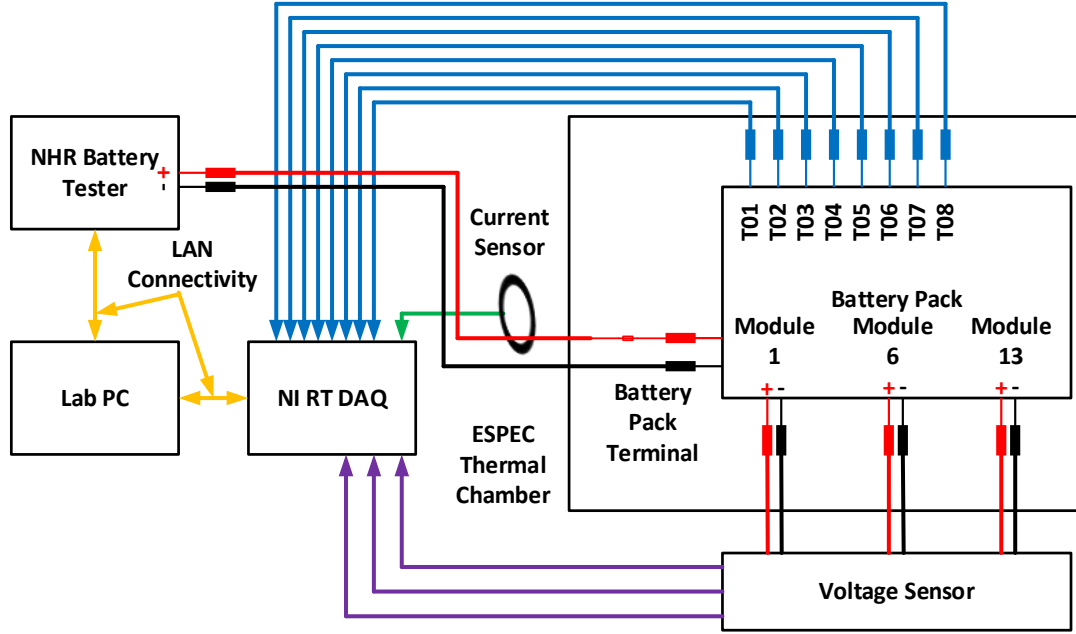


Figure 2.2. Time-domain test experimental setup.

The battery was kept inside the ESPEC EPZ-4H thermal chamber. The NHR 9200 battery tester equipped with 4912 part was used to charge or discharge the battery. Hall effect current and voltage sensors measured analog signals and provided the data to the NI PXIe-1071 chassis equipped with NI PXIe-8135 processor and NI PXI-6254 data acquisition system. The thermal sensor temperature data was also sent through the remaining channels of the data acquisition system. The battery tester, data acquisition system, and the thermal chamber were in a single LAN network with the lab PC controlling the experiment. The lab PC was utilizing NI LabView 2014 to control the connected

equipment in real-time. Figure 2.2 depicts the experimental setup used to perform the test. The results of the capacity test are given in Table 2.2.

Table 2.2. The measured actual capacity of commercial Li-ion battery

Temperature (°C)	Battery Actual Capacity $Q_a$ (Ah)
20	8.359
0	8.145
-10	7.671

It was observed that battery capacity dropped as the temperature was reduced. The reduction in temperature reduces the rate of transfer of li-ion from one electrode to another. The electrolyte forms crystals, increasing the impedance and impeding the transferring of li-ions. The DOD of the battery is calculated according to (2-1) where the SOC measurement is based on actual capacity  $Q_a$ .

$$DOD(t) = 100 - SOC(t) = 100 - \left( \frac{Q_a(t)}{Q_n} \times 100 \right) \quad \forall t \quad (2-1)$$

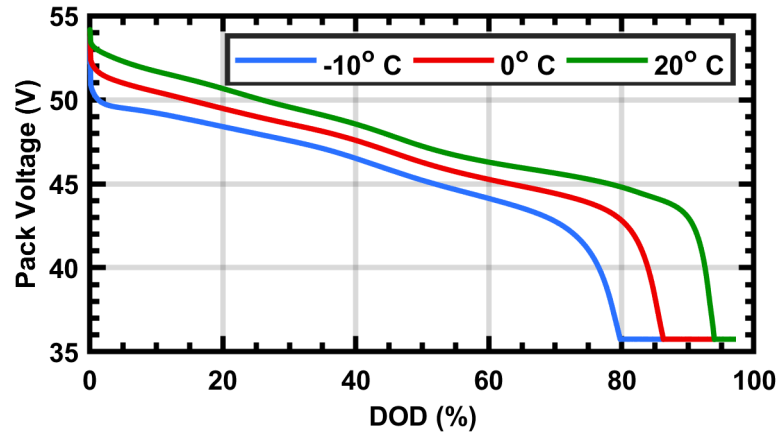


Figure 2.3. Capacity test results

The result of the capacity test can be observed in Figure 2.3 where the pack voltage is plotted against DOD. It is evident from Figure 2.3 that reduction in overall capacity

reduces the maximum DOD. Furthermore, due to the increase in internal impedance, the pack terminal voltage is reduced.

### 2.3.2 Hybrid Pulse Power Characterization Test

The hybrid pulse power characterization (HPPC) test is designed to observe the pulsed response of the battery. The test applies a charge and discharge pulse on a fully charged and relaxed battery. This is followed by a constant current discharge and a relaxation period. The duration of the relaxation is suggested by the manufacturer. For this commercial Li-ion battery, the purpose of conducting HPPC tests was to develop the OCV-DOD relationship. The measurement of battery terminal voltage, and depleted Ah ( $Q$ ) at the end of each relaxation period is recorded. At no-load condition, the battery terminal voltage gives OCV. Ah measurement ( $Q$ ) is used to generate the DOD of the battery from (2-2). Data from the experiment is fitted to an appropriate function using any adept curve fitting tool.

$$DOD(t) = 100 - SOC(t) = 100 - \left( \frac{Q(t)}{Q_n} \times 100 \right) \quad \forall t \quad (2-2)$$

HPPC test is utilized by the contemporary authors to generate the ECM circuit parameters. However, ECM parameters generated solely through HPPC inherently lacks accuracy as the voltage response is highly dependent on the constant load current between each set of pulses.

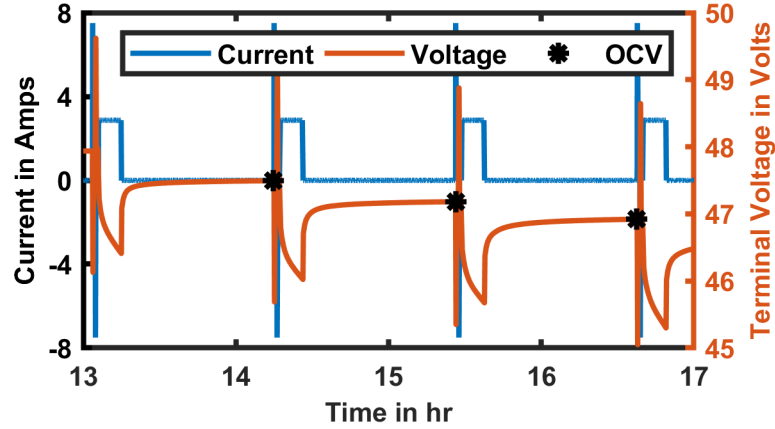


Figure 2.4. The HPPC test load profile and response voltage.

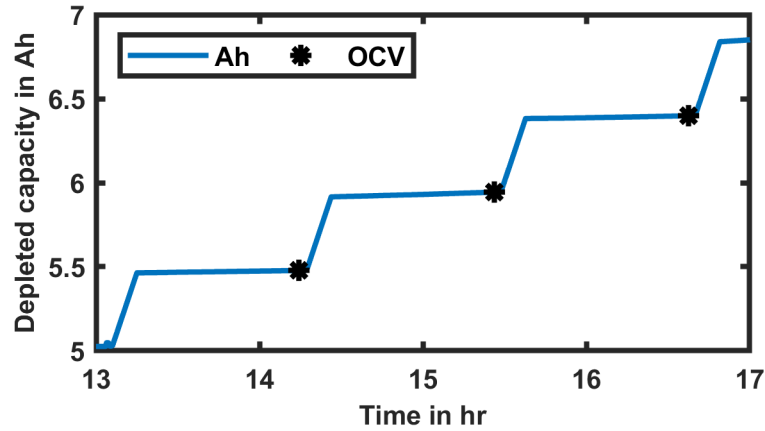


Figure 2.5. The HPPC test Ah response.

The experimental setup for HPPC remains the same as the capacity test. Instead of constant load current, a custom waveform representing the HPPC characteristics was used. Each constant discharge period was designed to deplete 5% of SOC. Since the nominal battery capacity is 8.6Ah, the constant discharge needed to deplete 0.43Ah. The constant discharge current was selected to be 2.87A ( $C/3$ ) for 9 minutes followed by 60 minutes of relaxation. In the discharge of 9 minutes, 5% of SOC was depleted. The 60 minutes relaxation was selected according to the manufacturer's suggestion [25]. The sample of the HPPC test result can be seen in Figure 2.4. Figure 2.4 shows the load current representing

the HPPC and response voltage. It also shows where the OCV measurements were collected. It is noticeable that after each constant discharge the battery terminal voltage settles to a lower value corresponding to the lower SOC state.

Table 2.3. OCV-DOD data from HPPC test

20°C		Temperature 0°C		-10°C	
DOD (%)	OCV (V)	DOD (%)	OCV (V)	DOD (%)	OCV (V)
0.0000	54.9950	0.0000	53.6810	0.0233	54.1070
5.3023	53.9280	5.2209	52.9760	5.0930	53.2010
10.9419	53.1930	10.8256	52.5700	10.5930	52.6970
16.1860	52.7320	16.1395	52.1010	16.1047	52.2970
21.6047	52.3310	21.7791	51.4810	21.5465	51.7130
26.8256	51.7450	27.1163	50.9670	26.7442	51.0630
32.1628	51.1760	32.6744	50.5130	32.0698	50.5010
37.3256	50.7270	38.0233	49.8570	37.1977	49.9570
42.7209	50.2230	43.5000	48.9730	42.5814	49.3300
47.8837	49.4000	48.6977	48.1960	47.6977	48.5980
53.3256	48.5610	54.2093	47.6430	52.9651	47.9340
58.4419	47.9370	59.3605	47.2610	58.1163	47.4320
63.6977	47.4940	64.9651	46.9750	63.3023	47.0600
69.1163	47.1810	70.0814	46.7160	68.6860	46.7410
74.4070	46.9200	75.3488	46.3830	73.9419	46.4020
80.3488	46.5920	80.8023	45.7440	79.3953	45.9390
85.6279	45.9840	86.0814	45.1140		

Figure 2.5 depicts the corresponding Ah depletion along with the OCV data point. The plateau reached after every successive constant discharge in Figure 2.5 signifies that the battery was relaxed without any load, thus allowing to reach the OCV conditions. The tabulated results of the entire HPPC test are given in Table 2.3.

### 2.3.3 Electrochemical Impedance Spectroscopy Test

The electrochemical impedance spectroscopy (EIS) test is a powerful tool used in electrochemistry to extract data on electrode kinetics and diffusion from an electrochemical

process. One of the major application areas for EIS is electrochemical energy storage or batteries. The typical DC analysis on battery only reveals information on electrode kinetics or mass transport. On the other hand, EIS can obtain both types of data by analyzing the battery with AC signals. In the galvanostatic EIS, the battery is subjected to a sweep of sinusoidal current ( $I$ ) while voltage response ( $E$ ) is recorded. The impedance is measured from (2-3) and can be explained as complex numbers as (2-4) and (2-5).

$$Z_t = \frac{E_t}{I_t} = \frac{E_o \sin(\omega t + \varphi)}{I_o \sin(\omega t)} \quad \forall t \quad (2-3)$$

$$Z_o = \frac{E_o}{I_o} \quad (2-4)$$

$$Z_t = Z_o \frac{\sin(\omega t + \varphi)}{\sin(\omega t)} = Z_o(\cos \varphi - j \sin \varphi) \quad \forall t \quad (2-5)$$

The complex impedance measured from the EIS experiment is most commonly analyzed with the Nyquist plot. An ideal Nyquist plot for a  $LiCoO_2$  technology is depicted in Figure 2.6 is divided into 5 sections according to [2]. Each section of this Nyquist plot is attributed to a specific electrochemical kinetic property occurring within the battery. These electrochemical kinetic properties are adequate in characterizing this li-ion battery. The EIS reveals these properties accurately. In Figure 2.6, Section 1 is attributed to the conductive materials i.e. current collectors, interconnections between cells and wires. At higher frequency, these components show inductive properties, thus the inductive component is considered in the ECM. The x-axis intercept in section 2 represents the cumulative resistive effect of current collectors, the interconnection between cells,

electrolyte, active material, and separator, characterized by a resistance. The first semi-circle, section 3, is related to the solid-electrolyte interface (SEI), portrayed by a parallel resistance and constant phase element (CPE). The second semi-circle (section 4) occurs due to double-layer capacitance and charge transfer resistance at the electrode. Though section 4 is attributed to different properties, due to the semi-circular shape, the ECM element is identical to section 3. Finally, section 5, expressed by a 45° line, is due to diffusion of lithium ions in the active material of the electrode at very low frequency, represented by a Warburg element.

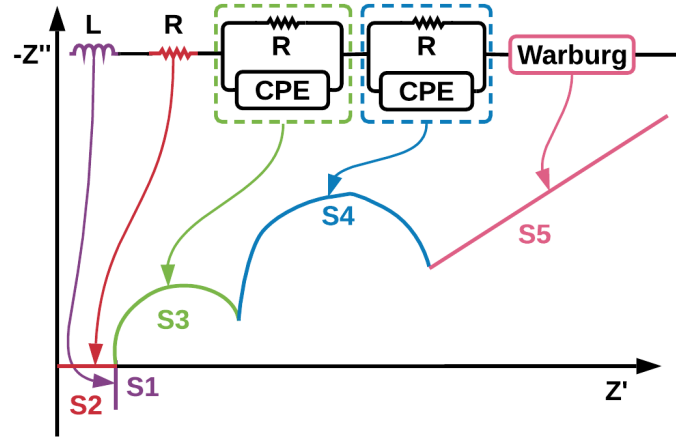


Figure 2.6. The ideal Nyquist plot for  $LiCoO_2$  Li-ion battery.

Temperature and SOC are major proponents that affect the underlying properties that dictate the ECM components. Thus, EIS must be repeated multiple times for separate temperature and SOC to account for these variations. Results from such tests need to accumulate to provide a complete characteristic.

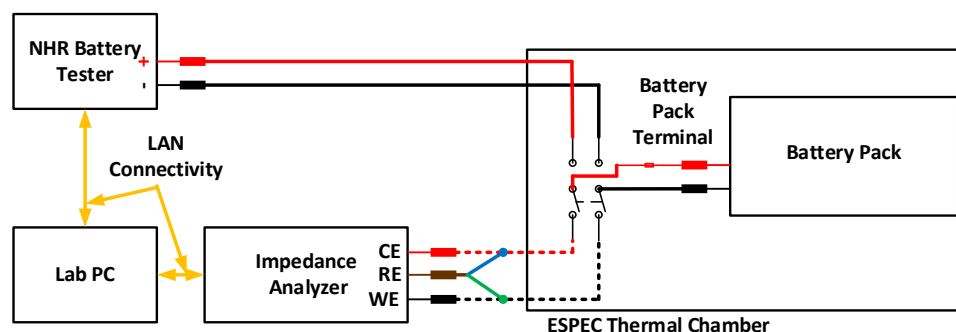


Figure 2.7. Time-domain test experimental setup.

For the commercial Li-ion battery, the experimental setup for EIS can be explained in Figure 2.7. The battery was fully charged up to the manufacturer's recommended voltage and kept in the thermal chamber at 20°C. The EIS experiment was solely operated by the impedance analyzer Modulab from Solartron Analytical fitted with Pstat 1MS/s and accessory HV 100. The Pstat was aided by the HV 100 to accommodate the entire battery pack. The current electrode (CE) and the working electrode (WE) connected to the battery terminals provided the sinusoidal current signal. The current signal was of 100mA, ranged from 2mHz to 1kHz. The reference electrode (RE) measured the sinusoidal voltage response. After the experiment was carried out for a specific SOC, the battery terminal was switched to battery tester. The battery tester was programmed to discharge the battery 20% to reach the next experimental state. A constant 2.87A (C/3) rate was applied to discharge the battery. There was a rest period after the discharge to allow the battery to reach the steady-state condition. The experiment was repeated until the battery reached 20% SOC. After that, the battery was recharged and put on a different temperature to repeat the entire procedure. These tests were repeated for 0°C and -10°C. The results obtained from the EIS test can be seen in Figure 2.8, Figure 2.9, and Figure 2.10. Each of the following figures shows the measured impedance at different SOC at a specific temperature.



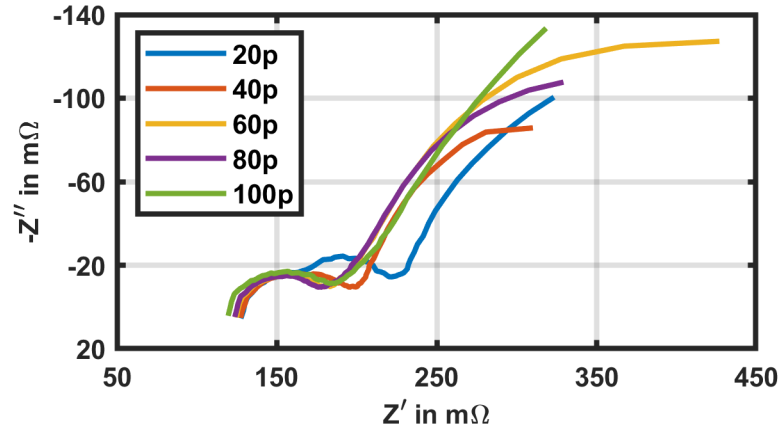


Figure 2.8. The measured impedance by EIS test at 20°C.

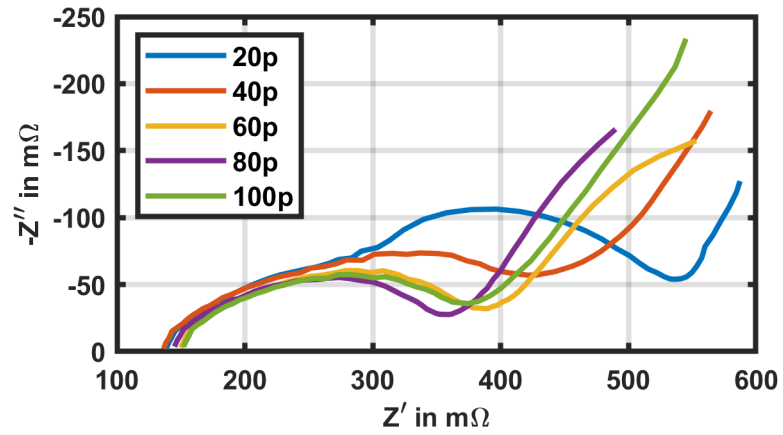


Figure 2.9. The measured impedance by EIS test at 0°C.

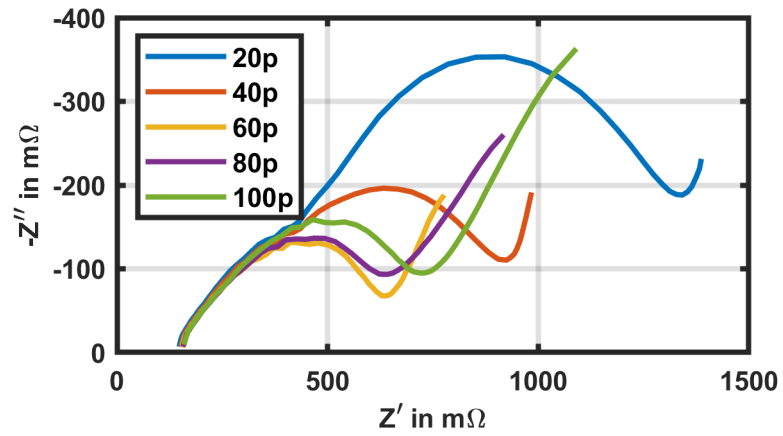


Figure 2.10. The measured impedance by EIS test at -10°C.

It is evident from these results that both real and imaginary parts of the internal impedance of the battery increases as temperature drops. The impedance increases rapidly after the temperature drops below 0°C. The EIS results correspond with the fact that impedance increases with the crystallization of the electrolytes occurring below 0°C. Comparing the effect of temperature, inductive properties of the battery impedance in high frequencies (Section 1 in Figure 2.6) are mostly observed in higher temperatures. However, the resistive properties of the battery pack increase with the temperature decrease, i.e. the battery shows higher resistances in low temperatures. This increase in the resistance is not only observed in the cumulative resistance of the connections, but it is also noticed in the semi-circles' resistances, as the radius of the semi-circles increases with the temperature drop. In addition, at higher temperatures, the effect of Li-ion diffusion in the electrode is dominant on the battery impedance (Section 5 in Figure 2.6), while in lower temperatures, the impact of the SEI and double-layer capacitance and charge transfer resistance are more influential, as depicted on Section 3 and 4 in Figure 2.6. Different SOC's results show that two semi-circles are separate and distinguishable in lower SOC's. However, in higher SOC's, only one semi-circle is noticeable in the Nyquist plot. Therefore, the effects of SEI, double-layer capacitance, and charge transfer resistance are detectable in lower SOC's.

## **2.4 Equivalent Circuit Modeling**

The ECM developed in this chapter utilizes three inputs, initial SOC, load current, and ambient temperature. The Model produces battery terminal voltage, present SOC, and DOD. The ECM has four parts, SOC and DOD determination, OCV calculation, equivalent impedance component, and terminal voltage deduction. At first the initial SOC and load

current at time  $t$  is taken to determine the SOC and DOD at time  $t + 1$ . The SOC and DOD values at time  $t + 1$  and temperature are used to determine the equivalent circuit component values. Simultaneously, the SOC and DOD at time  $t + 1$  and temperature are utilized to calculate the OCV of the battery. Finally, the present OCV and equivalent circuit component values are used in the differential equation to produce the terminal voltage of the battery. Though the system can produce more results, it is limited to terminal voltage, present SOC and DOD to ensure a high level of integrity with external components such as residential or vehicular models. The process is visualized in Figure 2.11. The number of equivalent circuit components produced depends on the degree of accuracy of the ECM. Figure 2.12 shows the ECM developed in this chapter.

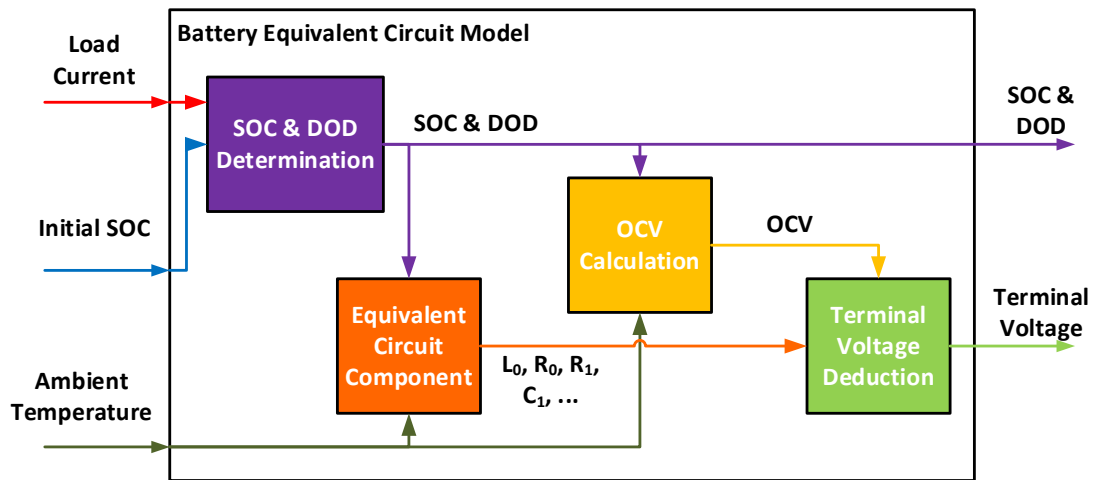


Figure 2.11. Equivalent circuit components

There are various ways of determining the SOC and DOD of the battery. For this chapter, a coulomb counting method was used. For the equivalent circuit components, as shown in Figure 2.6, at higher frequencies, the inductive property of the is dominant due to the electrically conductive parts in the pack. A lump resistance and inductance represent these cumulative resistive and inductive properties. Experimental results revealed that the

resistive part has a negative temperature coefficient. The value of this resistance increases as temperature drops, unlike a regular resistance.

A parallel combination of a resistance and constant phase element (CPE) is known as Zarc, which models the semi-circles in Figure 2.6. To model this impedance with electrical circuit elements, the author in [26] developed a method to approximate them with odd numbers of parallel resistance-capacitance (RC) combinations. It was proven that any arc in the Nyquist plot that requires a Zarc element in the circuit can be replaced with 3 consecutive RC elements with considerable accuracy. Thus, this study uses 6 consecutive RC elements for two semi-circle/arcs instead of a Zarc for the most precise model. A Warburg element is a resistive component which corresponds to a linearly rising line at  $45^\circ$  in the Nyquist plot and can be represented by 2 RC circuits in series.

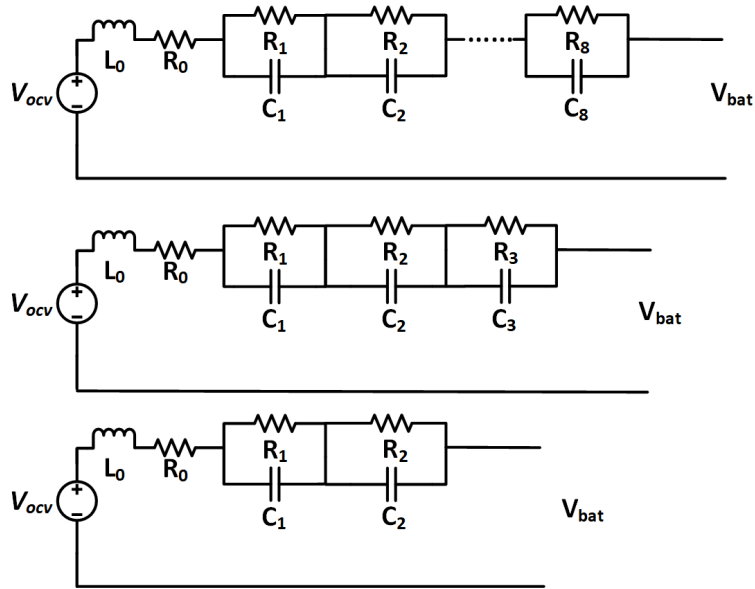


Figure 2.12. Generated equivalent circuit models

The most accurate ECM without any significant reduction in processing/calculation time model would have 8RC components, 6RC for the first two Zarcs and 2RC for the

Warburg element. A simplified model could be designed considering that the Nyquist plots have three arcs. In this case, a simplified model would have 3RC components, one for each arc. Both circuits, with 8RC and 3RC, were modeled using the experimental data for commercial Li-ion battery. Moreover, a further simplified and popular battery model with 2RC used by researchers in [8, 20], was also modeled based on the experimental results to compare.

Two statistical approaches are used to estimate the OCV and R, L and RC components from the HPPC and EIS experimental data: Impedance Analyzer fitting and Bayesian model. The significance of both Impedance Analyzer fitting and BN model is the capability to produce robust battery models, capable of predicting battery's characteristics with accuracy and precision. These two methods have a different approach to the modeling process. The ECM parameter fitting with Impedance Analyzer is based upon deterministic least-square regression, while the BN considers a probabilistic approach.

The application of ECM based on an impedance analyzer is typical for laboratory environments where a higher order model is desired as it can provide accurate battery characteristics with utmost efficiency. On the other hand, BNs can be applied for both laboratory and online applications as it can provide a more accurate lower order model. Lower order models can greatly simplify implementation for online applications.

#### **2.4.1 Impedance Analyzer Fitting**

The OCV was determined by the function of  $OCV = f(DOD, T)$  developed from the HPPC test results. A fifth-order polynomial equation was developed to fit the recorded data

from Table 2.3. A linear least square method was used to fit the data to the polynomial equation. The values of the coefficients are given in Table 2.4. MATLAB 2016 curve fitting tool was used to generate the function. The values of the parameters are given in Table 2.4.

Table 2.4. OCV-DOD-T function parameters

Parameters	Temperature		
	20°C	0°C	-10°C
p1	-1.89E-8	-8.07E-8	-8.24E-8
p2	2.42E-6	2.08E-5	2.07E-5
p3	-2.84E-6	2.08E-3	2.06E-3
p4	-8.52E-3	1.01E-1	1.02E-1
p5	0.1242	-2.445	-2.649
p6	54.52	75	80

The EIS tests and subsequent fittings were performed with Modulab ECS software associated with a Solartron impedance analyzer. Modulab ECS employs a linear least square linear regression method based on provided initial values to fit the experimentally obtained data to ECM. The initial values of the ECM components are obtained from the respective EIS Nyquist plot sections that the component belongs to as previously defined in Figure 2.6. For example, the initial value of the inductor  $L_0$  was found from the last data point with the maximum frequency  $f_{L_0}$  and impedance  $Z''_{L_0}$  using (2-7). Similarly, the x-axis intercept of the Nyquist plot provides the initial value of  $R_0$ . For the capacitors, the impedance and frequencies were selected from the respective arc that the circuit component is representing. The capacitor initial values were calculated similarly by (2-8).

$$L_0 = \frac{Z''_{L_0}}{2\pi f_{L_0}} \quad (2-6)$$

$$C_x = -\frac{1}{2\pi f Z''_{C_x}} \quad (2-7)$$

The determined circuit components are at multiple SOC and temperature. These components were fitted to a fourth-order polynomial to obtain  $Component_x = f(SOC, T)$ . The function parameter obtained is given in Table 2.5.

Table 2.5. ECM component function parameters

Components	Parameters				
	p1	p2	p3	p4	p5
L <sub>0</sub>	-6.38E-14	1.59E-11	-1.38E-09	4.85E-08	1.38E-06
R <sub>0</sub>	-1.98E-09	4.52E-07	-3.61E-05	1.01E-03	1.16E-01
R <sub>1</sub>	1.92E-09	-4.61E-07	3.91E-05	-1.36E-03	3.20E-02
C <sub>1</sub>	1.18E-09	-3.44E-07	3.39E-05	-1.34E-03	4.28E-02
R <sub>2</sub>	-2.17E-09	5.37E-07	-4.47E-05	1.41E-03	6.40E-03
C <sub>2</sub>	3.36E-08	-8.57E-06	7.62E-04	-2.72E-02	4.66E-01
R <sub>3</sub>	2.73E-09	-6.33E-07	5.35E-05	-2.01E-03	4.65E-02
C <sub>3</sub>	2.49E-08	-9.58E-06	1.23E-03	-6.45E-02	2.12E+00
R <sub>4</sub>	1.92E-09	-5.89E-07	6.81E-05	-3.49E-03	7.63E-02
C <sub>4</sub>	5.21E-06	-1.36E-03	1.21E-01	-3.97E+00	4.50E+01
R <sub>5</sub>	5.66E-09	-1.38E-06	1.18E-04	-4.01E-03	5.54E-02
C <sub>5</sub>	1.41E-05	-4.03E-03	3.99E-01	-1.57E+01	2.65E+02
R <sub>6</sub>	1.15E-08	-2.79E-06	2.34E-04	-7.65E-03	9.16E-02
C <sub>6</sub>	-1.31E-04	3.14E-02	-2.51E+00	7.04E+01	1.00E-03
R <sub>7</sub>	-4.69E-09	1.06E-06	-7.70E-05	2.21E-03	4.49E-02
C <sub>7</sub>	-2.24E-05	6.99E-03	-7.23E-01	2.66E+01	2.85E+02
R <sub>8</sub>	1.40E-07	-3.19E-05	2.57E-03	-8.50E-02	1.13E+00
C <sub>8</sub>	-1.56E-04	3.91E-02	-3.28E+00	1.01E+02	1.00E-03

The final step in developing the battery models is using the value of the circuit components in the ODE associated with their respective circuits to determine the battery terminal voltage given in (2-9).

$$V_{bat} = OCV - L_0 \frac{dI_b}{dt} - R_0 I_b - R_1 (I_b - C_1 \frac{dV_{R_1 C_1}}{dt}) \cdots - R_n (I_b - C_n \frac{dV_{R_n C_n}}{dt}) \quad (2-8)$$

Where,  $I_b$  and  $V_{R_n C_n}$  are the battery current and RC element's voltage, respectively.

Modeling battery with the linear least square method with the Modulab software is based on expert knowledge from the user, as it needs to suggest a circuit topology for the software to fit. Also, variations for this topology are made by painstakingly fixing specific parameters to manipulate the circuit correctly, which requires intensive personnel involvement. Therefore, machine learning algorithms are explored as an alternative in the next section.

#### 2.4.2 Developing ECM with Bayesian Model

Bayesian Network (BN) is a probabilistic presentation of process models with a directed acyclic graph including nodes and arrows (called edges). In Bayesian modeling, all variables can be divided into two groups of “Observations” and “Unobserved” values. In Bayes’ theorem, the vector of unobserved variables ( $\theta$ ) including model’s parameters and intermediate unseen variables can be calculated conditional to a vector of observations (measurements) ( $y$ ), using joint probabilities as given in (2-10).

$$[\theta|y] = \frac{[\theta, y]}{[y]} = \frac{[y|\theta][\theta]}{[y]} \quad (2-9)$$

Where,  $[\theta|y]$  is the posterior distribution,  $[y|\theta]$  is the likelihood, and  $[\theta]$  is the prior distribution. Here  $[y]$  is the marginal distribution of observations on the unobserved variables  $\theta$  as observed in (2-11). This probabilistic expression can include all uncertainties



such as sampling, measurement and process uncertainties in the calculation of an unobserved variable through the definition of probability distributions' parameters.

$$[y] = \int [y|\theta][\theta]d\theta \quad (2-10)$$

To model the battery OCV and impedance from the experiments, the first step is to define the observed and unobserved variables and define the graphical structure of the Bayesian network as Figure 2.13. Our expert domain knowledge was used to create the network structure, other such models exist that may be statistically indistinguishable based on the independencies/dependencies entailed by the model.

The observed variables in HPPC tests are  $DOD_k$  and  $OCV_k$  with K measurements. For EIS tests, the battery state of charge  $SOC_i$  and battery impedance  $Z_{batt, ij}$  in I observations with J measurements in each observation of impedance. Unobserved variables are the estimated R, L and C circuit elements. The estimated depth of discharge and state of charge is  $\overline{DOD}_k$  and  $\overline{SOC}_i$  respectively. The parameters are  $\alpha, \beta, \gamma$ , and  $\eta$ . The estimated real and imaginary parts of the impedance are  $Z'_{ij}$  and  $Z''_{ij}$ . Based on the network, we can write the mathematical expression of the Bayesian network as (2-12). Note that in (2-12), the sign between left and right side of the expression is “ $\propto$ ” instead of “ $=$ ”. This is because it is not possible to calculate the marginal distribution of observations for all values of unobserved quantities.

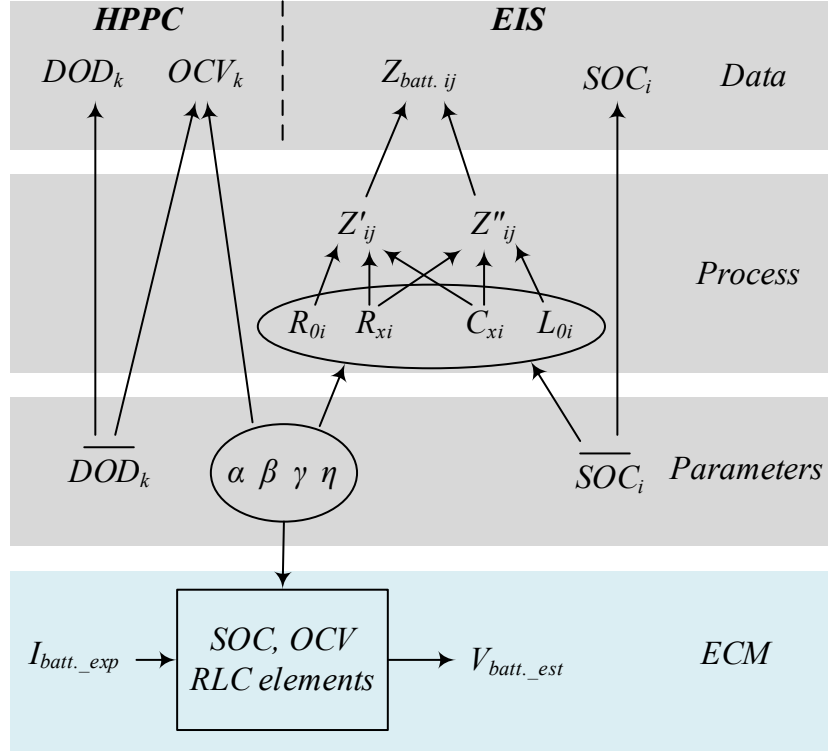


Figure 2.13. Bayesian network for the ECM model

$$\begin{aligned}
 & [R_0, L_0, R_x, C_x, Z', Z'', \overline{SOC}, \overline{DOD}, \alpha, \beta, \gamma, \eta | OCV, SOC, DOD, Z_{batt}] \\
 & \propto \prod_{i=1}^I \prod_{j=1}^J [Z_{ij} | Z'_{ij}] \times [Z_{ij} | Z''_{ij}] \times [Z'_{ij} | R_{0i}] \\
 & \prod_{k=1}^K [DOD_k | \overline{DOD}_k] \times [OCV_k | \alpha, \beta, \gamma, \eta, \overline{DOD}_k] \\
 & \times [Z''_{ij} | L_{0i}] \times [Z'_{ij} | R_{xi}, C_{xi}] [Z''_{ij} | R_{xi}, C_{xi}] [R_{0i} | \alpha, \beta, \gamma, \eta, \overline{SOC}_i] \\
 & \times [L_{0i} | \alpha, \beta, \gamma, \eta, \overline{SOC}_i] [R_{xi} | \alpha, \beta, \gamma, \eta, \overline{SOC}_i] [C_{xi} | \alpha, \beta, \gamma, \eta, \overline{SOC}_i] \\
 & \times [\alpha] \times [\beta] \times [\gamma] \times [\eta] [\overline{SOC}_i] \times [\overline{DOD}_k]
 \end{aligned} \tag{2-11}$$

Therefore, the Markov Chain Monte Carlo (MCMC) algorithm is used to calculate the posterior distributions and the Metropolis-Hastings method [27] is applied for sampling. To apply the MCMC algorithm, full conditionals for all random variables are calculated. The PDFs for the variables are chosen based on the requirements of each

variable. For instance, R, L, and C elements have “gamma” PDFs as they have positive values. The BN model’s outputs for a sample circuit element  $R_0$  are shown in Figure 2.14. For 5000 MCMC samples, the histogram and fitted gamma distribution is depicted in Figure 2.14, which proves the successful MCMC sampling. Figure 2.15 presents the estimated gamma PDFs of  $R_0$  in various SOC levels and using these distributions, the model parameters’ PDFs are estimated, and sample results are shown in Figure 2.16.

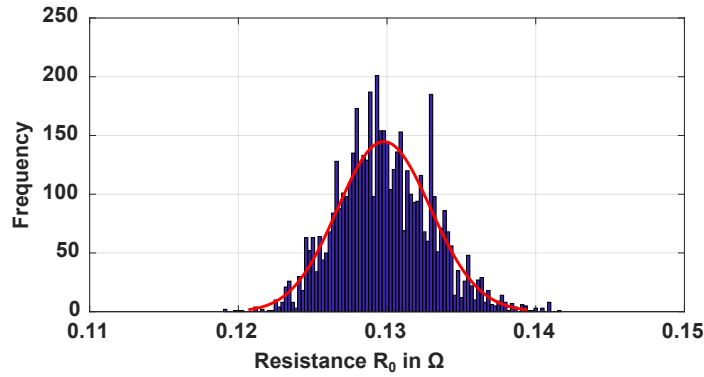


Figure 2.14. The Bayesian model outputs histogram for  $R_0$ .

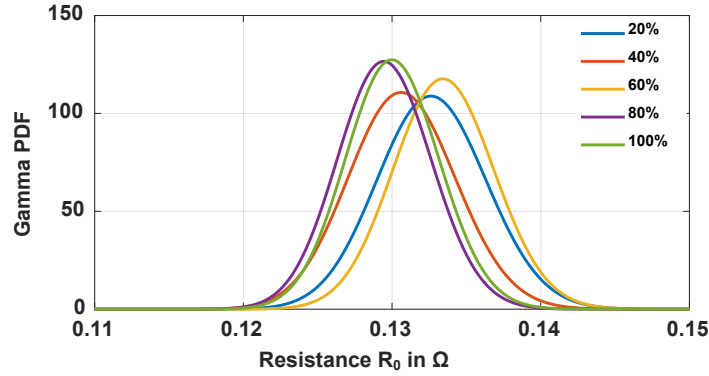


Figure 2.15. The Bayesian model output gamma PDF for  $R_0$  at various SOC levels.

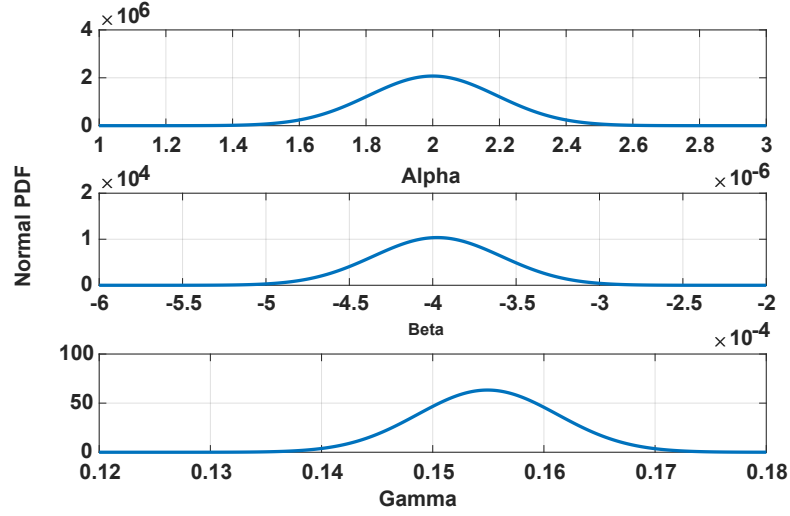


Figure 2.16. The Bayesian model output normal PDF of parameters for  $R_0$ .

Table 2.6. BN 2RC and 3RC model Data at 20°C

		20% SOC		80% SOC	
		Mean	SD	Mean	SD
2RC	$R_0$	0.1475	0.0035	0.1372	0.0035
	$L_0$	1.9E-08	2.05E-9	2.8E-08	2.84E-09
	$R_1$	0.0681	0.0029	0.0444	0.0025
	$C_1$	0.6456	0.0527	0.1836	0.0172
	$R_2$	0.1819	0.0086	0.2040	0.0080
	$C_2$	313.19	18.516	218.73	11.480
3RC	$R_0$	0.1311	0.0037	0.1298	0.0032
	$L_0$	5.7E-07	5.5E-08	3.6E-07	3.5E-08
	$R_1$	0.0346	0.0026	0.0407	0.0024
	$C_1$	0.0704	0.0064	0.0875	0.0078
	$R_2$	0.0577	0.0087	0.0301	0.0054
	$C_2$	1.6017	0.1639	22.669	2.135
	$R_3$	0.1722	0.0177	0.1957	0.0197
	$C_3$	322.87	18.562	263.78	16.203

After estimating the parameters' distributions, they are used to generate the ECM model and estimate the battery voltage  $V_{batt\_est}$  for a given experimental current  $I_{batt\_est}$ .

Table 2.6 presents the circuit elements estimated by the BN model for two SOC's.

## 2.5 Impedance Analyzer vs. Bayesian Network Models

This section compares the ECM developed by the Impedance Analyzer and BN models. Three ECMs (8RC, 3RC, and 2RC) were developed with Impedance Analyzer with varying accuracy. Whereas for BN, two ECMs (3RC and 2RC) were developed. The BN model was limited to 3RC as it was comparable to 8RC models from the Impedance Analyzer, albeit demanding more mathematical processing time and resource. However, the BN models are more successful in terms of accuracy and precision in estimating the internal impedance of the battery. The following discussion elaborates on this in terms of fitting accuracy, errors in percentage in real and imaginary parts, and validation under typical commercial Li-ion battery load.

### 2.5.1 Estimation Accuracy

Using the Impedance Analyzer, three ECM models with different levels of accuracy are developed as 8RC, 3RC and 2RC circuits. These results are compared to ECMs with 3RC and 2RC developed through BN. The BN development is focused on 3RC and 2RC as these are the cases where the impedance analyzer software presents less accurate models, as explained below. Figure 2.17 presents the Impedance Analyzer model results for 80% SOC. From Figure 2.17, it is evident that the 8RC ECM produces a superior fit as opposed to 3RC and 2RC. The 8RC ECM deploys 3RC's for each arc and 2RC's for the diffusion region. Having multiple RC's in a single region produces a better fit because each RC pair can fit a smaller semi-circle, which can be part of an arc-shaped trajectory. The cumulative effect of such multiple RC produces accurate fitting. Since this cannot be obtained through

3RC and 2RC circuits in the Impedance Analyzer fitting software, their ECMs are less accurate.

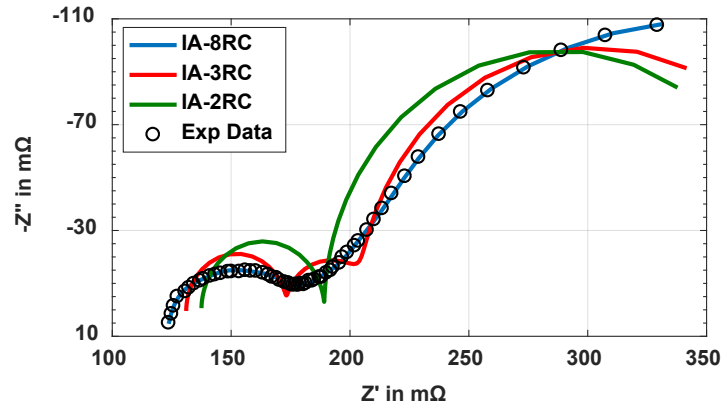


Figure 2.17. Accuracy of various Impedance Analyzer model at 20°C and 80% SOC.

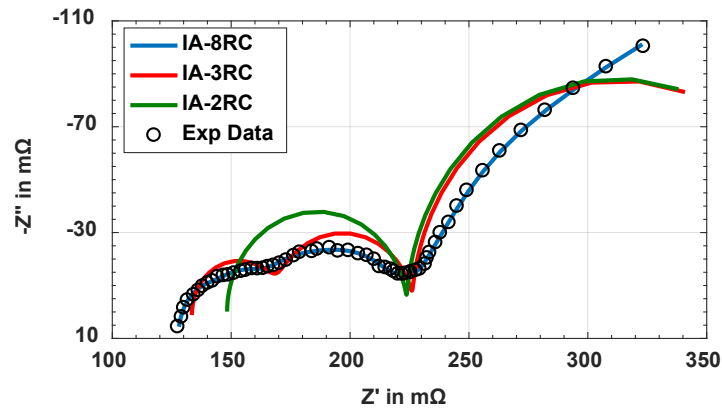


Figure 2.18. Accuracy of various Impedance Analyzer model at 20°C and 20% SOC.

A similar discussion is applicable for the 20% SOC result that has two semi-circles in the impedance profile as in Figure 2.18. The R square values of the three models are calculated as 0.999, 0.980 and 0.941 for 8RC, 3RC, and 2RC circuits, respectively, signifying the accuracy of the fitting.

However, using BN models results in an even more accurate impedance estimation for the same number of RC circuits. The impedance results of 3RC and 2RC ECM models from BNs for 80% and 20% SOC are presented in Figure 2.19 and Figure 2.20. Results

show they are clearly more accurate in higher frequencies than 3RC and 2RC ECMs and comparable to 8RC ECM from the Impedance Analyzer software. The BN-based 3RC and 2RC models have R-square equal to 0.993 and 0.982 respectively, which indicates the successful impedance estimation with BN models. Comparing the R2 of BN models to the Impedance Analyzer models illustrate that the BN approach can achieve higher R-square values (better estimation) with a lower number of RC circuits.

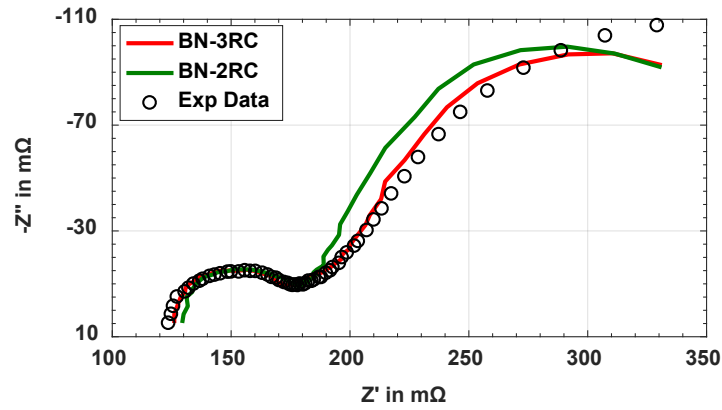


Figure 2.19. Accuracy of various BN models at 20°C and 80% SOC.

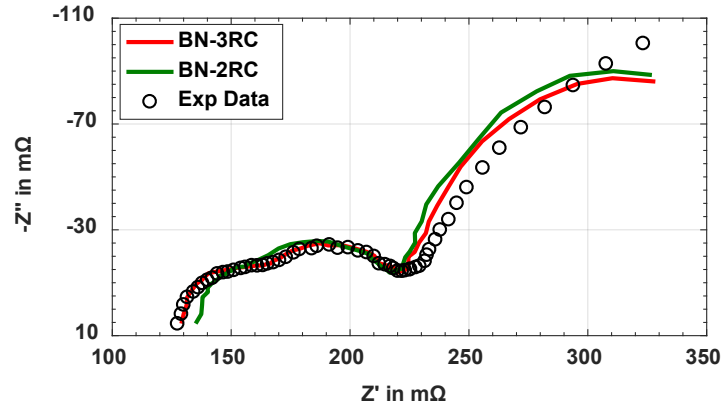


Figure 2.20. Accuracy of various BN models at 20°C and 20% SOC.

### 2.5.2 Estimation Error Analysis

To illustrate the error percentage distribution in different models, the error data for real and imaginary parts of the battery impedance is modeled by Rayleigh distribution as depicted in Figure 2.21 and Figure 2.22, for both Impedance Analyzer and BN models respectively. Based on Figure 2.21, for Impedance Analyzer models, the average impedance error value for the 8RC circuit is 3.3%, which is about 6 and 8.5 times less than the 3RC and 2RC models, respectively. This indicates that the 8RC model error is more concentrated around smaller values compared to the 2RC and 3RC models error data, in both the real and imaginary parts. However, for the BN models, the 3RC circuit has a 3.5% average error and the 2RC circuit has a 4.6%, which are slightly more than the average error value for 8RC circuit in Impedance Analyzer model, nonetheless, it is significantly lower than that of Impedance Analyzer 3RC and 2RC models. Therefore, BN models can reach higher precision with a reduced number of RC circuits.

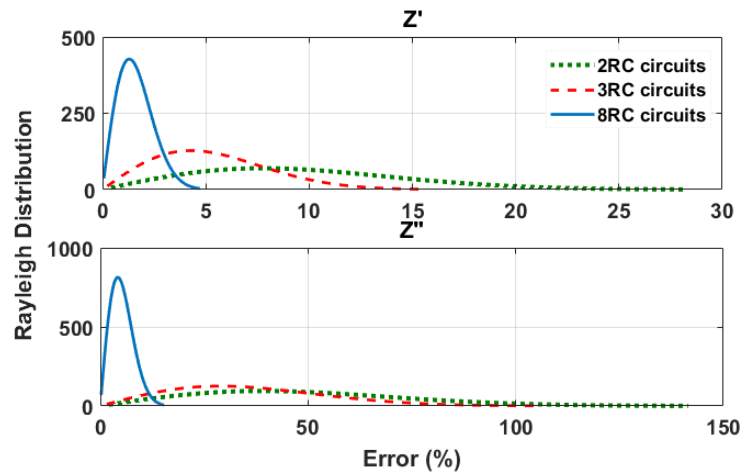


Figure 2.21. The probability distribution of fitting error for real and imaginary parts of impedance in Impedance Analyzer models.



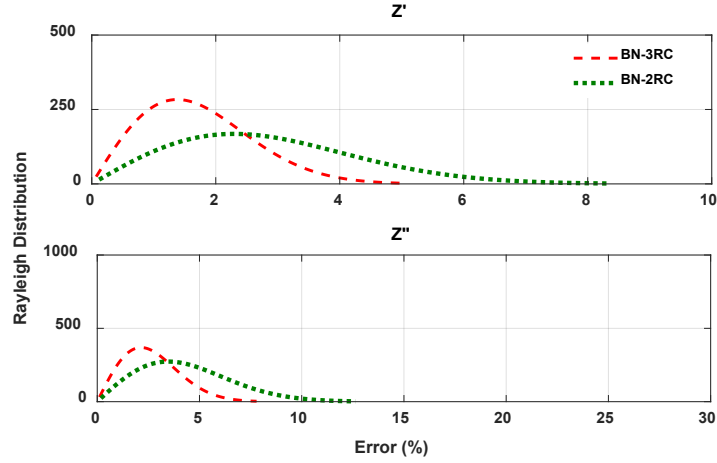


Figure 2.22. The probability distribution of estimation error for real and imaginary parts of impedance in BN models.

In addition, it is important to note that the fitting result of the imaginary part has higher error values than the real part in all three models of Impedance Analyzer. The average error in the real part of battery impedance is almost 5 times less than the average imaginary part of the impedance. It shows that the impedance fitting circuits with Impedance Analyzer are more successful in modeling the resistive properties of the battery impedance than the capacitive properties. However, in the BN models, there is no significant difference between real and imaginary parts' estimation errors. The probability density function (PDF) for the Rayleigh distribution of the error data is given by (2-13). Where  $E$  is the error data and  $\sigma$  is the scale factor of the distribution which can be used to calculate the mean and variance of the distribution as shown in (2-14) and (2-15).

$$f(E, \sigma) = \frac{E}{\sigma^2} e^{(-E^2/2\sigma^2)} \quad E \geq 0 \quad (2-12)$$

$$Mean = \sigma \sqrt{\frac{\pi}{2}} s \quad (2-13)$$

$$Variance = \left(2 - \frac{\pi}{2}\right) \sigma^2 \quad (2-14)$$

Table 2.7. Rayleigh distribution parameters of impedance fitting and BN estimation

		<b>Scale Factor</b>	<b>Mean</b>	<b>Variance</b>
$Z'$	2RC	7.774	9.743	25.94
	3RC	4.296	5.385	7.923
	8RC	1.296	1.624	0.721
	BN-2RC	2.294	2.875	2.259
	BN-3RC	1.378	1.727	0.8150
$Z''$	2RC	38.92	48.78	650.3
	3RC	28.95	36.28	359.7
	8RC	4.016	5.034	7.629
	BN-2RC	4.975	6.249	17.99
	BN-3RC	4.143	5.196	11.35

The numerical results of the Rayleigh distribution are presented in Table 2.7. These results show that the average value of the error distribution in the 8RC model for both the resistive and capacitive parts of the impedance is 1.6% and 5%. This is significantly less than the 3RC and 2RC models as observed in Figure 2.21 and Figure 2.22. In addition, the variance of the error distribution is higher for the 2RC and 3RC models compared to the 8RC model. For the BN models, numerical results of the 3RC circuit model are very close to the 8RC circuit of Impedance Analyzer which proves the superior accuracy of BN models.

### 2.5.3 Drive Cycle Validation

The battery model was experimentally validated by a custom drive cycle tailored for a commercial Li-ion battery, as shown in Figure 2.23. A hardware-in-loop simulation was performed with the experimental setup as Figure 2.2 where the battery was the hardware and the load is simulated to represent a typical application for commercial Li-ion batteries. The drive cycle is almost 5 hours long with a periodic discharge pulse and regenerations. The SOC of the battery decreases by 35% throughout the cycle (60% to 25%).

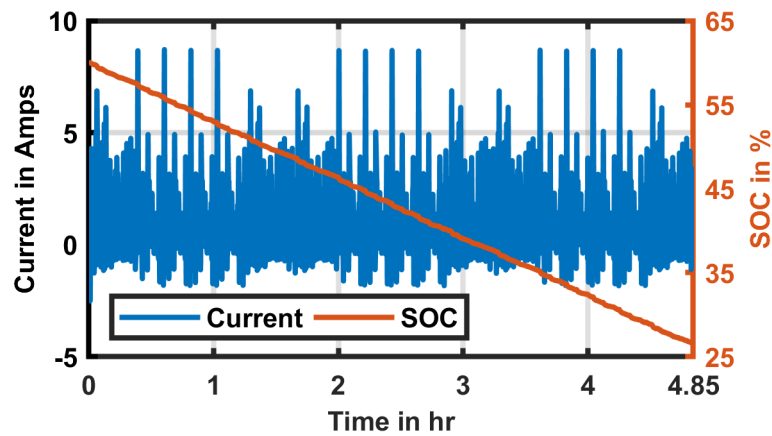


Figure 2.23. The experimental load current and battery SOC%.

It can be seen from Figure 2.24 that the fitting result of 8RC ECM has produced acceptable results. Though the testing drive cycle is highly dynamic, the simulated voltage has predicted the experimental voltage with the utmost accuracy. For the 8RC model, the relative error is less than 1% while the error RMS is 0.6%. It can also be deduced from Figure 2.24 that the 8RC ECM overestimates the battery terminal voltage. A similar trend can be observed from the 3RC and 2RC models, where the ECM overestimates the battery terminal voltage. The 3RC started the drive cycle with slightly more than 1% relative error.

Throughout the cycle, the error was increasing. Near the end of the cycle, both 3RC and 2RC were identical with a higher degree of error.

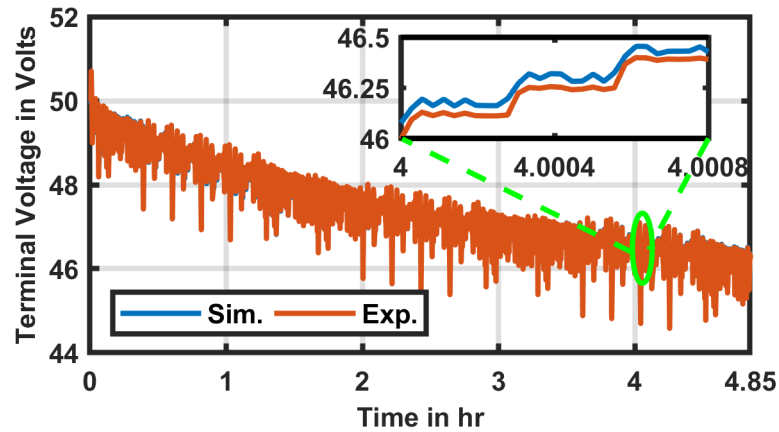


Figure 2.24. The experimental validation of 8RC ECM developed with Impedance Analyzer fitting.

This can be observed from an enlarged sub-section of the battery terminal voltage produced by each ECMs developed through Impedance Analyzer fitting in Figure 2.25. The 8RC ECM estimation is highly accurate as opposed to 3RC and 2RC. For discharging, regenerative and idle cases, 8RC ECM can replicate the battery behavior with minimal error. Moreover, 2RC and 3RC ECM performance are nearly identical. Thus, no significant improvement can be obtained by developing a 3RC ECM over a 2RC through the Impedance Analyzer software. However, as shown in Figure 2.26, the battery voltage estimations with the BN models have a lower deviation from the experimental results. The BN models overestimate the voltage drop on the battery impedance while the models from Impedance Analyzer underestimate. In addition, the voltage difference from the experimental data in the BN 3RC model is very similar to the Impedance Analyzer 8RC circuit. This validation proves that higher accuracy of the model can be reached with a reduced number of RC circuits in the BN approach.

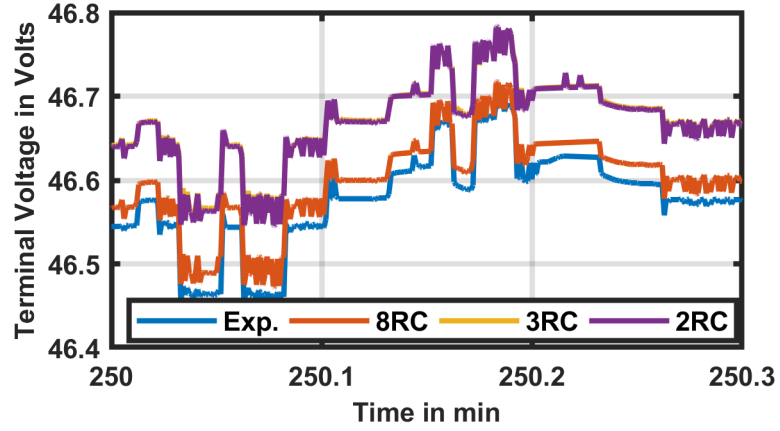


Figure 2.25. Accuracy of Impedance Analyzer models

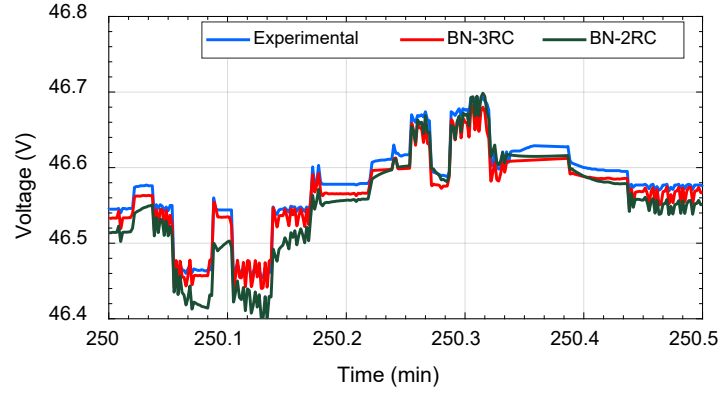


Figure 2.26. Accuracy of BN models

## 2.6 Conclusion

In this chapter, a commercial Li-ion battery is tested in both time-domain and frequency-domain at multiple SOC's and temperature scenarios. The experimental results are used to generate ECM models with different accuracy including 2RC, 3RC and 8RC elements by two approaches: Impedance Analyzer fitting and Bayesian Networks. The accuracy of these ECMs was analyzed in terms of fitting, impedance and battery voltage. A custom drive cycle for commercial Li-ion battery was used to validate simulated models. These are highlighted observations from the results are discussed in the following sections.

Higher temperatures cause higher inductive properties in the battery, while lower temperatures increase its resistive properties. Also, the impact of Li-ion diffusion on the battery impedance is more observable in higher temperatures, whilst in lower temperatures, the effect of SEI, double-layer capacitance, and charge transfer resistance are more distinguishable.

The difference in SEI impedance vs double-layer capacitance and charge transfer resistance is detectable in lower SOC as two semi-circles are separate.

In developing different ECMs by Impedance Analyzer fitting, it was proved that the 8RC model is more precise in all frequencies compared to the 2RC and 3RC models. The 8RC circuit fitting leads to a 3.3% average error in impedance presentation, while the 3RC and 2RC models are at 20.8% and 29.3%. These errors are particularly relevant to the imaginary part of impedance (capacitive properties).

Bayesian Network approach leads to a higher accuracy with a reduced number of RC circuits. Impedance estimation with 3RC BN has a similar error percentage (3.5%) with the Impedance Analyzer 8RC model. Even the BN 2RC model has a significantly lower error percentage (4.6%) compared to the Impedance Analyzer 2RC model.

The battery terminal voltage validation with the developed ECM models through the Impedance Analyzer and BNs show that the normalized RMS error (NRMSE) percentage for 8RC, 3RC, and 2RC Impedance Analyzer models are 0.6, 1.3 and 1.4 respectively. These results indicate that despite having higher impedance fitting errors in the 2RC and 3RC models, the terminal voltage is not very sensitive to model impedance precision. In

addition, the BN 3RC and 2RC models are more precise in the voltage calculation compared to the 3RC and 2RC Impedance Analyzer models.

Although the implementation of the BN approach is more complicated than the Impedance Analyzer modeling approach, it can estimate the battery's dynamic behavior with a lower number of elements (lower degrees of freedom) due to the merit of Bayesian statistics.

## References

- [1] P. P. Malysz, L. Gauchia, and H. H. Yang, "Fundamentals of electric energy storage systems," *Adv. Electr. Drive Veh.*, pp. 237–282, 2014.
- [2] M. Jafari, A. Gauchia, S. Zhao, K. Zhang, and L. Gauchia, "Electric Vehicle Battery Cycle Aging Evaluation in Real-World Daily Driving and Vehicle-to-Grid Services," *IEEE Trans. Transp. Electrification*, vol. 4, no. 1, pp. 122–134, Oct. 2017.
- [3] R. G. Jungst *et al.*, "Accelerated calendar and pulse life analysis of lithium-ion cells," *J. Power Sources*, vol. 119–121, pp. 870–873, 2003.
- [4] C. H. Chen, J. Liu, and K. Amine, "Symmetric cell approach and impedance spectroscopy of high power lithium-ion batteries," *J. Power Sources*, vol. 96, no. 2, pp. 321–328, 2001.
- [5] M. Farag, M. Fleckenstein, and S. R. Habibi, "Li-Ion Battery SOC Estimation Using Non-Linear Estimation Strategies Based On Equivalent Circuit Models." SAE International, 2014.
- [6] D. V Do, C. Forgez, K. E. K. Benkara, and G. Friedrich, "Impedance Observer for a Li-Ion Battery Using Kalman Filter," *IEEE Trans. Veh. Technol.*, vol. 58, no. 8, pp. 3930–3937, 2009.
- [7] D. Andre, M. Meiler, K. Steiner, H. Walz, T. Soczka-Guth, and D. U. Sauer, "Characterization of high-power lithium-ion batteries by electrochemical impedance spectroscopy. II: Modelling," *J. Power Sources*, vol. 196, no. 12, pp. 5349–5356, 2011.
- [8] M. Jafari, A. Gauchia, K. Zhang, and L. Gauchia, "Simulation and Analysis of the Effect of Real-World Driving Styles in an EV Battery Performance and Aging,"

*IEEE Trans. Transp. Electrification*, vol. 1, no. 4, pp. 391–401, Dec. 2015.

- [9] J. Li, M. Mazzola, J. Gafford, and N. Younan, “A new parameter estimation algorithm for an electrical analogue battery model,” in *2012 Twenty-Seventh Annual IEEE Applied Power Electronics Conference and Exposition (APEC)*, 2012, pp. 427–433.
- [10] A. Hentunen, T. Lehmuspelto, and J. Suomela, “Time-Domain Parameter Extraction Method for Thevenin-Equivalent Circuit Battery Models,” *IEEE Trans. Energy Convers.*, vol. 29, no. 3, pp. 558–566, 2014.
- [11] Y. C. Hsieh, T. D. Lin, R. J. Chen, and H. Y. Lin, “Electric circuit modelling for lithium-ion batteries by intermittent discharging,” *IET Power Electron.*, vol. 7, no. 10, pp. 2672–2677, 2014.
- [12] Y. Cao, R. C. Kroeze, and P. T. Krein, “Multi-timescale Parametric Electrical Battery Model for Use in Dynamic Electric Vehicle Simulations,” *IEEE Trans. Transp. Electrification*, vol. 2, no. 4, pp. 432–442, 2016.
- [13] K. Li and K. J. Tseng, “An equivalent circuit model for Li-ion batteries used in energy storage systems in building environment,” in *2016 IEEE Innovative Smart Grid Technologies - Asia (ISGT-Asia)*, 2016, pp. 504–510.
- [14] D. Gandolfo, A. Brandão, D. Patiño, and M. Molina, “Dynamic model of lithium polymer battery – Load resistor method for electric parameters identification,” *J. Energy Inst.*, vol. 88, no. 4, pp. 470–479, 2015.
- [15] A. Baba *et al.*, “Simultaneous Estimation of the SOC and Parameters of Batteries for HEV/EV.” SAE International, 2016.
- [16] A. Baba and S. Adachi, “SOC Estimation of HEV/EV Battery Using Series Kalman Filter,” *Electr. Eng. Japan*, vol. 187, no. 2, pp. 53–62, 2014.
- [17] Y. Tian, B. Xia, W. Sun, Z. Xu, and W. Zheng, “A modified model based state of charge estimation of power lithium-ion batteries using unscented Kalman filter,” *J. Power Sources*, vol. 270, pp. 619–626, 2014.
- [18] L. H. Saw, Y. Ye, and A. A. O. Tay, “Electro-thermal analysis and integration issues of lithium ion battery for electric vehicles,” *Appl. Energy*, vol. 131, no. 0, pp. 97–107, 2014.
- [19] T. Huria, G. Ludovici, and G. Lutzemberger, “State of charge estimation of high power lithium iron phosphate cells,” *J. Power Sources*, vol. 249, pp. 92–102, 2014.
- [20] T. Tanaka *et al.*, “Accurate and versatile simulation of transient voltage profile of lithium-ion secondary battery employing internal equivalent electric circuit,” *Appl.*



*Energy*, vol. 143, pp. 200–210, 2015.

- [21] B. Saha, K. Goebel, S. Poll, and J. Christophersen, “Prognostics Methods for Battery Health Monitoring Using a Bayesian Framework,” *IEEE Trans. Instrum. Meas.*, vol. 58, no. 2, pp. 291–296, 2009.
- [22] Z. He, M. Gao, G. Ma, Y. Liu, and S. Chen, “Online state-of-health estimation of lithium-ion batteries using Dynamic Bayesian Networks,” *J. Power Sources*, vol. 267, pp. 576–583, 2014.
- [23] G. Jin, D. E. Matthews, and Z. Zhou, “A Bayesian framework for on-line degradation assessment and residual life prediction of secondary batteries in spacecraft,” *Reliab. Eng. Syst. Saf.*, vol. 113, pp. 7–20, 2013.
- [24] S. S. Y. Ng, Y. Xing, and K. L. Tsui, “A naive Bayes model for robust remaining useful life prediction of lithium-ion battery,” *Appl. Energy*, vol. 118, pp. 114–123, 2014.
- [25] W. Wang, P. Malysz, K. Khan, L. Gauchia, and A. Emadi, “Modeling, parameterization, and benchmarking of a lithium ion electric bicycle battery,” in *2016 IEEE Energy Conversion Congress and Exposition (ECCE)*, 2016, pp. 1–7.
- [26] S. Buller, “Impedance-based simulation models for energy storage devices in advanced automotive applications,” Ph. D. Dissertation, RWTH Aachen, Aachen, Germany, 2003.
- [27] W. K. Hastings, “Monte Carlo Sampling Methods Using Markov Chains and Their Applications,” *Biometrika*, vol. 57, no. 1, pp. 97–109, 1970.

## Chapter 3

# Residential Battery Degradation in Smart Home Using Hierarchical Bayesian Network

### Abstract

The battery energy storage is crucial in enabling a smart home to participate in multiple grid services while maintaining desired operational requirements from end-users. The major challenge for a battery energy storage system is degradation as it reduces the available capacity and power. In this chapter, a detailed hierarchical Bayesian Network (BN) is developed to evaluate the capacity fade degradation of a residential battery energy storage in a smart home environment. The BN utilizes a stochastic method to relate the causal factors of residential battery degradation. Experimental results of lithium iron phosphate batteries were used to train the BN. The capacity fade was evaluated for several cases, originated from a smart home energy management system (SHEMS). The cases show that the capacity fade of the residential battery system relies heavily on SHEMS architecture, load characteristics, user preferences, and geographical location. The case studies revealed that performing grid services reduces the capacity fade by 3% more. Furthermore, geographical location with higher temperature and solar irradiance can have

up to 5% more capacity fade with similar load patterns while reducing electricity consumption by 40%.

### **3.1 Introduction**

The smart home is an essential part of the smart grid, which provides the end-user with reliable, secure and efficient energy while reducing emissions and electricity bills [1], [2]. A smart home integrates several flexible loads, controllable devices, renewable energy sources, and battery energy storage, allowing demand side management through a smart home management system (SHMS) [3]. Due to the falling cost of lithium-ion batteries, it is the most popular choice for a residential battery energy storage system [4]. The residential energy storage battery is supported by renewable energy sources and flexible loads that enable SHEMS to perform several grid services, i.e. capacity support, peak shaving, energy arbitrage, PV curtailment reduction, and voltage support while honoring end-user operational preferences [1]. Thus, allowing the end-user to participate in the electricity market to offset the electricity bill. The major concern in this regard is battery degradation and associated degradation cost, accounting for the usage of the battery.

Past relevant works showed a similar concept while working on vehicle-to-grid (V2G), where a stationary vehicle battery was used to perform ancillary services. However, it was observed in multiple cases that participating in grid services reduces battery life significantly [5]–[7]. Authors in [8] and [9] showed that revenue earned through grid services was nullified by battery degradation cost. Therefore, it is critically important to consider battery degradation while incorporating the battery in a smart home.

There are two main approaches to determine battery degradation: data-based prognostics and model-based studies [10]. The data-based prognostics use a set of data for training. Afterward, the remaining usable life or battery state of health of the battery is predicted by using the present measurement data. This sort of approach is most suitable for online applications due to their design, characteristics, and calculation load [11]. Contemporary researchers use various data-based prognostics, i.e. Kalman Filters [12] and relevance vector machine [13]. On the other hand, the model-based research predicts battery degradation from mathematical expressions, obtained by fitting extensive experimental battery performance data, i.e. solid electrolyte interface (SEI) growth [14], cyclable lithium loss [15], internal impedance growth determined through electrochemical impedance spectroscopy (EIS) fitted to an equivalent circuit model [16] and Arrhenius equation-based models supported by extensive experimental research [17].

Past works on residential battery energy storage systems use some of these techniques to incorporate battery degradation. In most cases, battery degradation is ignored, due to the complex nature of batteries [18]–[21]. Other researchers consider battery capacity fade modeled through empirical studies [4]. Abdulla et al. [18] proposed a method to determine a total number of kWh until the end of life (EoL) using rain-flow counting of battery cycles, based on nominal battery cycle life and SOC. Mamun et al. [22] utilized SEI growth on the electrode to evaluate the capacity fade and applied a \$/kWh degradation factor of the battery in the optimization problem. Cai et al. [23] determined the capacity fade with both SEI formation and active material loss or loss of cyclable lithium. Afterward, the determined capacity fade is related to the SOC and battery power by fitting.

Riffonneau et al. [24] determined capacity fade in terms of SOC only, but the capacity fade was determined only during discharge.

The model-based approach of battery degradation modeling relies on deterministic mathematical equations and assumes factors affecting degradation remain constant throughout the cycling process. However, neither the degradation phenomena are deterministic, nor the factors remain constant during the lifetime of the battery. In a smart home, the capacity fade of the battery depends on the type of household loads, user preferences, availability of renewable sources, weather and temperature variation, participation in the electricity market and electricity price. Most of these factors need to be explained with probability distributions as they inherently contain a level of uncertainty. Also, the capacity fade of the battery has a causal relationship to the external factors. Thus, deterministic methods are not reliable in evaluating capacity fade for a battery.

Bayesian Network is a data-driven method that allows the incorporation of uncertainty in the measurement of data and process, estimates the hidden processes, provides probability distribution instead of point value estimation and shows the causal relationship between different processes for battery capacity fade evaluation. Therefore, Bayesian models can provide a more insightful and accurate evaluation of battery capacity fade. The battery degradation can be analyzed in terms of capacity fade and power capability. This chapter solely focuses on exploring the capacity fade of the battery as a manifestation of degradation. The contributions of this chapter, as opposed to the state of the art, are listed below.

- A more reliable, secure and accurate probabilistic battery capacity degradation method through hierarchical BN is discussed, contrasting the contemporary deterministic approach.
- A BN and associated probability distribution-based equation are developed utilizing prior lab-based experimental results for a residential battery energy storage system.
- Associating battery capacity fade with external environmental factors rather than solely implicating battery parameters.

The rest of the chapter is organized as follows. Section 3.2 describes the SHEMS simulation which generates different scenarios for the BN. In section 3.3, a detailed explanation of the development of the BN is discussed. Section 3.4 provides the results and discussion on capacity fade and associated causal factors obtained from the BN for multiple scenarios followed by the conclusion. The nomenclature used in this chapter is given in Table 3.1.

Table 3.1. List of nomenclatures

Terms	Description
$P_t^I$	Inflexible load power consumption at t (kW)
$P_t^{Bu}, P_t^{Bs}$	Battery power used for residential loads and sold to the grid at t (kW)
$P_t^{Bch}, P_t^{Bdch}$	Battery charge and discharge power at t (kW)

$\eta_{ch}^B, \eta_{dch}^B$	Battery charging and discharging efficiency
$R_{max}^{Bch}, R_{max}^{Bdch}$	Battery maximum charging and discharging power (kW)
$P_t^{EVu}, P_t^{EVs}$	EV battery power used for residential loads and sold to the grid at t (kW)
$P_t^{EVch}, P_t^{EVdch}$	EV battery charge and discharge power at t (kW)
$\eta_{ch}^{EV}, \eta_{dch}^{EV}$	EV battery charging and discharging efficiency
$R_{max}^{EVch}, R_{max}^{EVdch}$	EV battery maximum charging and discharging power (kW)
$u_t^{EV}$	Variable to prevent simultaneous EV battery charge and discharge
$\Delta t$	The time interval between data measurements
$Cap$	Battery rated capacity (Ah)
$I_{ch}, I_{dch}$	Battery charging and discharging current (A)
$SOC_t^{Bin}$	The initial state of charge of the battery
$SOC_t^B$	Battery state of charge at t
$SOC_t^{Bmin}, SOC_t^{Bmax}$	Battery minimum and maximum state of charge at t
$x_t^{lp}, y_t^{lp}, z_t^{lp}$	Phase control variables for phase p and load l at t
$PT^{lp}, PD^{lp}, UP^l$	Cycles required, time delay, and user preference for phase j and load i

$P_t^{SC}, P_t^{PVPro}$	PV power capacity and total power produced at t (kW)
$\eta_2, A$	PV panel efficiency and area
$P_t^{PVu}, P_t^{PVs}$	PV power used for residential loads and sold to the grid at t (kW)
$P_t^{Gr}$	Power purchased from the grid at t (kW)
$P_t^s$	Power sold from residence to the grid at t (kW)
$P_t^{EVu}$	EV power used for residential loads at t (kW)
$PL_t$	Total load power limit at t (kW)
$P_t^{sub}$	Maximum power sold to the grid at t (kW)
$P_t^{Grub}$	Minimum power sold to the grid at t (kW)
$u_t^{Gr}$	Variable to prevent simultaneous power consumption and grid services at t
$C_t^P$	Price of electricity at t
$q_{ij}$	Capacity fade percentage of a battery cell at observation i and measurement j
$T_{rim}$	The internal temperature of residence at observation i and measurement m (°C)
$T_{mid}$	Ambient temperature at observation i and measurement d (°C)
$S_{t_{ic}}$	Solar irradiation GHI at observation i and measurement c (W/m <sup>2</sup> )



$\lambda_i$	Estimation of capacity fade percentage at observation i
$\widehat{T_{r_i}}$	Estimation of internal temperature of residence at observation i
$Ah_i$	Estimation of A-h at observation i
$SOC_i$	Estimation of average SOC at observation i
$I_{c_i}$	Estimation of C-rate for observation i
$V_{o_i}$	Estimation of battery voltage at observation i
$\alpha, \beta, E_a, \eta_1, \zeta, \epsilon$	Battery aging parameters
$\widehat{T_{m_i}}$	Estimation of ambient temp. at observation i
$\widehat{S_{t_i}}$	Estimation of irradiance at observation i
$\widehat{P_{pv_i}}$	Estimation of solar power at observation i
$\widehat{P_{b_i}}$	Estimation of battery power at observation i
$k_{1_i}, \dots, k_{11_i}$	Contribution coefficients of capacity fade for a service i
$P_{gr}$	Grid power consumed
$P_{evU}$	EV power used
$P_{wm}$	Washing machine power consumption

$P_{dw}$	Dishwasher power consumption
$P_{dry}$	Clothes dryer power consumption
$P_{ac}$	HVAC power consumption
$P_{ewh}$	Electric water heater power consumption
$P_{evC}$	EV charging power provided
$P_I$	Inflexible load power consumption
$P_{gs}$	Power used for grid services

---

### 3.2 Smart Home Energy Management System

A smart home energy management system (SHEMS) has the capability to schedule various types of household loads that helps to minimize the electricity bills without compromising user comfort. SHEMS system communicates with different household loads in real-time, while taking input from the user through, and receives day ahead prices [25]. It can develop an optimized load schedule for the household loads utilizing day ahead prices available. This optimization can curtail electricity usage and increases energy utilization efficiency [26]. The inclusion of a residential battery, plug-in hybrid/electric vehicle and renewable source such as solar photovoltaic (PV) enables SHEMS to perform grid services. Therefore, SHEMS is essential for successful demand-side load management. In this SHEMS simulation, a discrete linear load and generation model is used, as the overall system operation is considered in discrete time with a finite horizon,  $T$ ,

and equal time interval,  $\Delta t$ . The SHEMS simulation comprises various types of loads, a residential battery, an electric vehicle (EV) and PV panels. The following assumptions were considered: the smart meter receives day-ahead electricity price while having the capability to log consumption statistics, the weather forecast is available from the data center and each load can communicate with the meter.

### **3.2.1 Load Models**

Multiple types of loads with varying characteristics are included in the SHEMS model to have an accurate representation of the general household setup. The household loads according to demand flexibility can be divided into two broad categories, inflexible and flexible loads. Inflexible loads do not follow any schedule and depend on highly stochastic usage patterns of the residents [3]. On the other hand, as the name suggests, flexible loads can be scheduled. According to the unique properties, the flexible loads are divided again into three categories, interruptible, uninterruptible, and thermostatically controlled loads. These various types of loads are described in detail in the following parts.

#### ***3.2.1.1 Inflexible Loads***

As mentioned previously, inflexible loads are highly dependent on the behavior of the resident and the smart home energy management system has to provide power to these loads. For example, television and laptop. Such type of loads is modeled by an aggregate base loads [27] as seen in Figure 3.1. Figure 3.1 shows a typical residential inflexible loads profile.

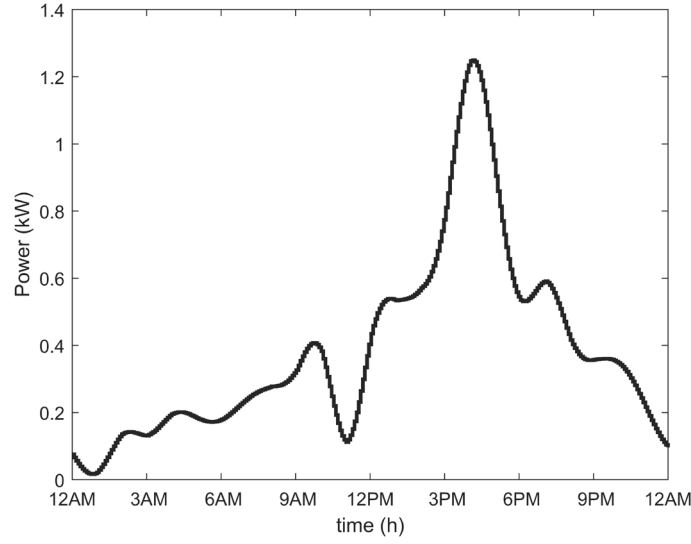


Figure 3.1. Inflexible load profile [27].

### 3.2.1.2 Uninterruptible Loads

Uninterruptible loads can be scheduled but must continue operating once started, i.e., washing machine, dishwasher, and cloth dryer,  $L_U = \{WM, DW, CD\}$  are modeled using single and multi-phase operations. The rated power requirements for the washing machine, dishwasher and dryer are 2kW, 2.2kW, and 1kW, respectively. Each uninterruptible load,  $l$  is operated through multiple phases,  $p$  with three binary variables. Binary variable  $x_t^{lp}$  is high when a load  $l$  is operating in phase  $p$  at time interval  $t$ . Similarly,  $y_t^{lp}$  is high when the operation of that specific load has done operating in that time interval. Also,  $z_t^{lp}$  ensures the same load is barred from operating for a certain time interval  $t$ .

The uninterruptible load must operate a predefined period of cycles whenever it starts it operates as scheduled as ensured by (3-1). Like the clothes dryer needs to operate a certain period for the cloths to be dried to the user's preference. Furthermore, (3-2) ensures

a phase load either must be on or off. Also, once a phase started, it must continue uninterrupted sequential operation through (3-3) and when a phase is completed, it cannot start again by (3-4). Finally, the next phase can only start operating if the previous phase is done is devised by (3-5). Multiphase operation expands on the single phase by including another binary operator. This operator enables a prefixed delay during operation as defined by (3-6). However, the delay can only be introduced if the previous phase is completed as given by (3-7). Finally, there could be certain periods in a day when the user may not want the uninterruptible loads to be scheduled by the energy management system, i.e. operation of loud washing machine or dryer during sleeping hours. These preferences can also be included in the model by introducing another binary variable  $UP_t^l$ , which is high for period  $t$  when the operation is desired and low when not preferred. This variable is related to  $x_t^{lp}$  to control the start of a phase as given by (3-8).

$$\sum_{t=1}^T x_t^{lp} = PT^{lp} \quad , \forall l, p \quad (3-1)$$

$$x_t^{lp} + y_t^{lp} \leq 1 \quad , \forall l, p, t \quad (3-2)$$

$$x_{t-1}^{lp} - x_t^{lp} \leq y_t^{lp} \quad , \forall l, p, t: t > 1 \quad (3-3)$$

$$y_{t-1}^{lp} \leq y_t^{lp} \quad , \forall l, p, t: t > 1 \quad (3-4)$$

$$x_t^{lp} \leq y_t^{l(p-1)} \quad , \forall l, p, t: j > 1 \quad (3-5)$$

$$\sum_{t=1}^T z_t^{lp} = PD^{lp} \quad , \forall l, p \quad (3-6)$$

$$z_t^{lp} = y_t^{l(p-1)} - (x_t^{lp} + y_t^{lp}) \quad , \forall l, p, t: t > 1 \quad (3-7)$$

$$x_t^{lp} \leq UP_t^l \quad , \forall l, p, t \quad (3-8)$$

### 3.2.1.3 Interruptible Loads

Interruptible loads can be interrupted without sacrificing consumer comfort, consume power during the low-price period, i.e. electric vehicles (EVs) and battery energy storage. The interruptible loads,  $L_I = \{B, EV\}$ , can either be load or power supply depending on their charging and discharging cycle. The power produced can either be used to provide grid services or to supply the loads.

#### 3.2.1.3.1 Battery Energy Storage System Load

The battery energy storage is modeled with (3-9) to (3-14). These mathematical solely focus on the operations of the battery energy storage system with the energy management system and residential loads.

$$P_t^{Bu} + P_t^{Bs} = \eta_{dch}^B P_t^{Bdch} \quad , \forall t \quad (3-9)$$

$$0 \leq P_t^{Bdch} \leq R_{max}^{Bdch} (1 - u_t^B) \quad , \forall t \quad (3-10)$$

$$0 \leq P_t^{Bch} \leq R_{max}^{Bch} (u_t^B) \quad , \forall t \quad (3-11)$$

$$SOC_{t+1}^B = SOC_t^B + \frac{\Delta t \cdot (\eta_{ch}^B I_{ch} - \eta_{dch}^B I_{dch})}{100Cap}, t \geq 1 \quad (3-12)$$

$$SOC_t^{Bmin} \leq SOC_t^B \leq SOC_t^{Bmax}, \forall t \quad (3-13)$$

$$SOC_t^B = SOC_t^{Bin}, t = t_o \quad (3-14)$$

Equation (3-9) is the power balance equation, describing the summation of battery power sold and used for the residential load is provided from the total power the battery can discharge. The power balance equation is subject to constraints given by (3-10) to (3-14). Here, (3-9) shows that total power discharged from the battery is the summation of the power distributed to residential loads and the power used for grid services. Here, (3-10) and (3-11) limits the total power that can be used to charge or discharge the battery. Also,  $u_t^B$ , a binary variable, which ensures that charging and discharging does not occur simultaneously as shown in (3-10) and (3-11). The state of charge (SOC) of the battery is measured with coulomb counting as given by (3-12). The maximum and minimum SOC ranges are given to prevent overcharge and over-discharge in (3-13). Moreover, SHEMS opts to charge the battery completely at the end of the day as given by (3-14).

The residential battery is modeled according to the specification of Tesla Powerwall 2 [28]. The battery is rated at 270Ah with a nominal voltage rating of 50V, giving the 13.5kW total power. The charge and discharge power are limited to 5kW as per the specifications. The battery is considered fully charged at the start of the day with 100% initial SOC.

### 3.2.1.3.2 Electric Vehicle Load

The electric vehicle is modeled as a mobile battery energy storage system, which can provide power to other residential loads and the grid if necessary. However, the model of EV is designed with a condition that at the end of the day, the battery is fully charged, giving full range to the next day's drive. Also, since this is a mobile load, availability for interaction with the energy management system was included in the model. Two variables  $T_d$  and  $T_a$  defines when the battery leaves and arrives at the residence respectively. The EV is available to the system between the period  $T_a$  and  $T_d$ . The model is explained by (3-15) to (3-20).

$$P_t^{EVu} + P_t^{EVs} = \eta_{dch}^{EV} P_t^{EVdch} \quad , \forall t \in [T_a, T_d] \quad (3-15)$$

$$0 \leq P_t^{EVdch} \leq R_{max}^{EVdch} (1 - u_t^{EV}) \quad , \forall t \in [T_a, T_d] \quad (3-16)$$

$$0 \leq P_t^{EVch} \leq R_{max}^{EVch} (u_t^{EV}) \quad , \forall t \in [T_a, T_d] \quad (3-17)$$

$$SOC_{t+1}^{EV} = SOC_t^{EV} + \frac{\Delta t \cdot (\eta_{ch}^{EV} I_{ch} - \eta_{dch}^{EV} I_{dch})}{100Cap} \quad , \forall t \in [T_a, T_d] \quad (3-18)$$

$$SOC_t^{EVmin} \leq SOC_t^{EV} \leq SOC_t^{EVmax} \quad , \forall t \in [T_a, T_d] \quad (3-19)$$

$$SOC_t^{EV} = SOC_t^{EVmax} \quad , t = T_d \quad (3-20)$$

The model for the EV is identical to battery energy storage in the residence. It is considered that the EV battery is rated at 16kW. This battery can be discharged to a minimum of 4.8kW, while the battery returns to the residence with 8kW. The charging and discharging rate of the EV were fixed at 3.3kW.



### 3.2.1.4 Thermostatically Controlled Loads

Thermostatically controlled load models are air conditioner and electric water heater,  $L_T = \{AC, EWH\}$ . The model output is temperature, guided by constraints and user-defined temperature ranges. The model for the HVAC system is explained with (3-21) to (3-23).

$$T_t^{in} = \left(1 - \frac{\Delta t}{100M_a C_a R^{eq}}\right) T_{t-1}^{in} + \frac{\Delta t}{100M_a C_a R^{eq}} \cdot T_t^{out} + \frac{COP \cdot P_{AC} \Delta t}{2.77 \times 10^{-4} M_a C_a} \cdot u_t^{AC}, \forall t \quad (3-21)$$

$$T_t^{lb} \leq T_t^{in} \leq T_t^{ub}, \forall t \quad (3-22)$$

$$P_t^{AC} = P_{AC} \cdot u_t^{AC}, \forall t \quad (3-23)$$

In (3-21), the internal temperature of the residence at time  $t$  is generated from the air mass,  $M_a$ , thermal capacitance,  $C_a$ , equal thermal resistance,  $R^{eq}$ , performance coefficient,  $COP$ , AC rated power,  $P_{AC}$ , and external temperature,  $T_t^{out}$ . The values of these parameters are obtained from [29]. The constraint (3-22) shows the user preferred lower,  $T_t^{lb}$ , and upper,  $T_t^{ub}$  bound of the temperature. Finally, the total power consumed by the HVAC is given by (3-23). The rated power for the HVAC was 2kW.

The electric water heater is modeled similar to the HVAC system. The major difference is that the temperature of the hot water is dependent on the hot water usage pattern of the resident. The expressions (3-24) to (3-26) is utilized to define the electric water heater.

$$T_t^{EWH} = T_{t-1}^{EWH} + (\alpha \cdot u_t^{EWH} - \beta \cdot HWU_t - \gamma)\Delta t \quad , \forall t \quad (3-24)$$

$$T_t^{EWH,lb} \leq T_t^{EWH} \leq T_t^{EWH,ub} \quad , \forall t \quad (3-25)$$

$$P_t^{EWH} = P_{EWH} \cdot u_t^{EWH} \quad , \forall t \quad (3-26)$$

The hot water temperature at time  $t$  is a function of the hot water usage,  $HWU_t$ . A common hot water usage pattern for residential users was obtained from [30] as shown in Figure 3.2. Here, (3-24) is the temperature limit constraints according to user preferences. Total power is obtained from (3-26). The rater maximum power for the electric water heater was 4kW.

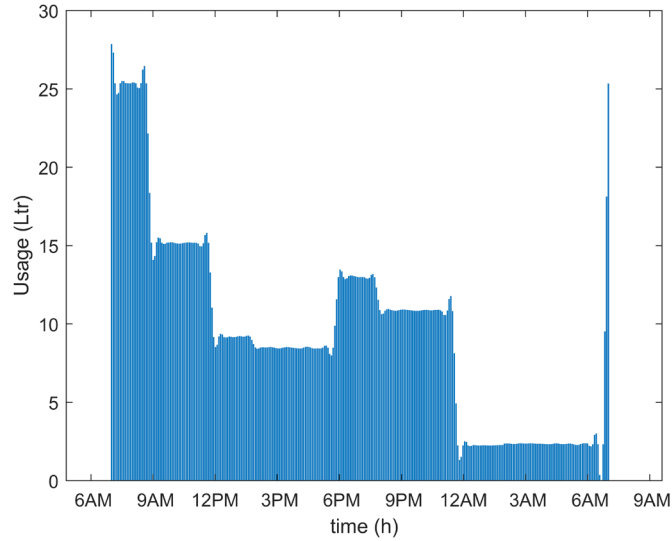


Figure 3.2. Hot water usage pattern in a residence [30].

### 3.2.2 PV Generation Model

The SHESM is considered to be equipped with PV solar panels with MPPT, that can produce maximum energy, limited by the solar power production capacity. The PV is the

local power source besides the power from the grid that can either resource the residential load or sell power back to the grid. Here, (3-27) calculates the total solar power production capacity, giving the total power produced by the PV panels as shown in (3-28). The efficiency,  $\eta_2$ , and area of the PV panel A is considered to be 0.2 and 45m<sup>2</sup> respectively. The other restrictions ensure the PV power is either used for residential loads or sold to the grid.

$$P_t^{SC} = \eta_2 S_t A (1 - 0.005(T_t^{out} - 25)) \quad , \forall t \quad (3-27)$$

$$0 \leq P_t^{PVPro} \leq P_t^{SC} \quad , \forall t \quad (3-28)$$

$$P_t^{PVu} + P_t^{PVs} = P_t^{PVPro} \quad , \forall t \quad (3-29)$$

$$\begin{cases} 0 \leq P_t^{PVu} \\ 0 \leq P_t^{PVs} \end{cases} \quad , \forall t \quad (3-30)$$

### 3.2.3 Problem Formulation

Since load models contain both continuous and discrete variables, the problem is set up as mixed-integer linear programming (MILP). The MILP problem is formulated with (3-31) to (3-35). The objective function is given in (3-31), designed to minimize the electricity cost of the residence. The total power sold back to the grid is given by (3-32), which is the sum of all the power sold by PV, EV and battery. The balancing equation (3-33), is subject to (3-34) to (3-36) and previously explained constraints. Here, (3-34) enforces that the total load is non-negative, whereas (3-35) and (3-36) ensures the residence is not performing grid services and consuming electricity from the grid simultaneously.

$$\text{minimize } \sum_{t=1}^T (P_t^{Gr} - P_t^S) C_t^P \Delta t \quad , \forall t \quad (3-31)$$

$$P_t^S = P_t^{PVs} + P_t^{EVs} + P_t^{Bs} \quad , \forall t \quad (3-32)$$

$$P_t^{Gr} + P_t^{PVu} + P_t^{EVu} + P_t^{Bu} = \sum_{i \in L_I} P_t^{i,ch} + \sum_{i \in L_U} P_t^i + \sum_{i \in L_T} P_t^i + P_t^I \quad , \forall t \quad (3-33)$$

$$0 \leq \sum_{i \in L_I} P_t^{i,ch} + \sum_{i \in L_U} P_t^i + \sum_{i \in L_T} P_t^i + P_t^I \leq PL_t \quad , \forall t \quad (3-34)$$

$$0 \leq P_t^S \leq P_t^{sub} (1 - u_t^{Gr}) \quad , \forall t \quad (3-35)$$

$$0 \leq P_t^{Gr} \leq P_t^{Grub} u_t^{Gr} \quad , \forall t \quad (3-36)$$

The day ahead real-time (RT) electricity price used for billing is used as the price of electricity in (3-31). A common residential day ahead RT price profile as seen in Figure 3.3 was used to formulate the problem.

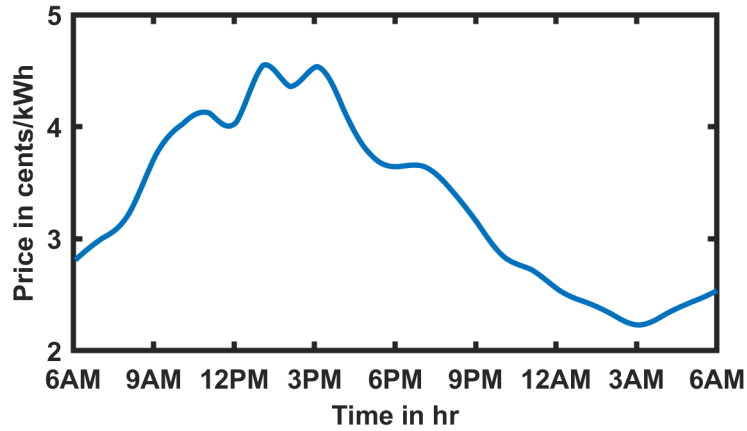


Figure 3.3. The utilized day ahead RT price profile.

This SHEMS model is generated in MATLAB 2018 environment. The SHEMS model is developed with the YALMIP tool, which is used as an algebraic modeling language (AML) to solve the MILP problem. The grid power consumed by the residence, total PV power produced, and load profiles obtained from the SHEMS problem for an optimized condition are most important in this analysis. These quantities are used to determine the battery degradation using Bayesian Networks.

### **3.3 Hierarchical Bayesian Network for Battery Degradation Estimation**

Bayesian Network is a probabilistic method of representing a process through a direct acyclic graph (DAG) and parameters to determine a joint probability distribution of network random variables. The DAG constitutes of nodes and edges. These nodes are random variables, connected to parent through edges. BN can classify the variables according to several properties. In this problem, the variables are either observations or unobserved variables. Observations are measurements, a single instance of a stochastic process. Unobserved variables are modeled as random variables because their characteristics are controlled by a probability distribution. Thus, unobserved variables are characterized by a probability distribution. According to Bayes' theorem, the probability distribution of an unobserved variable,  $X$ , conditional of the observation,  $Y$ , known as the posterior distribution,  $P(X|Y)$ , is given in (3-37), where observations and unobserved variables are vectors [31]. Here, (3-37) gives the probability of unobserved random variable  $X$ , given than observation  $Y$  is available.

$$P(X|Y) = P(Y|X)P(X)/P(Y) \quad (3-37)$$

$$P(Y) = \int P(Y|X) P(X) dX \quad (3-38)$$

Here,  $P(Y|X)$  is known as likelihood,  $P(X)$  is prior and  $P(Y)$  is marginal distribution. Marginal distribution can be determined analytically using (3-38). BN satisfies Markov condition, which requires that every variable is independent of the effect of non-descendants [32]. Therefore, this problem is solved with Markov Chain Monte Carlo (MCMC) sampling.

The factors influencing battery degradation or capacity fade, in this case, are temperature, SOC, C-rate and ampere-hour throughput. Except for the temperature, all other variables are the function of daily operations of the battery and user preferences, all highly stochastic processes. Moreover, SOC and amp-hour throughput are conditional on C-rate, while C-rate is conditional on battery power itself. Thus, hierarchal BN is appropriate to evaluate battery capacity fade.

### 3.3.1 Network Development

The proposed detailed hierarchical Bayesian Network can be seen in Figure 3.4. The following parts will divulge the details of forming this BN. The first step when developing BN is to define the variables with nodes and interdependencies with arrows. The measurement of the capacity fade percentage of a battery cell contains errors, in terms of measurement and the process. The errors give rise to uncertainty. So, the estimation of capacity fade percentage is considered with errors. The estimation has a probabilistic

relation with actual measurement. The probabilistic nature of capacity fade estimation allows for consideration of operational variation that cannot be achieved by any deterministic model generated from lab-based experiments.

Moving down the network in Figure 3.4, a top tier node has a subsequent node only when higher tier variables is dependent on the lower tier variable. For example, the capacity fade estimation has a probabilistic relationship with total amp-hour throughput, C-rate, average state of charge, and temperature estimations [13], [33], [34]. This probabilistic relation aids in considering the variations in subsequent nodes down the network. Here it was considered that the battery would face the internal temperature of the residence. Most batteries are either equipped with thermal management units or, placed inside the residence. Further down the network in Figure 3.4, it can be seen that Ah and SOC has a conditional dependency on  $I_c$  as both the amp-hour throughput and average state of charge is a function of the battery current. The C-rate is a method of measuring the battery current without the limitation of the battery capacity.

The C-rate enables the possibility of relating the power of the battery by considering the voltage. The battery power is obtained from an aggregated average function consisting of several contributing factors. These contributing factors are associated with their respective powers in the residential power pool which has a possibility of contributing towards the capacity fade of the battery. The solar PV power generation has a probabilistic relation to battery power. Solar PV generation is highly susceptible to the change of ambient conditions, which can be explained properly by a probabilistic relationship.

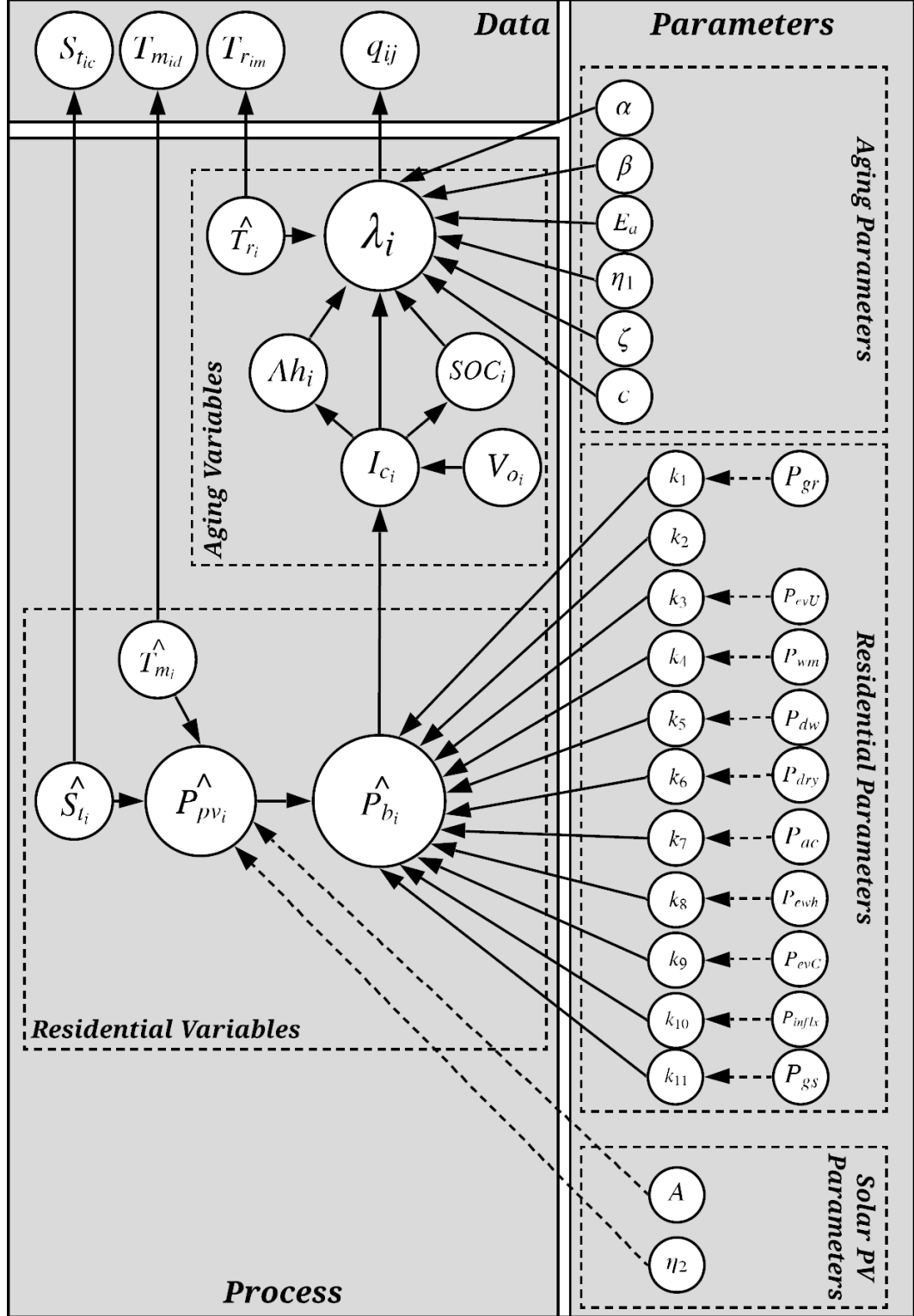


Figure 3.4. Developed BN for estimating degradation for residential battery energy storage systems.



Except for PV, other components in the power pool are considered to have a deterministic connection to their respective contribution factors. Like the capacity fade, the temperature and solar irradiations are related to their respective measurement probabilistically. The aging and PV solar parameters explain the relationships of capacity fade and PV power estimation to their subsequent variables.

The BN in Figure 3.4, developed with these random variables, observation data, and parameters, has three parts to it. First is data, containing the measurements, then the process based on the conditional dependencies and lastly the parameters. The process section contains both aging and residential variables. The solid lines represent probabilistic dependency whereas the dashed lines are for deterministic properties. In this problem, there are,  $i = 1, \dots, N$ , the number of observations. Each observation contains multiple measurements. Here, J, M, D and C number of measurements are taken at each observation for,  $q_{ij}$ ,  $T_{rim}$ ,  $T_{mid}$ , and  $S_{tic}$  respectively.

### 3.3.2 Mathematical Expressions

The mathematical expression from the network, are derived considering all the variables, data and parameters can be observed in (3-39). Equation (3-40) to (3-43) are associated functions used in (3-39). The equation are formed by using the previously explained Bayes' rule. Probabilities are denoted with, "[ ]", unobserved variables are presented on the left of, "|", observed variables to the right. Since the marginal distribution is ignored, " $\propto$ " is used instead of equality. To solve this problem through MCMC 10,000 samples of the posterior are taken. These samples are estimated through distribution fitting.

Thus, the probability distribution function (PDF) of each variable is based on their properties.

In this system,  $q, \lambda, Ah, V_o, \widehat{P}_{pv}, \widehat{S}_t, I_c$  and all the parameters must be greater or equal to zero, thus gamma PDF represents these variables. A beta PDF is appropriate for this *SOC* as it has a range from 0 to 1. A normal PDF describes both the temperatures and battery power, as these are real numbers. The final step in the mathematical formulation is forming full conditionals to apply MCMC. Full conditional equations for  $\lambda, \widehat{T}_m, \widehat{T}_r, \widehat{P}_{pv}, \widehat{S}_t$  and  $I_c$  are given in (4-44) to (4-54). Here,  $[\lambda | \cdot]$  defines the conditional dependence of capacity fade with all the associated variables. Also, G, B, and N refer to the type of distribution used to explain a specific variable.

$$\begin{aligned}
& \left[ \lambda, \widehat{T}_r, Ah, SOC, I_c, V_o, \widehat{P}_b, k_1, \dots, k_{11}, \widehat{P}_{pv}, \widehat{S}_t, \widehat{T}_m, \alpha, \beta, E_a, \eta, \zeta, \epsilon, A, \eta_2 \right] \\
& \quad | q, T_r, T_m, S_t \\
& \propto \prod_{i=1}^N \prod_{j=1}^J [q_{ij} | \lambda_i] [\lambda_i | F_i] \prod_{m=1}^M [T_{rim} | \widehat{T}_r] [\widehat{T}_r] [Ah_i | I_{ci}] [SOC_i | I_{ci}] \\
& \quad \times [I_{ci} | Y_i] [V_{oi}] [\widehat{P}_{bi} | G_i] [\widehat{P}_{pv_i} | H_i] \prod_{c=1}^C [S_{tic} | \widehat{S}_t] [\widehat{S}_t] \prod_{d=1}^D [T_{mid} | \widehat{T}_m] [\widehat{T}_m] \\
& \quad \times [\alpha] [\beta] [E_a] [\eta_1] [\zeta] [\epsilon] [k_{1_i}] \dots [k_{11_i}] [A] [\eta_2]
\end{aligned} \tag{3-39}$$

$$F_i = (\alpha SOC_i + \beta) e^{-(E_a - \eta_1 I_{ci}) / R \widehat{T}_r} \times Ah_i^\zeta + \epsilon \tag{3-40}$$

$$\begin{aligned}
G_i = & k_{1_i} P_{gr} + k_{2_i} \widehat{P}_{pv_i} + k_{3_i} P_{evU} + k_{4_i} P_{wm} + k_{5_i} P_{dw} + k_{6_i} P_{dry} + k_{7_i} P_{ac} \\
& + k_{8_i} P_{ewh} + k_{9_i} P_{evC} + k_{10_i} P_I + k_{11_i} P_{gs}
\end{aligned} \tag{3-41}$$

$$Y_i = \widehat{P}_{b_i}/V_{o_i} \quad (3-42)$$

$$H_i = \eta_2 \widehat{S}_{t_i} A \left( 1 - 0.005 (\widehat{T}_{m_i} - 298) \right) \quad (3-43)$$

$$[\lambda | \cdot] \propto \prod_{i=1}^N \prod_{j=1}^J \mathbf{G}[q_{ij} | \lambda_i] \mathbf{G}[\lambda_i | F_i] \quad (3-44)$$

$$[\widehat{T}_m | \cdot] \propto \prod_{i=1}^N \mathbf{G}[\widehat{P}_{pv_i} | H_i] \mathbf{N}[\widehat{T}_{m_i}] \prod_{d=1}^D \mathbf{N}[T_{m_{id}} | \widehat{T}_{m_i}] \quad (3-45)$$

$$[\widehat{P}_{pv} | \cdot] \propto \prod_{i=1}^N \mathbf{N}[\widehat{P}_{b_i} | G_i] \mathbf{G}[\widehat{P}_{pv_i} | H_i] \quad (3-46)$$

$$[\widehat{S}_t | \cdot] \propto \prod_{i=1}^N \mathbf{G}[\widehat{P}_{pv_i} | H_i] \mathbf{G}[\widehat{S}_{t_i}] \prod_{c=1}^C \mathbf{G}[S_{t_{ic}} | \widehat{S}_{t_i}] \quad (3-47)$$

$$[I_C | \cdot] \propto \prod_{i=1}^N \mathbf{G}[\lambda_i | F_i] \mathbf{G}[I_{c_i} | Y_i] \mathbf{G}[Ah_i | I_{c_i}] \mathbf{B}[SOC_i | I_{c_i}] \quad (3-48)$$

$$[\widehat{P}_b | \cdot] \propto \prod_{i=1}^N [\widehat{P}_{b_i} | G_i] \times [I_{c_i} | Y_i] \quad (3-49)$$

$$[V_o | \cdot] \propto \prod_{i=1}^N [I_{c_i} | Y_i] \times [V_{o_i}] \quad (3-50)$$

$$[k_n | \cdot] \propto \prod_{i=1}^N [\widehat{P}_{b_i} | G_i] \times [k_{n_i}] \quad ; n = 1, 2, 3 \dots \dots, 11 \quad (3-51)$$

$$[\widehat{T}_r | \cdot] \propto \prod_{i=1}^N \mathbf{G}[\lambda_i | F_i] \times \mathbf{N}[\widehat{T}_{r_i}] \times \prod_{m=1}^M \mathbf{N}[T_{rim} | \widehat{T}_{r_i}] \quad (3-52)$$

$$[Ah | \cdot] \propto \prod_{i=1}^N [\lambda_i | F_i] \times [Ah_i | I_{c_i}] \quad (3-53)$$

$$[SOC | \cdot] \propto \prod_{i=1}^N [\lambda_i | F_i] \times [SOC_i | I_{c_i}] \quad (3-54)$$

The MCMC solving process starts with an initial value  $v^{(1)}$ , for all variables and parameters. These initial values are calculated deterministically from observations. At any given iteration, a proposal value  $v^{(P)}$ , is proposed based on the current value and distribution properties of the variable given by (3-55). The standard deviation of the proposal should be smaller or equal to the priors to ensure successful sampling. Metropolis-Hasting criteria in (3-56) determine which sample of the posterior to keep.

$$v^{(*)} \sim N(v^{(r)}, \sigma_t) \quad (3-55)$$

$$R = \min \left( 1, \frac{[v^{(P)} | \cdot]}{[v^{(r)} | \cdot]} \times \frac{[v^{(r)} | v^{(P)}]}{[v^{(P)} | v^{(r)}]} \right) \quad (3-56)$$

In the problem under discussion, the initial values are calculated from SHEMS simulation results, i.e.  $\widehat{T}, \widehat{P}_{pv}, \widehat{S}_t$ . Initial values of aging parameters differ according to the

type of battery chemistry. Thus, different researchers present various values. For this problem, multiple sources [34]–[36] are used to obtain the appropriate initial values of aging parameters. The contribution coefficients are initiated based on the residential source and loads contribution towards battery degradation and their probability of charging and discharging. The initial value of battery power estimation is obtained from (3-41), whereas the initial value of capacity fade estimation is from (3-40). Battery voltage is initiated with the nominal voltage of a TESLA Power Wall 2. The other variables,  $\lambda$ ,  $Ah$ ,  $SOC$  and  $I_c$  are initiated with a calculation based on battery power and voltage initial values.

### 3.3.3 Training and Evaluation of BN through Testing

The modeled BN was trained with experimental results of A123 ANR26650, 2.3Ah, lithium-iron-phosphate (LFP) cells, obtained from [35]. Groot et al. [35] performed multiple time and frequency based experiments with several sets of ANR26650 in order to generate a detailed deterministic battery model. Results of capacity fade, SOC and temperature were obtained from 1C rate tests that are used to train the BN model. ANR26650 are the most popular for residential or vehicular application for their extensive safety features. The purpose of training the BN is to obtain the PDF of parameters  $\alpha, \beta, E_a, \eta, \zeta$ , accounting for the uncertainty in the measurement of data and process. To train the model, 80% of the data were randomly selected, the rest were kept for testing the model.

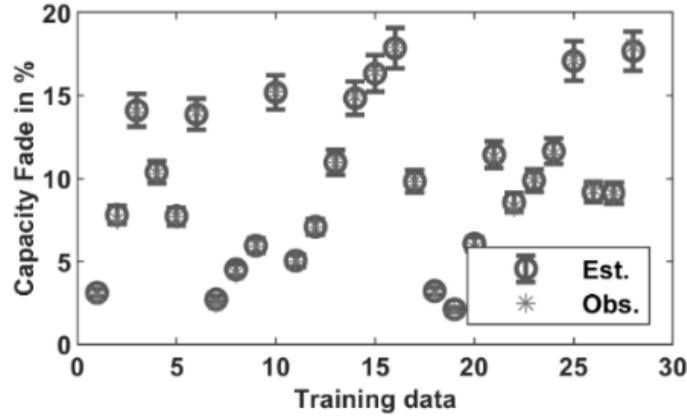


Figure 3.5. Training of modeled Bayesian Network.

The accuracy of the training procedure can be seen in the error bar plot Figure 3.5. In Figure 3.5, the mean of the PDF for  $\lambda$ , and error bar with twice the standard deviation is plotted along with respective observations. The purpose of testing is to observe if the trained BN can predict the remaining 20% data. Figure 3.6 shows a similar plot where the remaining observations are estimated with obtained parameters.

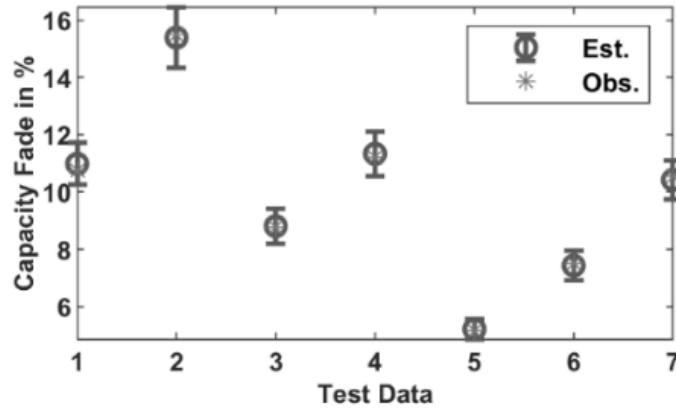


Figure 3.6. Testing of modeled Bayesian Network.

The normalized root mean square difference percentage (NRMSDP) between the mean of PDF and its observations are determined for the aging variables. NRMSDP for

both testing and training phase are in Table 3.2. The smaller value of error and high accuracy of fitting for the aging variable validates the success of the training process.

**Table 3.2. NRMSDP Values from Training and Testing**

<b>Variables</b>	<b>Training</b>	<b>Testing</b>
Capacity Fade, $\lambda$	1.79%	1.28%
Ah Throughput, $Ah$	1.35%	1.07%
State of Charge, $SOC$	0.82%	0.30%
Temperature, $T$	0.16%	0.07%
C-rates, $I_c$	0.98%	0.78%

The results of the optimization problem are used as an input to the BN model. The power requirements of the residential loads while being optimized is used as an input to the BN. These variables are part of the residential parameter sections of Figure 3.4.

### **3.4 Case Study: Evaluate Degradation of The Battery**

In the case study section, first, the effect of grid services performed by the SHEMS on battery capacity is explored. Second, the capacity fade due to varying EV schedule is shown. Lastly, capacity fade due to changing weather, in terms of ambient temperature and solar irradiation due to variation in location is discussed. Capacity fade is evaluated for a service life of ten years.

#### **3.4.1 Effect of Grid Services on Capacity Fade**

This case consists of two identical scenarios. In both scenarios, power consumption from the grid,  $P_t^{Gr}$ , was limited to 5.5kW. The EV leaves the residence at 7 am and comes back at 5 pm, with 50% SOC remaining. Real-time utility (RTU) price structure was used [3]. The solar irradiance and ambient temperature for both cases remained exactly the same.

The major difference was the energy management system could perform grid services in the second scenario. The capacity fade PDFs can be seen in Figure 3.7 for both scenarios. It can be seen here that the capacity fade of the battery is higher when grid services are not performed. The center of the distribution when the grid services are performed is about 9.29%, whereas for not performing grid services the value goes up to 12.14%.

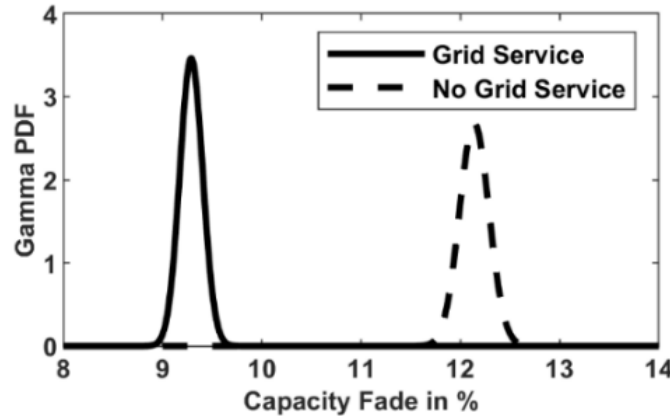


Figure 3.7. Effect of grid services on the capacity fade.

This higher aging is caused by the presence of the solar PV system. When the SHEMS is prevented from performing grid services, the objective function focusing on reducing electricity bill increases self-consumption from the renewable source. The power from the PV is stored in the battery and discharged to loads as per requirement. Reducing the power intake from the grid leads to a reduction in the overall electricity bill. The battery Ah-throughput increases to 30.5kAh from 21.55kAh when grid services are not performed.

It can be further confirmed by observing the distributions of the PV power used for charging the battery for each case in Figure 3.8. It is obtained from the distribution of power contributed towards battery capacity fade from the PV,  $k_{2i}\widehat{P_{pv_i}}$ . It can be seen, not



performing grid services causes the solar PV to charge the battery with a higher power to increase self-consumption.

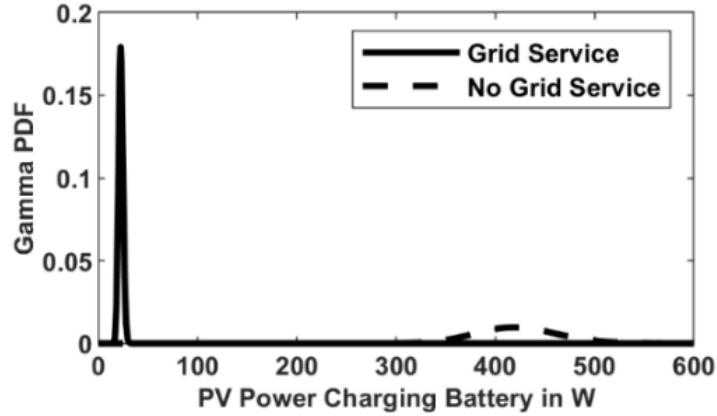


Figure 3.8. An increase in PV power used to charge the battery.

### 3.4.2 Effect of EV Schedule on Capacity Fade

This case deals with changing the schedule of the EV. Initially, it was assumed that the EV is absent during the first 10 hours of the day and comes back with 50% SOC remaining. A set of 4 scenarios were created to represent the effect of EV schedule on the capacity fade. This set considers that EV departs the house at a random time, from 7 am to 10 am, while returning at 5 pm. Other parameters of SHEMS remained like the base case with no grid services being performed. The battery has a higher capacity fade with the delayed departure of EV from the residence. If the EV is available longer in the power pool of the residence, it has a higher probability to either charge or discharge from the battery. This excess cycling of the battery caused by the presence of the EV causes a higher capacity fade. The PDFs of the capacity fade can be observed in Figure 3.9.

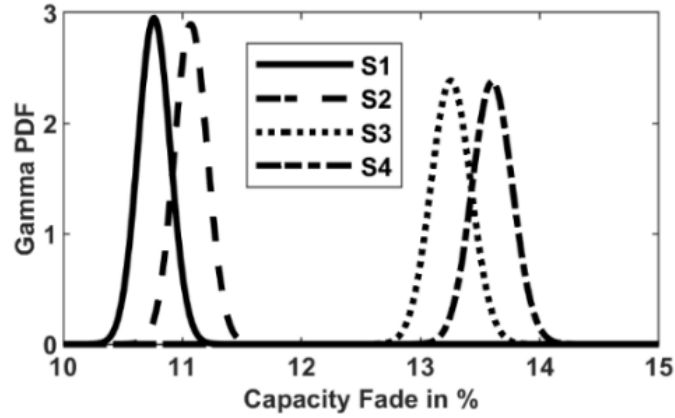


Figure 3.9. Effect of EV schedule on capacity fade.

The center of the PDF is increasing with a delayed departure in Figure 3.10. The mean of capacity fade can change almost 3% with delayed departure. It can be further confirmed that the battery has higher Ah cycling due to the presence of the EV. It shows that with delayed departure the battery has more Ah being cycled through it, subsequently producing a higher capacity fade. The Ah throughput can be reduced by 42% if the EV departs the residence earlier, reducing the capacity fade by almost 3%.

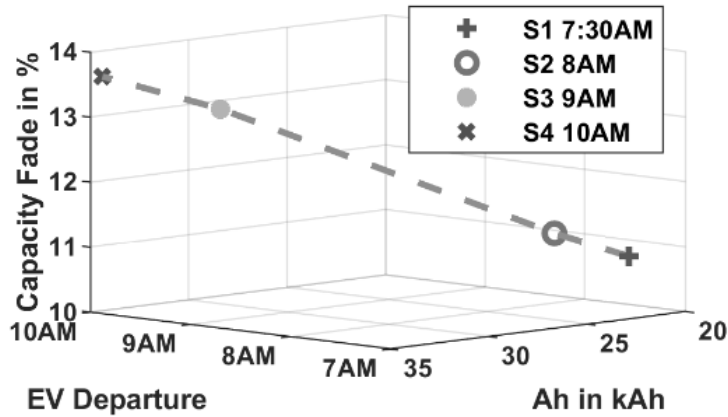


Figure 3.10. Capacity fade increases with EV departure time and Ah.

### 3.4.3 Impact of Weather and Location on Capacity Fade

The location of the residence has a major effect on the capacity fade of the battery. The change in location affects ambient temperature and solar irradiation. The power drawn by the HVAC is directly related to the ambient temperature. HVAC acts as a load to the battery contributing towards the capacity fade. To explore the effect of the temperature change, the hourly temperature data for five different climates, Anchorage (AK), Denver (CO), New York (NY), Los Angeles (LA), Phoenix (AZ) in 2018 were collected. The locations were selected in order of their increasing mean of the normal PDF. The capacity fade was estimated for these locations, keeping other parameters of SHEMS as the base case with no grid services being performed.

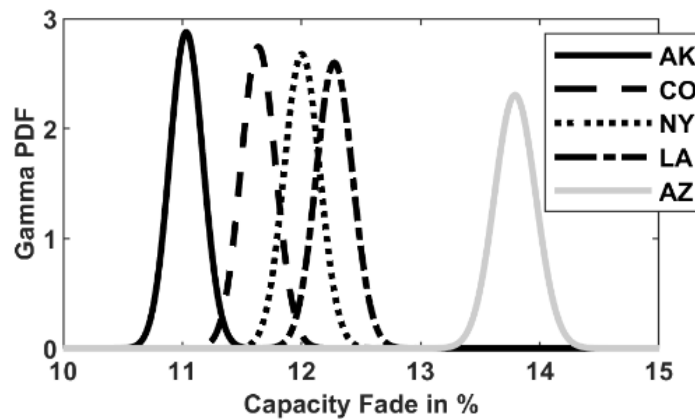


Figure 3.11. Effect of the ambient temperature of various locations on the capacity fade.

These varying normal PDFs of ambient temperature lead to variations in the capacity fade. The capacity fade PDF for variations in ambient temperature can be observed in Figure 3.11. Here the capacity fade ranges from 11% to 14%. It is evident that Anchorage has the lowest capacity fade contributed by a temperature distribution with the lowest

mean. Whereas, Phoenix has the highest capacity fade, caused by a temperature PDF with a much higher mean.

Increased capacity fade with increasing temperature, even though the battery remains inside the residence or under controlled thermal conditions, can be explained with the PDF of the Ah throughput. Figure 3.12 shows the PDF of the Ah throughput of the battery. With higher ambient temperature the Ah throughput is higher. It is because, at higher ambient temperature, the HVAC requires more power to maintain the internal temperature of the residence in accordance with the user's preference. This higher power requirement causes increased load on the battery. Thus, increasing the capacity fade in the process.

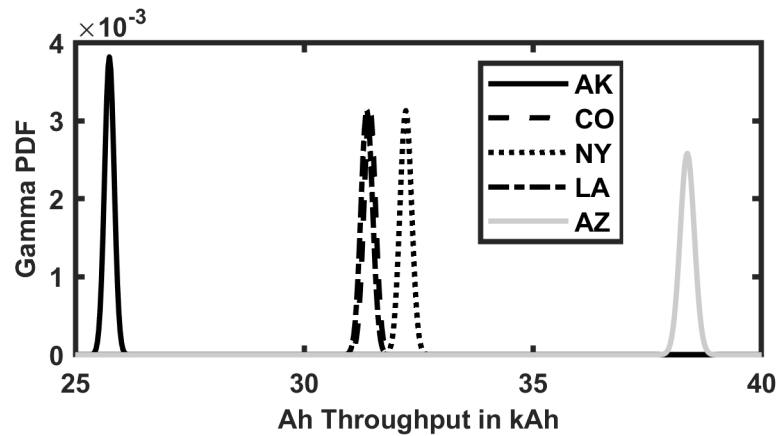


Figure 3.12. Increase in the Ah throughput for higher ambient temperature.

The solar irradiation is more abundant as the SHEMS moves from Anchorage to Phoenix. This results in higher power generation from solar PV in Phoenix as opposed to Anchorage. This higher PV power production leads to a significant increase in self-consumption, as no grid services were being performed while exploring the effect of changed solar irradiation. A significantly large portion of PV power generated is used to charge the battery when higher solar irradiation is available. The contribution coefficient

of PV power towards the capacity fade increases with abundant solar irradiation, as seen in Figure 3.13. This higher contribution from the PV power causes the capacity fade to increase. Figure 3.14 shows the effect of solar irradiation on the capacity fade, ranging from 9% to 14%.

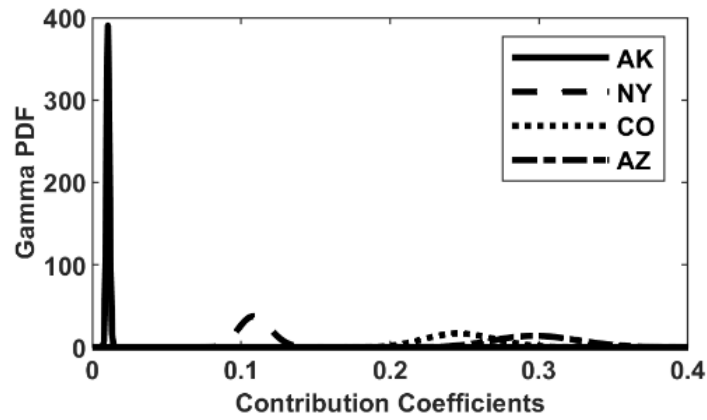


Figure 3.13. Increase in contribution to capacity fade for increased solar irradiance.

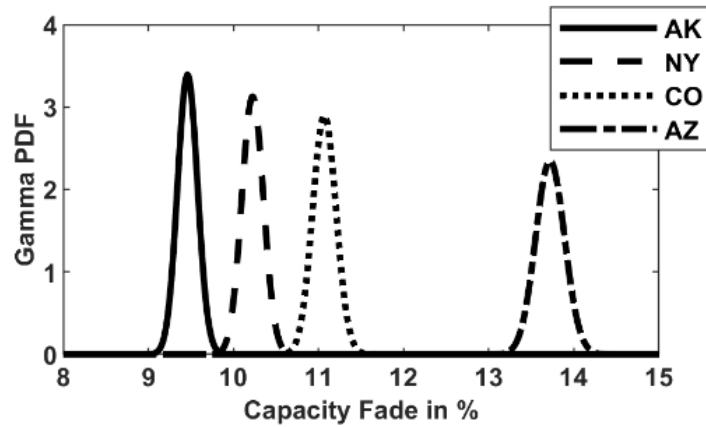


Figure 3.14. Effect of capacity fade for increased solar irradiance

It is evident that higher solar irradiation leads to significantly higher capacity fade for the battery. Anchorage has the lowest capacity fade as it is associated with the lowest

average yearly solar irradiance. Whereas, Phoenix has the highest capacity fade brought about by the abundant solar irradiance available.

### **3.5 Conclusion**

A smart home energy management system simulation is utilized to provide the initial values and priors for BN. These results are used to design a BN for residential battery energy storage. The BN relates batteries' immediate variables to external variables, i.e. solar irradiation, ambient temperature.

Afterward, the capability of the BN was exercised with multiple case scenarios. These case scenarios revealed some interesting results. It was revealed that utilizing the residential battery for grid services causes a reduction in the capacity fade of the battery, as the battery will not be charged more often from the PV panel. Moreover, the capacity fade was increased with a longer presence of EV at the residence. Though the battery was not subject to the ambient temperature directly, the capacity fade was higher for higher temperature climates. Finally, increased solar irradiance resulted in a higher capacity fade.

The overall results reveal that a probabilistic approach of evaluation of battery capacity fade through hierarchical BN is a promising solution in different cycling conditions. The excellence of this method lies in the capability of utilizing real-life load, source and environmental data, relating it probabilistically to account for the real world variations on previously generated experimental priors, through developed BN. Evaluated degradation can be a powerful tool for SHEMS. The optimization can utilize the evaluated battery degradation information in order to adapt to account for aging.

## References

- [1] I. Ranaweera, O.-M. Midtgård, and M. Korpås, “Distributed control scheme for residential battery energy storage units coupled with PV systems,” *Renew. Energy*, vol. 113, pp. 1099–1110, 2017.
- [2] G. Xu, W. Yu, D. Griffith, N. Golmie, and P. Moulema, “Toward Integrating Distributed Energy Resources and Storage Devices in Smart Grid,” *IEEE Internet Things J.*, vol. 4, no. 1, pp. 192–204, 2017.
- [3] A. Savasci, “Grid-Aware Optimal Demand Response Management of Smart Homes,” *MS, Michigan Technol. Univ.*, pp. 43–73, 2018.
- [4] D. Torregrossa and E. Niederhäuser, “Rooftop Photovoltaic Power Plant and Electrochemical Storage: Trend and Perspectives for Residential Buildings,” in *2017 International Symposium on Computer Science and Intelligent Controls (ISCSIC)*, 2017, pp. 33–38.
- [5] J. D. K. Bishop, C. J. Axon, D. Bonilla, M. Tran, D. Banister, and M. D. McCulloch, “Evaluating the impact of V2G services on the degradation of batteries in PHEV and EV,” *Appl. Energy*, vol. 111, pp. 206–218, Nov. 2013.
- [6] J. D. K. Bishop, C. J. Axon, D. Bonilla, and D. Banister, “Estimating the grid payments necessary to compensate additional costs to prospective electric vehicle owners who provide vehicle-to-grid ancillary services,” *Energy*, vol. 94, pp. 715–727, Jan. 2016.
- [7] C. Guenther, B. Schott, W. Hennings, P. Waldowski, and M. A. Danzer, “Model-based investigation of electric vehicle battery aging by means of vehicle-to-grid scenario simulations,” *J. Power Sources*, vol. 239, pp. 604–610, 2013.
- [8] R. Dufo-López, “Optimisation of size and control of grid-connected storage under real-time electricity pricing conditions,” *Appl. Energy*, vol. 140, pp. 395–408, Feb. 2015.
- [9] A. Shcherbakova, A. Kleit, and J. Cho, “The value of energy storage in South Korea’s electricity market: A Hotelling approach,” *Appl. Energy*, vol. 125, pp. 93–102, Jul. 2014.
- [10] W. He, N. Williard, M. Osterman, and M. Pecht, “Prognostics of lithium-ion batteries based on Dempster–Shafer theory and the Bayesian Monte Carlo method,” *J. Power Sources*, vol. 196, no. 23, pp. 10314–10321, Dec. 2011.
- [11] M. Jafari, L. E. Brown, and L. Gauchia, “A Bayesian Framework for EV Battery Capacity Fade Modeling,” in *2018 IEEE Transportation Electrification Conference and Expo (ITEC)*, 2018, pp. 304–308.

- [12] R. Xiong, F. Sun, Z. Chen, and H. He, "A data-driven multi-scale extended Kalman filtering based parameter and state estimation approach of lithium-ion polymer battery in electric vehicles," *Appl. Energy*, vol. 113, pp. 463–476, Jan. 2014.
- [13] X. Qin, Q. Zhao, H. Zhao, W. Feng, and X. Guan, "Prognostics of remaining useful life for lithium-ion batteries based on a feature vector selection and relevance vector machine approach," in *2017 IEEE International Conference on Prognostics and Health Management (ICPHM)*, 2017, pp. 1–6.
- [14] K.-C. Chiu, C.-H. Lin, S.-F. Yeh, Y.-H. Lin, C.-S. Huang, and K.-C. Chen, "Cycle life analysis of series connected lithium-ion batteries with temperature difference," *J. Power Sources*, vol. 263, pp. 75–84, 2014.
- [15] B. Xu, A. Oudalov, A. Ulbig, G. Andersson, and D. S. Kirschen, "Modeling of Lithium-Ion Battery Degradation for Cell Life Assessment," *IEEE Trans. Smart Grid*, vol. 9, no. 2, pp. 1131–1140, 2018.
- [16] J. Remmlinger, M. Buchholz, T. Soczka-Guth, and K. Dietmayer, "On-board state-of-health monitoring of lithium-ion batteries using linear parameter-varying models," *J. Power Sources*, vol. 239, pp. 689–695, 2013.
- [17] N. Omar *et al.*, "Lithium iron phosphate based battery – Assessment of the aging parameters and development of cycle life model," *Appl. Energy*, vol. 113, no. 0, pp. 1575–1585, 2014.
- [18] K. Abdulla *et al.*, "Optimal Operation of Energy Storage Systems Considering Forecasts and Battery Degradation," *IEEE Trans. Smart Grid*, vol. 9, no. 3, pp. 2086–2096, 2018.
- [19] K. Worthmann, C. M. Kellett, P. Braun, L. Grüne, and S. R. Weller, "Distributed and Decentralized Control of Residential Energy Systems Incorporating Battery Storage," *IEEE Trans. Smart Grid*, vol. 6, no. 4, pp. 1914–1923, 2015.
- [20] Y. Wang, X. Lin, and M. Pedram, "A Near-Optimal Model-Based Control Algorithm for Households Equipped With Residential Photovoltaic Power Generation and Energy Storage Systems," *IEEE Trans. Sustain. Energy*, vol. 7, no. 1, pp. 77–86, 2016.
- [21] R. Atia and N. Yamada, "Sizing and Analysis of Renewable Energy and Battery Systems in Residential Microgrids," *IEEE Trans. Smart Grid*, vol. 7, no. 3, pp. 1204–1213, 2016.
- [22] A. Mamun, I. Narayanan, D. Wang, A. Sivasubramaniam, and H. K. Fathy, "A Stochastic Optimal Control Approach for Exploring Tradeoffs between Cost Savings and Battery Aging in Datacenter Demand Response," *IEEE Trans.*



- Control Syst. Technol.*, vol. 26, no. 1, pp. 360–367, 2018.
- [23] J. Cai, H. Zhang, and X. Jin, “Aging-aware predictive control of PV-battery assets in buildings,” *Appl. Energy*, vol. 236, pp. 478–488, Feb. 2019.
  - [24] Y. Riffonneau, S. Bacha, F. Barruel, and S. Ploix, “Optimal Power Flow Management for Grid Connected PV Systems With Batteries,” *IEEE Trans. Sustain. Energy*, vol. 2, no. 3, pp. 309–320, 2011.
  - [25] B. Zhou *et al.*, “Smart home energy management systems: Concept, configurations, and scheduling strategies,” *Renew. Sustain. Energy Rev.*, vol. 61, pp. 30–40, Aug. 2016.
  - [26] P. Zhang, F. Li, and N. Bhatt, “Next-Generation Monitoring, Analysis, and Control for the Future Smart Control Center,” *IEEE Trans. Smart Grid*, vol. 1, no. 2, pp. 186–192, Sep. 2010.
  - [27] M. Rastegar, M. Fotuhi-Firuzabad, and F. Aminifar, “Load commitment in a smart home,” *Appl. Energy*, vol. 96, pp. 45–54, 2012.
  - [28] Tesla, “Tesla Powerwall Specification Sheet.”
  - [29] N. G. Paterakis, O. Erdinç, A. G. Bakirtzis, and J. P. S. Catalão, “Optimal household appliances scheduling under day-ahead pricing and load-shaping demand response strategies,” *IEEE Trans. Ind. Informatics*, vol. 11, no. 6, pp. 1509–1519, Dec. 2015.
  - [30] M. C. Bozchalui, “Optimal Operation of Energy Hubs in the Context of Smart Grids.”
  - [31] N. T. Hobbs and M. B. Hooten, *Bayesian models: a statistical primer for ecologists*. Princeton University Press, 2015.
  - [32] J. Pearl, *Probabilistic reasoning in intelligent systems : networks of plausible inference*. Morgan Kaufmann Publishers, 1988.
  - [33] Y. Zhang, C. Y. Wang, and X. Tang, “Cycling degradation of an automotive LiFePO<sub>4</sub> lithium-ion battery,” *J. Power Sources*, vol. 196, no. 3, pp. 1513–1520, 2011.
  - [34] G. Suri and S. Onori, “A control-oriented cycle-life model for hybrid electric vehicle lithium-ion batteries,” *Energy*, vol. 96, pp. 644–653, 2016.
  - [35] J. Groot, “State-of-health estimation of Li-ion batteries: cycle life test methods,” *Ph.D., CHALMERS Univ. Technol.*, p. 138, 2012.

- [36] J. Wang *et al.*, “Cycle-life model for graphite-LiFePO<sub>4</sub> cells,” *J. Power Sources*, vol. 196, no. 8, pp. 3942–3948, 2011.

## Chapter 4

# Low-cost Hardware-in-the-Loop Lithium-Ion Battery Degradation System for Residential Energy Storage

### **Abstract**

Residential energy storage systems are utilizing Li-ion batteries due to longer service life and lower maintenance. However, the degradation of Li-ion batteries causes loss of capacity and loss of power. This aging phenomenon needs to be characterized by residential energy storage systems to ensure reliable service. In this chapter, a low-cost hardware-in-the-loop (HIL) system is developed to perform aging tests on a Li-ion battery. The HIL utilizes residential loads simulation and a Raspberry Pi 3 based hardware. Raspberry-Pi communicates and controls the peripheral devices to cycle the battery according to the residential load profile obtained from the simulation. The initial test results reveal that the low-cost hardware is capable of cycling the battery according to the load profiles with considerable accuracy.

## 4.1 Introduction

Degradation of Li-ion batteries needs to be validated, irrespective of how it is incorporated in studies involving residential applications. The most common methods for such validation are hardware-in-the-loop (HIL) simulation. HIL mostly popular for prototyping and system modeling for avionics is slowly emerging in battery degradation studies [1]–[3]. HIL enables the use of actual hardware, which is of research interest, simulating the rest of the system. This ensures that the battery produces accurate degradation results as opposed to any analytical or experimental models while reducing the cost by simulating other parts of the system.

Generally, HIL systems for battery degradation testing are developed using dSPACE, National Instruments and other platforms that are very costly and sophisticated [4]. For example, Authors in [5] used an HIL setup with NHR battery tester and NI DAQ equipment, which can produce a battery equivalent circuit model (ECM) with errors less than 0.01%. However, the setup is only able to test one unit, either a cell, a module, or a pack of battery. To have conclusive results about battery degradation, experiments must be repeated on multiple cells. Which would prolong the degradation studies to inordinately. In such conditions, a low-cost system needs to be adopted where multiple cells can be tested simultaneously.

This chapter describes such a low-cost HIL system based on a Raspberry-Pi, capable of performing battery degradation tests. The residential loads are simulated in an optimization problem, are part of the simulation which produces the load profiles for the battery. Raspberry-Pi based HIL system cycles the LG INR18650 MJ1 cells repeatedly

according to the residential load profiles to degrade the battery. Serial peripheral interface (SPI) is utilized by the Raspberry-Pi to communicate with the configurable power supply and electronic load through ADCs and digital potentiometer.

The rest of the chapter is organized as follows. Section 4.2 provides an overview of the entire HIL system used for residential energy storage degradation. The description of the optimization problem that contains the residential loads and produces the battery load profile is described in section 4.3. Section 4.4 divulges the details of schematics and operations of the MiniLab HIL system. In section 4.5, the preliminary results are discussed and utilized to assess the performance MiniLab's performance as a HIL simulation system, followed by the conclusion.

## **4.2 Overview of the HIL Simulation**

The simulation section of the HIL consists of an optimization problem with typical residential loads and control algorithms for the Raspberry Pi. The following flowchart in Figure 4.1 provides a top-level overview of the entire process.

The HIL simulation starts with selecting the appropriate application, in this case, lithium batteries as residential energy storage. The next step involves deciding the type of load that is part of the residential load. Once the loads are selected and their parameters are well defined, an optimization problem is set up and solved to obtain the load profile or the effect of the loads, grid, renewable energy sources on the battery. This load profile is scaled down and translated to battery current suitable to the desired size, in this case, a single cell. The battery current is then provided to the Raspberry-Pi. The Raspberry-Pi has an algorithm

that checks the state of charge (SOC) of the battery which needs to be tested. The algorithm is designed to start with a fully charged battery. Once the battery is fully charged, it is cycled repeatedly until total Ah throughput reaches a pre-specified value

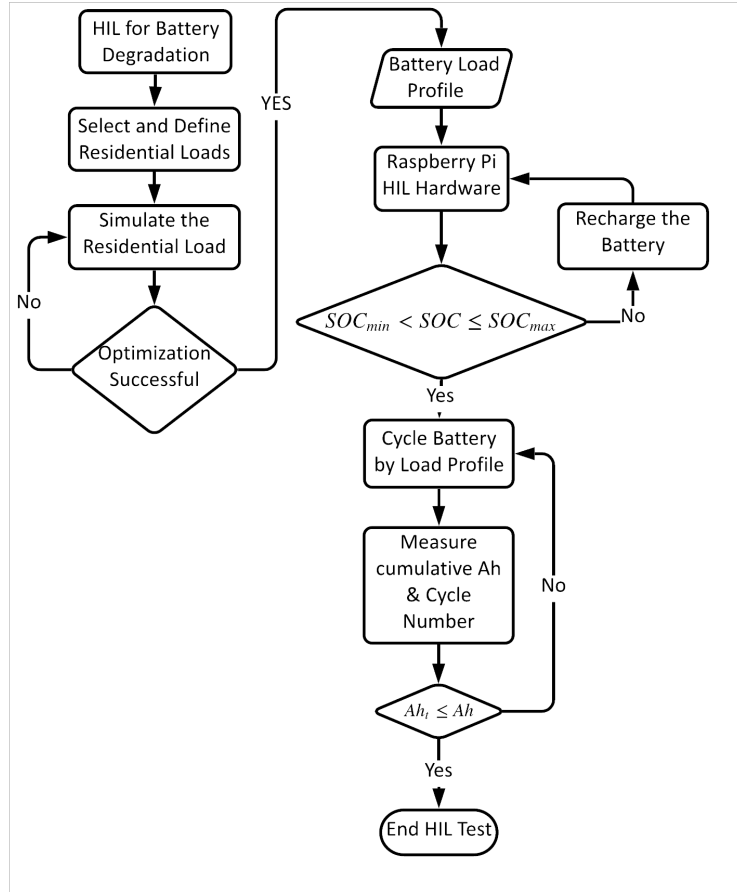


Figure 4.1. Overview of the HIL simulation.

### 4.3 Residential Load Problem Formulation

It is assumed the residential loads are connected to a smart home energy management system (SHEMS), which communicates and controls different household loads in real-time while taking input from the user through human machine interfaces (HMI). Furthermore, it is also assumed that the SHEMS receives day ahead prices [6]. It develops an optimized

load schedule for the household loads utilizing day ahead prices available. These optimizations conserve electricity usage and increase energy utilization efficiency [7]–[9]. In this residential load simulation, a discrete linear load and generation model is used, as the overall system operation is considered in discrete time with a finite horizon,  $T$ , and equal time interval,  $\Delta t$ . Some assumptions were considered such as the smart meter receives day-ahead electricity price while having the capability to log consumption statistics, the weather forecast is available from the data center, and each load can communicate with the meter.

The load models utilized to develop the optimization problem were obtained from [10]. The residential battery was sized according to the specifications of Tesla Powerwall 2 [11]. Several scenarios were developed with residential loads. These scenarios include the capability to perform grid services, EV schedule, the effect of solar irradiation, and weather conditions. The residential energy storage is modeled according to the specifications of Tesla Powerwall 2, with a configuration of 74P6S, and nominal voltage 50V. The load profile is translated accordingly to match a single cell. Sample battery load profile when the residential battery is performing grid services and when it is prohibited can be seen in Figure 4.2 and Figure 4.3, respectively.

In both figures, battery discharge is positive while the negative represents charging. These two scenarios are identical in all aspects except the grid-tie capabilities. For the grid service prohibited scenario, the residence is not allowed to perform any grid services. This is a common case where the residence is prohibited from the utility service provider, due to lack of infrastructure or legal bindings. On the other hand, the full capability of

residential energy storage is explored where the utility considers the residence as prosumer and can utilize the services for a financial incentive. Furthermore, the solar irradiance, EV schedule, and weather conditions are identical in both cases. The solar irradiance for these two cases shown in Figure 4.4 is typical for the USA.

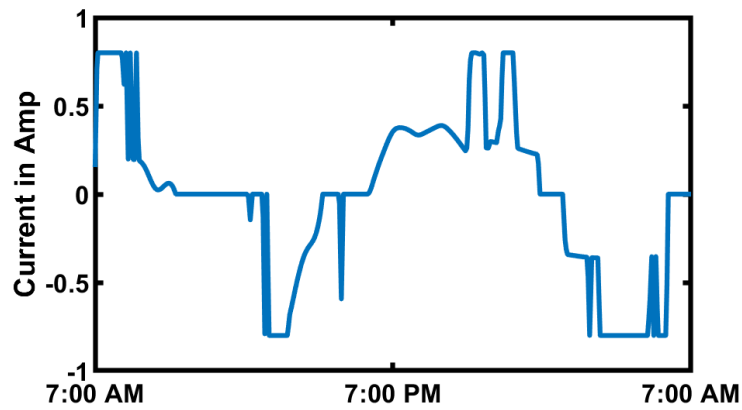


Figure 4.2. Single cell load profile while grid services are prohibited.

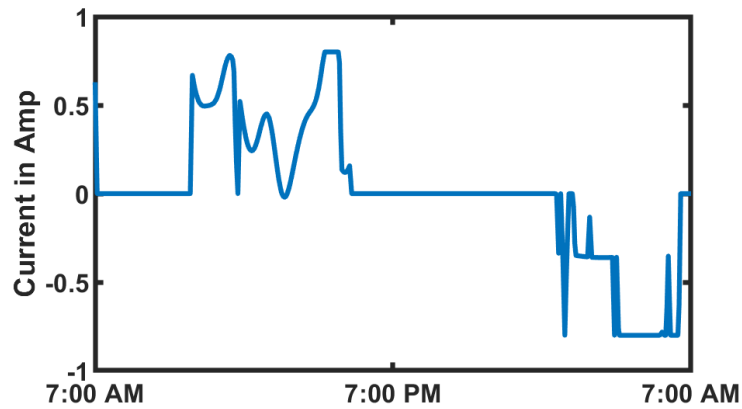


Figure 4.3. Single cell load profile while grid services are performed.

It is evident from these figures that the battery is cycled extensively while grid services are not performed. When the grid services are not performed. The energy generated by the solar PV is stored in the battery. This causes the battery to be cycled repeatedly as opposed to the grid service scenario, in which extra PV energy is sold back



to the grid. Total Ah cycled throughout the entire day for no grid service and grid service case are 7.9Ah and 5.6Ah respectively.

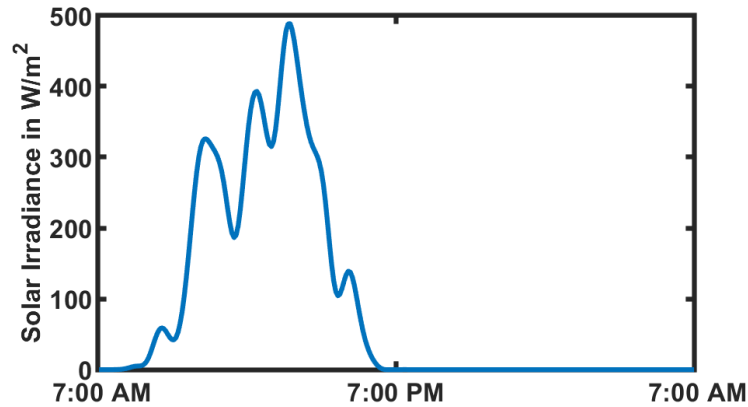


Figure 4.4. Solar irradiance in both case scenarios.

#### 4.4 Schematic and Operation of MINILAB HIL System

The “MiniLab” system is developed in-house as the low-cost alternative HIL simulation system. It is based on a Raspberry Pi 3-model B process with power supply, DC/DC converter, and electronic load. The Raspberry Pi uses a serial peripheral interface (SPI) communication protocol through a digital potentiometer to control the DC/DC converter and electronic load. The battery current feedback from the hall effect sensor is sent through ADC back to the Raspberry Pi. The Python program running on the processors contain two simple PI controller to control the charging and discharging current. A total of 23 MiniLab’s are developed to run multiple scenarios of degradation simultaneously. The details of the construction are elaborated in the following section.

Figure 4.5 shows the entire schematic of the HIL simulation system used to perform degradation tests. Individual MiniLab’s are named “FishX”, to give homage to the originating idea of aging of fishes in a school of fish. The major components of the setup

are shown in the figure. The workstation contains the MATLAB simulation of the residential load and Python program for the MiniLab. The optimized and scaled load profile is provided to the Raspberry Pi along with the hardware control instructions in the form of the Python program through the ethernet switch. The ethernet switch is connected to all the MiniLabs and allows bi-directional communication.

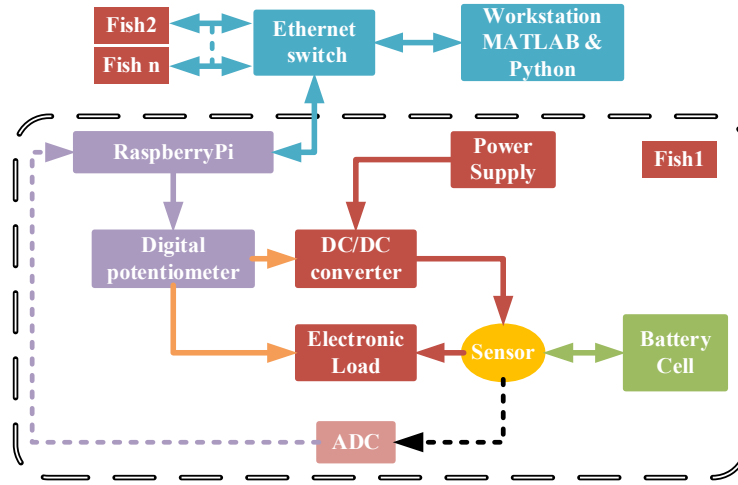


Figure 4.5. Schematic of MiniLab HIL simulation system.

The Raspberry Pi uses SPI to communicate two individual digital potentiometers, one is dedicated to the DC/DC converter and the other to the electronic load. The current measurement from the sensor is feedback to the processor through ADC. The programmed PI controlled in both charging and discharging cases uses battery current profile and feedback to control the respective digital pots. The digital pot converts the digital signals from the processor to resistance values. The resistive output of the digital pot is converted to a corresponding voltage value. This voltage is used to control the DC/DC converter, maintaining a required charging current. Similarly, the electronic load controls the discharging current according to the input of the digital pot.

The power supply is N2Power XL125-12 CS, a fixed supply with high power density [12]. The specification of this power supply is suitable for a single cell MiniLab setup with a small footprint. The power supply provides power to the DC/DC converter. The converter is PTH12040W from Texas Instruments [13]. The output range of the DC/DC converter is 0.8V-5.5V and up to 50A with proper heat sinks, perfectly suitable to test single cells or modules of multiple cells in parallel. The electronic load discharges the battery according to the battery load current. It is also controlled according to a digital pot. The digital pot operates couple of MOSFET's as variable resistance connected to an Intel D34017-001 Aluminum/Copper CPU Heatsink.

Besides the major components, a manual battery disconnect switch is placed in the setup, to prevent any accidental charge or discharge of the battery. Moreover, several diode switches, i.e. diode to prevent current flowing back to the DC/DC converter, MOSFET to enable output of the battery are included in the system for protection and proper operation. Furthermore, fuses rated 10A is used throughout the system to prevent excessive current flowing to or from the battery. Since this system initially is designed to test single cells only, the 10A range of the fuse will allow testing at higher C-rate. The entire setup of the MiniLab HIL simulation system can be seen in Figure 4.6. Total 23 MiniLab's are stacked in 3x4 setup on a custom made structure.



Figure 4.6. MiniLab HIL simulation system.

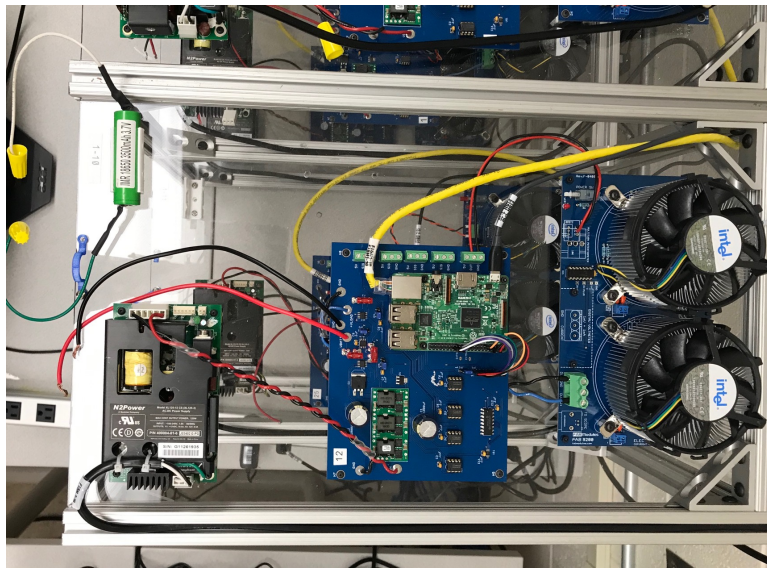


Figure 4.7. Fish1 MiniLab HIL system.

Figure 4.7 shows Fish12 MiniLab. It can be seen from that the entire setup is placed on a plexiglass board with dimensions of 3ft x 1ft. There are four major parts of the MiniLab; the processing unit, power supply, electronic load, and the battery. The power

supply, heat sink fan and the processing unit is powered from a dedicated wall outlet. The yellow wire from the Raspberry Pi 3 connects each MiniLab to the local ethernet switch.

Figure 4.8 shows the details of the processing unit on Fish8. This figure shows the major parts described in Figure 4.5 along with several other components. Specifically, connector ports for the power supply, battery, and bandwidth selector for ICs. The figure also shows the analog input and load connector terminals. The analog input terminals transfer the analog data from external sensors to the ADC. Currently, the current measurement from a hall effect sensor is provided to the processes through these analog channels. There are three extra analog channels made available to be used with any future experiments.

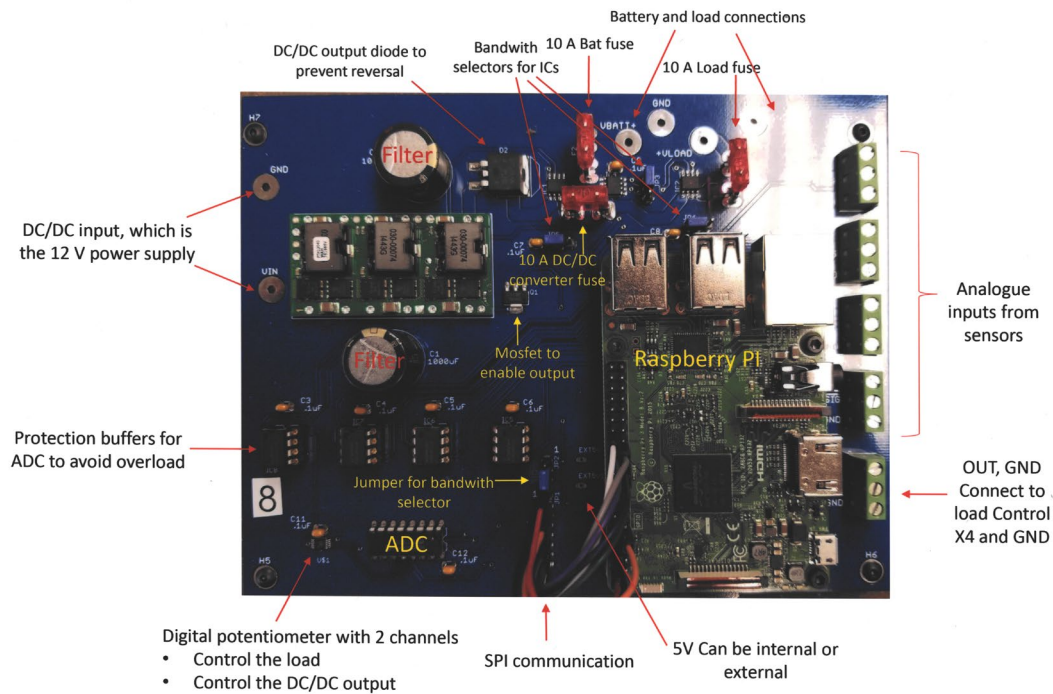


Figure 4.8. MiniLab HIL simulation system.

## 4.5 Initial Results & the Effectivity of MiniLab as HIL System

MiniLab HIL system is capable of distributed testing which means that it is possible to perform multiple degradation testing of multiple scenarios simultaneously. Since the MiniLab is newly developed, before starting to perform 24-hour long testing as suggested by the simulation, the efficacy of this HIL system needs to be tested. Thus, only two cases from prior work [10] were used. These two cases originate from the residence capability of performing grid services, as seen in Figure 4.2 and Figure 4.3.

The result of HIL can be observed in Figure 4.9 when residential energy storage can perform grid services. The experimental result follows the optimized battery load profile. However, the experimental result is marred with noise. The normalized root mean square difference percentage (NRMSDP) in this case is 2.74%. While for the case where no grid services were performed the NRMSDP is 3.27%.

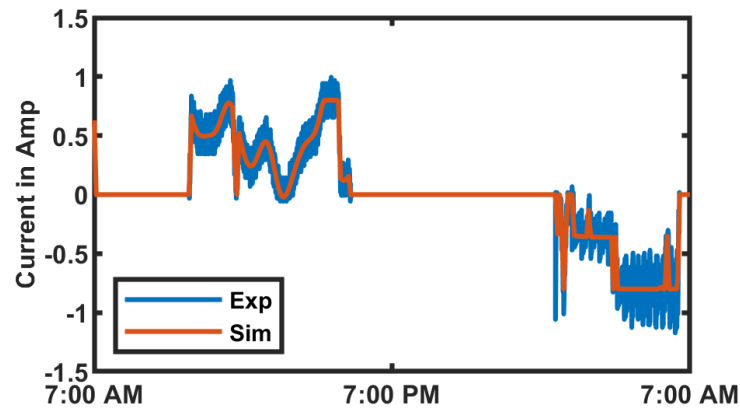


Figure 4.9. Results of HIL while grid services are performed.

The total Ah cycled throughout the entire day while performing grid service according to the experimental data is 5.5Ah. The experimental data has a 2% variation in terms of total Ah throughput in a single day. For the no grid service scenario, the difference

is only 1%. The small NRMSDP and closely matching total Ah cycling indicates that the MiniLab HIL system can successfully perform degradation testing. However, the accuracy of the experimental result can be further improved by applying a tighter PI controller for the DC/DC converter, or including a low pass filter to reduce noise.

The batteries utilized for these aging tests are LG INR18650 MJ1. According to the battery's specification sheet [14], the life cycle of the battery is 400 cycles, where each cycle consists of one complete discharge and charging procedure at rated condition. With the rated capacity of 3.2Ah, the total Ah throughput until the end of life (EoL) is 2720Ah. The battery capacity will fade by 20% at EoL. Thus, to reach EoL, the battery must be continuously cycled for 345 days with no grid service and 486 days with grid service performed scenario. It was observed from a prior detailed hierarchical Bayesian Network (BN) estimation that variation of capacity fade in different scenarios is about 5%. Thus, to validate the prior BN estimation, the capacity fade has through HIL degradation must be more than 5%. Given the uncertainties introduced by manufacturing and experimental processes, to observe any trend the batteries should be cycled until 10% capacity fade is observed. This would require continuous cycling of batteries for about 173 days with no grid service and 243 days with the grid service profile.

## **4.6 Conclusion**

Li-ion batteries are being introduced in various applications due to their inherent qualities. Residential energy storage is one such case. However, to make the Li-ion powered residential energy storage reliable and sustainable, the degradation issue needs to

be addressed. This chapter divulges the details of the low-cost HIL simulation system that is used to perform capacity fade degradation tests on Li-ion batteries used in residential energy storage. This low-cost system is developed with the aim to reduce cost while having the capability to perform aging tests on multiple cells in various degradation scenarios simultaneously. The overview and the schematic of the Raspberry Pi 3 based HIL were discussed in detail. It was shown that the results of the HIL simulation closely matches the battery load profile provided by the residential load profile optimization. The low-cost HIL system was developed to run aging tests and validate prior BN estimation. A discussion on the time required to obtain results comparable to BN estimation was also included. Further experimental work is required to generate more data to analyze battery degradation. These degradation data then can be utilized to validate prior research work.

## References

- [1] J. Khazaei, L. Piyasinghe, V. R. Disfani, Z. Miao, L. Fan, and G. Gurlaskie, "Real-time simulation and hardware-in-the-loop tests of a battery system," in *IEEE Power and Energy Society General Meeting*, 2015, vol. 2015-September.
- [2] C. S. Edrington, M. Steurer, J. Langston, T. El-Mezyani, and K. Schoder, "Role of Power Hardware in the Loop in Modeling and Simulation for Experimentation in Power and Energy Systems," *Proc. IEEE*, vol. 103, no. 12, pp. 2401–2409, Dec. 2015.
- [3] Y. Zhang, R. Xiong, H. He, and W. Shen, "Lithium-Ion Battery Pack State of Charge and State of Energy Estimation Algorithms Using a Hardware-in-The-Loop Validation," *IEEE Trans. Power Electron.*, vol. 32, no. 6, pp. 4421–4431, Jun. 2017.
- [4] A. Taksale, V. Vaidya, P. Shahane, G. Dronamraju, and V. Deulkar, "Low-cost hardware-in-loop for automotive application," in *2015 International Conference on Industrial Instrumentation and Control, ICIC 2015*, 2015, pp. 1109–1114.
- [5] K. Khan, M. Jafari, and L. Gauchia, "Comparison of Li-ion battery equivalent circuit modeling using impedance analyzer and Bayesian networks," *IET Electr.*



*Syst. Transp.*, vol. 8, no. 3, 2018.

- [6] B. Zhou *et al.*, “Smart home energy management systems: Concept, configurations, and scheduling strategies,” *Renew. Sustain. Energy Rev.*, vol. 61, pp. 30–40, Aug. 2016.
- [7] P. Zhang, F. Li, and N. Bhatt, “Next-Generation Monitoring, Analysis, and Control for the Future Smart Control Center,” *IEEE Trans. Smart Grid*, vol. 1, no. 2, pp. 186–192, Sep. 2010.
- [8] A. Vojdani, “Smart Integration,” *IEEE Power Energy Mag.*, vol. 6, no. 6, pp. 71–79, 2008.
- [9] A. Brooks, E. Lu, D. Reicher, C. Spirakis, and B. Wehl, “Demand Dispatch,” *IEEE Power Energy Mag.*, vol. 8, no. 3, pp. 20–29, May 2010.
- [10] K. Khan, T. Hossen, A. Savaci, L. Gauchia, and S. Paudyal, “Design of A Simplified Hierarchical Bayesian Network for Residential Energy Storage Degradation,” in *2019 IEEE Power & Energy Society General Meeting (PESGM)*, 2019.
- [11] Tesla, “Tesla Powerwall 2 Specification Sheet,” 2019.
- [12] N2Power, “N2Power XL125-12 CS AC-DC Power Supply,” 2019. [Online]. Available: [www.n2power.com](http://www.n2power.com). [Accessed: 12-Nov-2019].
- [13] T. Instruments, “PTH12040W 50-A, 8 to 14-V Input, Wide-Output Adjust Power Module | TI.com,” 2019. [Online]. Available: <http://www.ti.com/product/PTH12040W>. [Accessed: 12-Nov-2019].
- [14] K. S. Oh and D. M. Kim, “Product Specification of Rechargeable Lithium-Ion Battery Model : INR18650 MJ1 3500mAh,” 2014.

## Conclusions

This dissertation is an accumulation of my research work that was conducted in four different stages. The first stage was focused on mostly literature review, to obtain a firm understanding of battery characteristics, degradation process and the experimental procedures involved to assess those procedures. The majority of the second stage consisted of battery characterization experimentations and associated data analysis utilizing various methods. A detailed hierarchical Bayesian Network was proposed to evaluate the degradation of lithium-ion residential energy storage systems in the third stage. The fourth stage discusses a low-cost hardware-in-the-loop simulation process that is being used to validate the results of the degradation estimation of stage three. The following parts summarize the highlighted findings of different stages in my research.

- **State 1:** A detailed literature review about Li-ion battery characterization and degradation processes was performed in this stage. Deterministic empirical methods obtained through rigorous experimental procedures are more than capable to predict the instantaneous performance of the battery. However, it was realized that a deterministic method to address the battery aging phenomenon is inadequate. Thus, a probabilistic approach utilizing well-defined deterministic aging mechanics can provide an improved understanding of the degradation process. The literature review aided in choosing the modified Arrhenius equation, the most appropriate battery degradation method for our scale of operations.

- Stage 2:** Multiple types of extensive characterization experimentations in both time and frequency domain were performed on Li-ion batteries in this stage. The experimentations revealed that frequency domain electrochemical impedance spectroscopy (EIS) can determine the battery internal impedance than any time-domain tests. However, improved regression methods, i.e. Bayesian Network based regression can improve the EIS impedance characterization. This stage also served as a precursor for stage 4, as it provided the technical knowledge required to develop and perform real-time hardware-in-the-loop (HIL) experiments, which is essential in battery degradation tests. Furthermore, the foundation of Energy Storage Systems and Sustainability (E3S) Lab at Michigan Technological University was established through this process.
- Stage 3:** A detailed hierarchical Bayesian Network (BN) to evaluate degradation for li-ion residential energy storage was proposed in this stage. The BN was developed anticipating the possible uncertainties of process and measurements. The modified Arrhenius equation presented the means to relate battery degradation to external causal factors such as grid connectivity, solar irradiance and weather conditions. The estimation process was solved with the Markov Chain Monte Carlo technique and the Metropolis-Hastings algorithm. The estimation revealed that the battery degradation was higher when the residential energy storage is prohibited to perform grid services. It was also revealed that lower ambient temperature increases the capacity fade,

although the residential battery is generally placed inside the household generally. Finally, it was also realized that higher solar irradiance causes higher degradation throughout the lifetime of the battery.

- **Stage 4:** This stage was dedicated to developing a hardware-in-the-loop (HIL), multi-unit, low-cost, reliable, and sustainable li-ion battery degradation testing facility for the E3S lab. The Raspberry Pi based MiniLab HIL system was developed in-house, initially to evaluate the capacity fade estimations proposed by the BN in stage 3. Several MiniLabs are being used simultaneously to perform aging tests for various scenarios on multiple cells, promising improved data sets to validate the BN proposals. The preliminary results reveal that MiniLab is capable of performing HIL with the utmost accuracy for prolonged periods of testing.

## Contributions

Following a detailed review of various Li-ion aging characterization methods used in contemporary research, I realized that the probabilistic approach with the aid of a generally utilized deterministic model would be able to evaluate the aging process and relate to external causal factors. To improve my understanding and have a well-rounded knowledge of battery characteristics, aging, and testing procedure involved, I started my research with the experimental side. I developed the procedure and perform time and frequency domain tests to characterize Li-ion batteries. Different regression methods were used to analyze the experimentally obtained data to generate 8RC battery model, capable of predicting instantaneous battery performance with less than 1% error. The results were improved further by Bayesian Network regression methods. As a consequence of these experimental studies, the foundation of Energy Storage Systems and Sustainability (E3S) Lab at Michigan Technological University was established. Later on, I improved on the knowledge of Bayesian Network based regression, to develop a detailed hierarchical Bayesian Network (BN) to evaluate the degradation of Li-ion residential energy storage system. The BN is generated considering the most perceivable uncertainties of process and measurements. The BN utilizes a well-established modified Arrhenius equation to relate battery degradation to external causal factors. I used Markov Chain Monte Carlo and Metropolis-Hastings ratio to solve the BN and generate posterior probability distributions about capacity fade and several other interesting observations. Furthermore, I worked in establishing the low-cost hardware-in-the-loop (HIL) battery aging testing facility, MiniLab, to validate BN estimations. The preliminary results show that MiniLab is capable

of performing degradation testing for an extended period with the utmost accuracy. Throughout working with the BN, it was realized that though I have limited this dissertation to a specific application and technology of Li-ion, this probabilistic approach can be modified and adopted by any application or technology, conditional on available training data. Overall, this generates a new avenue for analyzing battery degradation analysis.

## Future Work

This dissertation proposes a probabilistic approach to determine Li-ion battery degradation through a detailed hierarchical Bayesian Network (BN) for residential energy storage systems. The BN explores the effects of grid services, solar irradiation, EV schedule and weather conditions on battery aging. However, there are some shortcomings that could be worked upon to improve this research further, which are listed as follows.

- The aging tests with the MiniLab should continue in order to ascertain the estimations generated by BN. It would be interesting to observe the capacity fade from MiniLab testing and their location on the posterior probability distributions of capacity fade given by BN trained by experimental results.
- The degradation experiment should be performed on the aged batteries as well. The results of the capacity fade from aged batteries can be used to train another BN to estimate degradation for second life use. These tests and estimations through multiple life and relationship with the causality factors will provide a better understanding of how to utilize batteries through multiple life cycles.
- The proposed model does not include the effect of calendar aging. The Li-ion battery also degrades while it is not being cycled, especially when it is left at fully charged conditions, albeit at a very slow pace as opposed to the cycle aging. The calendar aging can be included with another dedicated node in the existing BN. The calendar aging node should have another hierarchical model

that may involve utilizing some node from calendar degradation, i.e. state of charge (SOC). Afterward, the aging from both nodes can be aggregated into another node which provides the probability distribution of total capacity fade.

- The research focuses on capacity fade only while disregarding power fade. In the aging process capacity fade and power fade occurs simultaneous, thus battery power fade needs to be included while analyzing battery degradation. A node can be included in the existing BN for relating the determined capacity fade with power fade. The BN can be trained by experimental results to relate power and capacity fade with dedicated parameters.
- The BN should include the effect of cost for the individual operation of the battery. This requires multiple nodes to be inserted in the BN and a significant amount of actual billing data for individual loads. This modification can aid to do a cost-volume-profit or break-even analysis. The prosumer or the utility can use such analysis to judge what services to be performed by the residential energy storage.
- Rather than using a single node, the grid services can be divided into common services performed by the residential energy storage. Combined with the involvement of cost per load or service, the utilities can use this method to choose what services to perform in order to make a profit.



# A Copyright Documentations

## Chapter 1:

10/7/2019

Rightslink® by Copyright Clearance Center



RightsLink®

Home

Create Account

Help



**Title:** Deterministic models of Li-ion battery aging: It is a matter of scale  
**Author:** Mehdi Jafari, Khalid Khan, Lucia Gauchia  
**Publication:** Journal of Energy Storage  
**Publisher:** Elsevier  
**Date:** December 2018

© 2018 Elsevier Ltd. All rights reserved.

LOGIN

If you're a [copyright.com user](#), you can login to RightsLink using your copyright.com credentials.

Already a [RightsLink user](#) or want to [learn more?](#)

Please note that, as the author of this Elsevier article, you retain the right to include it in a thesis or dissertation, provided it is not published commercially. Permission is not required, but please ensure that you reference the journal as the original source. For more information on this and on your other retained rights, please visit: <https://www.elsevier.com/about/our-business/policies/copyright#Author-rights>

BACK

CLOSE WINDOW

Copyright © 2019 [Copyright Clearance Center, Inc.](#) All Rights Reserved. [Privacy statement](#). [Terms and Conditions](#).  
Comments? We would like to hear from you. E-mail us at [customercare@copyright.com](mailto:customercare@copyright.com)

## Chapter 2:

10/16/2019

Michigan Technological University Mail - Permission needed to reproduce for dissertation



Michigan Tech

Khalid Khan <kkhan@mtu.edu>

---

### Permission needed to reproduce for dissertation

---

4. journals <journals@theiet.org>  
To: "kkhan@mtu.edu" <kkhan@mtu.edu>

Wed, Oct 16, 2019 at 9:34 PM

Dear Dr Khalid

Thank you for your email. You're to re-use the material as per your request without any charge or embargo period, please ensure that you cite and reference the original paper within your thesis.

Please don't hesitate to contact me if you have any further queries.

Kind regards,

**Katherine Ivory**

Senior Editorial and Production Assistant & Permissions Officer (Research Journals and Letters)



The Institution of  
Engineering and Technology

Visit our website [www.theiet.org](http://www.theiet.org)

Follow us on [Twitter @IET\\_Journals](#) and [LinkedIn](#)

Michael Faraday House, Six Hills Way, Stevenage, SG1 2AY, United Kingdom

**From:** Khalid Khan <kkhan@mtu.edu>  
**Sent:** Wednesday, October 9, 2019 7:10 AM  
**To:** 4. iet\_est <iet\_est@theiet.org>  
**Subject:** Permission needed to reproduce for dissertation

Hello,

I'm Khalid. I'm the first author of 'Comparison of Li-ion battery equivalent circuit modelling using impedance analyzer and Bayesian networks', published on IET Electrical Systems in Transportation, 2018, 8, (3), p. 197-204, DOI: 10.1049/iet-

<https://mail.google.com/mail/u/0?ik=c2f5d015fb&view=pt&search=all&permmsgid=msg-f%3A1647564641152215397&simpl=msg-f%3A164756464115...> 1/2

10/16/2019

Michigan Technological University Mail - Permission needed to reproduce for dissertation

est.2017.0087.

I intend to use some of the materials from this published journal for my PhD Dissertation. I believe I need your official permission to reproduce any part of this publication. Can you please tell me what is the procedure for this?

With Regards,  
Khalid Yousuf Khan  
Ph.D. Candidate  
Department of Electrical and Computer Engineering  
Michigan Technological University  
Houghton, MI, 49931

[Redacted]

---

The Institution of Engineering and Technology ("IET") is registered as a Charity in England and Wales (No. 211014) and Scotland (No. SC038698). The information transmitted is intended only for the person or entity to which it is addressed and may contain confidential and/or privileged material. Any review, retransmission, dissemination or other use of, or taking of any action in reliance upon, this information by persons or entities other than the intended recipient is prohibited. If you received this email in error, please contact the sender and delete the material from any computer. The views expressed in this message are personal and not necessarily those of the IET unless explicitly stated. The IET cannot guarantee that this email and any attachments are virus free.

<https://mail.google.com/mail/u/0?ik=c2f5d015fb&view=pt&search=all&permmsgid=msg-f%3A1647564641152215397&simpl=msg-f%3A164756464115...> 2/2

## Permission for Additional Publication:

11/13/2019

Rightslink® by Copyright Clearance Center



RightsLink®



Home



Help



Live Chat



Khalid Khan ▾



### Modeling, parameterization, and benchmarking of a lithium ion electric bicycle battery

Conference Proceedings: 2016 IEEE Energy Conversion Congress and Exposition (ECCE)

Author: Weizhong Wang

Publisher: IEEE

Date: Sept. 2016

Copyright © 2016, IEEE

#### Thesis / Dissertation Reuse

The IEEE does not require individuals working on a thesis to obtain a formal reuse license, however, you may print out this statement to be used as a permission grant:

*Requirements to be followed when using any portion (e.g., figure, graph, table, or textual material) of an IEEE copyrighted paper in a thesis:*

- 1) In the case of textual material (e.g., using short quotes or referring to the work within these papers) users must give full credit to the original source (author, paper, publication) followed by the IEEE copyright line © 2011 IEEE.
- 2) In the case of illustrations or tabular material, we require that the copyright line © [Year of original publication] IEEE appear prominently with each reprinted figure and/or table.
- 3) If a substantial portion of the original paper is to be used, and if you are not the senior author, also obtain the senior author's approval.

*Requirements to be followed when using an entire IEEE copyrighted paper in a thesis:*

- 1) The following IEEE copyright/ credit notice should be placed prominently in the references: © [year of original publication] IEEE. Reprinted, with permission, from [author names, paper title, IEEE publication title, and month/year of publication]
- 2) Only the accepted version of an IEEE copyrighted paper can be used when posting the paper or your thesis online.
- 3) In placing the thesis on the author's university website, please display the following message in a prominent place on the website: In reference to IEEE copyrighted material which is used with permission in this thesis, the IEEE does not endorse any of [university/educational entity's name goes here]'s products or services. Internal or personal use of this material is permitted. If interested in reprinting/republishing IEEE copyrighted material for advertising or promotional purposes or for creating new collective works for resale or redistribution, please go to [http://www.ieee.org/publications\\_standards/publications/rights/rights\\_link.html](http://www.ieee.org/publications_standards/publications/rights/rights_link.html) to learn how to obtain a License from RightsLink.

If applicable, University Microfilms and/or ProQuest Library, or the Archives of Canada may supply single copies of the dissertation.

BACK

CLOSE

© 2019 Copyright - All Rights Reserved | Copyright Clearance Center, Inc. | Privacy statement | Terms and Conditions  
Comments? We would like to hear from you. E-mail us at [customer@copyright.com](mailto:customer@copyright.com)

<https://s100.copyright.com/AppDispatchServlet#formTop>

1/1